

Stellingen behorende bij het proefschrift Focusing Grating Couplers for Integrated Optics

- 1 For a perfect focusing grating coupler, the optical path calculated from the light source through a fixed point at a groove to the focus differs from that calculated from the same light source through the corresponding point on an adjacent groove to the focus by one wavelength.

Nils Abramson, "Principle of least wave change," *Journal of Opt. Soc. Am. A*, Vol.6, No.5, pp.627-629, (1989).

- 2 Misalignment of optical collimating system OSI will contribute coma to the reconstructed beam. After minimizing the focal spot size in the observation plane containing the diffraction focus by adjusting the angle of incidence between the collimated guided wave and the FGC, the coma tail points away from the focus either along the propagation direction of the incident wave or opposite to that, depending upon the tilt angle of OSI. From this particular orientation, we can determine if system OSI is orientated correctly. For a Strehl intensity of 0.8, the tolerances of the tilt angle are calculated as $\pm 0.1^\circ$ ($N.A.=0.6$) and $\pm 0.2^\circ$ ($N.A.=0.3$) for two FGC's with the waveguide parameters given in Table 3.1 in this thesis, Chapter 3.

- 3 The residual wavefront error caused by system OSI as calculated at the recording wavelength λ_h (see Fig.4.7 of this thesis, Chapter 4) will contribute an aberration to the reconstructed beam at the wavelength of λ_0 ($\lambda_0 > \lambda_h$). The aberration is found to equal the residual wavefront error multiplied by the wavelength ratio $\frac{\lambda_0}{\lambda_h}$ (not scaled down by the same factor as mistakenly stated in Ref.[20]).

- 4 Consider an oblate spheroidal coordinate system formed by rotating a system of mutually orthogonal ellipses and hyperbolas about the minor axis of the ellipse. These coordinates can be useful to describe the propagation of a Gaussian beam because of the simplicity of modeling a contour of constant amplitude in the beam as one sheet of a hyperboloid, being a coordinate surface in the mentioned system. A family of ellipses confocal with the amplitude hyperbola form the Gaussian beam wavefronts exactly.

B. Tehan Landesman and H.H. Barrett, "Gaussian amplitude functions that are exact solutions to the scalar Helmholtz equation," *Journal of Opt. Soc. Am. A*, Vol.5, No.10, pp.1610-1619, (1988). B. Tehan Landesman, "Geometrical representation of the fundamental mode of a Gaussian beam in oblate spheroidal coordinates," *Journal of Opt. Soc. Am. A*, Vol.6, No.1, pp.5-17, (1989).

- 5 A diffractive optical element (DOE) has a very large chromatic aberration as compared to a conventional lens. It has been difficult to use DOE's in high-precision optical systems that use a light source with a variable wavelength (*e.g.* a diode laser). An achromatic optical system could be made from two DOE's similar to a conventional doublet which means that FGC's could work with waveguide grating lenses to reduce the chromatic aberration.

Masayuki Kato, Satoshi Maeda, Fumio Yamagishi, Hiroyuki Ikeda and Takefumi Inageki, "Wavelength independent grating lens system," *Applied Optics*, Vol.28, NO.4, pp.683-686, (1989).

- 6 An array of small periodic pillars (whose cross-section may be considered as a two-dimensional doubly periodic grating) produced on an optical surface can be used to reduce reflection from that surface. This is especially important for infrared optical components made of high refractive index materials, which may not be able to tolerate conventional coatings. The layer with the pillar array structure is equivalent to a quarter-wave antireflection coating, if the pillar height equals a quarter wavelength and its periodicity is smaller than a chosen wavelength.

M.E. Motamedi, W.H. Southwell, and W.J. Gunning, "Antireflection surfaces in Silicon using binary optics technology," *Applied Optics*, Vol.31, No.22, pp.4371-4375, (1992).

- 7 A man should work until he succeeds. If he stops halfway and wastes all his previous effort, it is usually because his will is not firm, not because he lacks the strength.

- 8 A scientist's willingness to retract his mistakes honestly and openly is more important in establishing his scientific stature than a long list of discoveries.

Richard Muller, "Nemesis, the story of a scientific revolution," Guild Publishing London, (1989).

- 9 A teacher can only point at the basic principles of an art, to perform wonders in that art the pupil himself must seek to understand the principles with his heart.

- 10 A way of thinking based on stimulation of creativity and on generation of ideas from imagination, is a reliable way to revive developments that have got stuck.

566427

3174283

TR diss 2121

~~217~~

**TR diss
2121**

Focusing Grating Couplers for Integrated Optics

Focusing Grating Couplers for Integrated Optics

Proefschrift

ter verkrijging van de graad van
doctor aan de Technische Universiteit Delft,
op gezag van de Rector Magnificus,
prof. drs. P.A. Schenck,
in het openbaar te verdedigen
ten overstaan van een commissie aangewezen
door het College van Dekanen,
op maandag 26 oktober 1992 te 16.00 uur

door

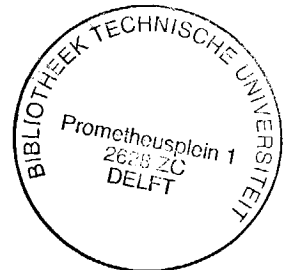
Chieh-wen Wang

geboren te Taiwan, the Republic of China

Master of Science in Electro-Optical Engineering



Delft University press / 1992



Dit proefschrift is goedgekeurd door de promotor

Prof. dr. ir. H.J. Frankena

The work described in this thesis was sponsored by 'Nederlandse Organisatie voor Toegepast Natuurwetenschappelijk Onderzoek' (TNO) and by the 'Industrial Technology Research Institute' (ITRI) in Taiwan, the Republic of China.

ISBN 90-6275-818-5 / CIP

Copyright ©1992 by Chieh-wen Wang and the Research Group of Optics, Department of Applied Physics, Delft University of Technology, The Netherlands.

All rights reserved.

No part of the material protected by this copyright notice may be reproduced or utilized in any form or by any means, electric or mechanical, including photocopying, recording or by any information storage and retrieval system, without permission from the publisher: Delft University Press, Stevinweg 1, 2628 CN Delft, The Netherlands.

Telephone +31 15 783254 Fax +31 15 781661

Printed in The Netherlands

To my Mother and Father

Contents

1	INTRODUCTION	1
1.1	The focusing grating coupler (FGC) and its historical background	1
1.2	Scope and organization of this dissertation	3
2	THEORETICAL CONSIDERATIONS	5
2.1	Introduction	5
2.2	The grating pattern equation for the FGC	6
2.3	Off-axis image formation and wavefront aberration	10
2.4	The field distribution of the focused wave in the exit plane . . .	14
2.5	The field distribution around the focus	18
3	COMPUTATION RESULTS	19
3.1	Computational setup	19
3.2	Comparison with earlier theories	21
3.3	Field distribution in the exit plane	28
3.4	Field distribution around the focus	28
3.5	The influence of the corrugation depth	32
3.6	The diffraction image in the presence of aberrations	33
3.7	Tolerances for the FGC structure	35
4	HOLOGRAPHICAL SETUP FOR RECORDING FGC'S	37
4.1	Basic setup	37

4.2	The design method	39
4.3	The design of the optical systems	49
4.4	Calculation of the intensity distribution in the recording plane	61
5	EXPERIMENTAL RESULTS	71
5.1	The fabrication process	71
5.2	The measurement setup	76
5.3	Focusing characteristics	77
6	DISCUSSION AND CONCLUSIONS	87
A	FORMULAS FOR CALCULATING THE AMPLITUDE FACTORS OF THE FLOQUET WAVES AND THE QUANTITY $\delta\beta$	91
	REFERENCES	98
	ACKNOWLEDGEMENTS	103
	SUMMARY	105
	SAMENVATTING	109
	CURRICULUM VITAE	113

Chapter 1

INTRODUCTION

1.1 The focusing grating coupler (FGC) and its historical background

Optical components which are constructed as parts of integrated circuits will improve the reproducibility, reduction of size, weight and cost, and can enhance the application flexibility. Following the development of micro-fabrication technology, combination of components into an optical integrated circuit has become possible. Gratings with periodicities comparable to one wavelength or even smaller, whose operation is based upon diffraction, are widely used as passive components in applications related to optical telecommunication, optical computers, optical data storage and optical sensors [1] for realizing deflectors, wavelength filters, (de)multiplexers and mode converters. All those grating functions can be classified, according to their dependence on optical wave coupling, as either guided-wave to guided-wave coupling or guided-wave to radiation-wave coupling. In this dissertation, only the latter is considered. The first grating coupler with straight and periodic grating lines was produced by M.L. Dakss in 1970 [2]. Grating couplers similar to prism couplers can either couple a collimated guided wave into a collimated radiation wave outside the waveguide

(output coupler) or vice versa (input coupler). Chirped grating couplers with straight grating lines can be used to couple a beam out of a waveguide forming a focused line parallel to the grating lines [3], acting simultaneously as a wavefront converter and as an outcoupler. The period of such a chirped grating decreases monotonically along the propagation direction of the guided wave. In Ref. [3], chirped gratings were produced by recording the interference pattern of a plane wave and a convergent cylindrical wave, with a focal line perpendicular to the plane of incidence of both recording waves, at an Ar-ion laser wavelength of $457.9nm$. Reconstruction occurred at various wavelengths of the same laser. The chirp rate of the grating was controlled by adjusting the angle between the two recording waves. However, a sharp focused line cannot be obtained if the wavelengths during recording and reconstruction are different. To form a sharp focused line, aberrations caused by the wavelength shift must be compensated by modifying the wavefronts of the recording beams. In the case that the focal line of the cylindrical recording waves is rotated over 90° with respect to the previous case, the grating lines are equally spaced but curved. A cylindrical wave, whose focal line is located in the plane passing through the symmetry axis of the grating line and normal to the planar waveguide, was coupled out of the waveguide using a grating coupler of this kind [4].

Focusing grating couplers (FGC's) are designed to focus a guided wave in an integrated optical circuit onto a point above the waveguide. Often, an FGC has a chirped as well as curved grating pattern to match the phase condition between the guided wave and the focused spherical wave at the output [6]. M. Miler and M. Skalsky produced the first published FGC using two cylindrical waves with mutually perpendicular focal lines, lying in different planes [5]. D. Heitman and C. Ortiz [8] produced FGC's by recording the interference pattern of a plane wave and a spherical wave at the wavelength $457.9nm$. The photoresist grating itself (without transferring the grating pattern into the dielectric layer below the photoresist with the aid of etching techniques) directly served as a

output coupler for use at $632.8nm$. Their results show that a focal spot width of $2.2\mu m$ for an FGC with a focal length $150\mu m$ and a grating diameter $100\mu m$ ($N.A.=0.31$) can be achieved. Another grating coupler [8] with a focal length of $1mm$ and a grating area of $0.5 \times 0.6mm^2$ ($N.A.\approx 0.24$) had an aberrated spot width of $25\mu m$ and showed predominant coma and astigmatism. D. Heitman and C. Ortiz suggested that FGC's could be used for video disk pick-up heads and for optical data storage systems.

An integrated-optical disk pickup device as described in [6] is constructed by integrating an FGC, grating lenses, and photodiodes in a waveguide on an Si substrate. A guided wave diverging from a butt-coupled laser diode is diffracted by the FGC onto a spot on an optical disc and the wave reflected by the disc is coupled into the waveguide by the same FGC. Twin Bragg type grating lenses which serve as a 50% beam splitter diffract and focus part of the returning light onto two detectors at either side of the laser. The focusing error signal is obtained from the photocurrents of the detectors, using push-pull methods. Electron beam writing has been employed to produce the FGC in that demonstration device. This FGC had a focal length of $2.0mm$, aperture of $1.0 \times 1.0mm^2$ and a 3-dB spot width of $3.5\mu m$ at the wavelength of $790nm$ ($6\mu m$ at $\frac{1}{e^2}$ of the peak intensity).

1.2 Scope and organization of this dissertation

We aim at a design of an FGC in which a guided diverging wave is outcoupled as a spherical wave converging to a point above the waveguide. The incident guided wave (collimated in the experiments) is generated by prism-incoupling into the waveguide. The field distribution at the FGC and at the focal plane are investigated theoretically. FGC's are produced by holographic recording

and are etched into the waveguide surface by wet chemical etching. The design of the optical systems, necessary to perform the holographical recording of the required grating, has been deduced from theoretical considerations. The field distribution around the focus of the diffracted beam is studied by recording the intensity.

Chapter 2 presents a model including the vectorial treatment of the electromagnetic field, in order to calculate the field distributions at the FGC and around the focal point for estimating the image quality.

Chapter 3 gives a comparison of the results of our model and those from earlier theories. The field distributions at the FGC and around the focus are calculated for several typical cases. The Strehl intensity at the diffraction focus is used to calculate fabrication tolerances and tolerances of the grating alignment.

Chapter 4 describes the method to design a holographic setup for recording FGC's. Our holographic setup was designed to compensate for the aberration caused by a wavelength shift between the recording and reconstruction processes. The intensity distribution in the recording plane has been calculated to evaluate the performance of our holographic setup. FGC's are to be recorded at the wavelength of $363.8nm$ for coupling a focused beam out of the waveguide using an incident collimated wave with a wavelength of $632.8nm$.

Chapter 5 presents the experimental work. Multilayer waveguides produced on two-inch silicon substrate are used to make FGC's on the waveguides. FGC's are etched into the waveguide surface by wet etching. From experimental results, a focal spot size of $2.9\mu m$ and a grating diameter of $1.3mm$ has been obtained.

Chapter 6 summarizes the main results and presents some suggestions for future investigation.

Chapter 2

THEORETICAL CONSIDERATIONS

2.1 Introduction

A main problem in analyzing FGC's is to determine the focal spot quality. Methods and criteria from geometrical optics are usually employed for this, including an estimate of the wave aberration [7] or computation of the transverse ray aberration [7, 8]. These methods, however, do not allow to calculate the light intensity distribution around the focus. Such a calculation would be useful to obtain a better estimate of the image quality. In Ref. [6], an FGC with low numerical aperture (N.A.=0.24) was modeled assuming a uniform attenuation coefficient across the grating and neglecting the coupling between TE and TM waves. For an FGC with a high numerical aperture, the coupling between TE and TM waves becomes significant and has to be taken into consideration. Seligson [9] devised a method using a vectorial theory to calculate the diffraction field components at the exit plane of an FGC, assuming a collimated incident TE guided wave. In that paper Fourier transform was subsequently employed to compute the field at the focal plane of the grating. The actual grating pattern

was treated as a single entity and the coupling between TE and TM waves was taken into account. However, the attenuation of the guided wave was neglected such that the corrugation depth of the grating remained undetermined. Nevertheless, that method provides a simple way to estimate field distributions at the FGC and at the focal plane.

We'll introduce a different model in which the design of FGC's is similar to Seligson's, but using a more detailed analysis. Specifically, the actual complex propagation constant of the incident guided wave is taken into consideration, leading to the optimization of the corrugation depth. The complex propagation constant of the incident guided wave will be calculated by dividing the FGC into subgratings. In addition, the coupling between TE and TM waves is taken into account. If the dimensions of each subgrating are small (about $30 \times 30 \mu\text{m}^2$, for an FGC with N.A.=0.6 and a focal length of 1mm), the local curvature may be replaced by an average curvature and the chirp rate (usually $< 0.04\%$) can be ignored. In the cases we consider, the average radius of the curvature is supposed to be at least forty times larger than the dimensions of the subgrating such that locally the grating can be replaced by a periodic and straight grating. Then, the FGC may be regarded as an array of subgratings with different periods and orientations. A previously published method of calculating the field distribution at the FGC can be applied directly [10]. Subsequently, the modified Huygens-Fresnel principle [17] will be employed to calculate the field distribution around the focus. As will be seen, our model has the advantage that it can tackle cases including aberrations caused by fabrication errors of the FGC, by a displacement of the light source and by a wavelength shift of the light.

2.2 The grating pattern equation for the FGC

The planar dielectric waveguide, at which the FGC occurs, consists of a guiding film with refractive index n_f sandwiched between media with refractive indices

n_c (cover) on top of it and n_s (substrate) below. An FGC is formed by corrugating part of the cover/film interface as shown in Fig. 2.1. The corrugation

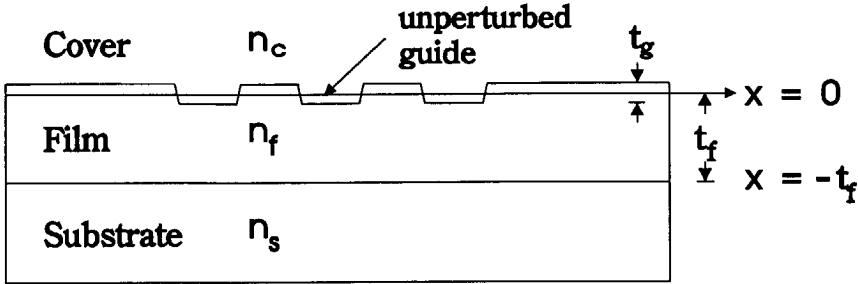


Figure 2.1: Geometry of the planar dielectric waveguide with FGC-grooves, having an arbitrary profile.

depth t_g is assumed to be small as compared to the wavelength of the incident wave and to the average film thickness t_f . Outside the grating area, the film thickness equals $t_f + \frac{t_g}{2}$. The FGC covers a rectangular area in the yz -plane, the origin O of our Cartesian coordinate system lies in the center of the grating. We'll use the diffracted field in the plane $x = 0$ (located at half-height of the corrugation) as the starting value of our calculations around the focal spot; for that reason the plane $x = 0$ will be indicated as the *exit plane* of the grating. The rectangular outline of the grating has sides parallel to the y - and z -axes; the linear dimensions of the FGC in those directions are L_y and L_z (see Fig.2.2). The grating lines are symmetrical around the plane $y = 0$. Let \vec{i} , \vec{j} and \vec{k} be the unit vectors in the directions of the coordinate axes. The unperturbed planar guide with its cover/film boundary at the plane $x = 0$ has the refractive index profile

$$n(x) = \begin{cases} n_c & (x \geq 0), \\ n_f & (-t_f \leq x \leq 0), \\ n_s & (x \leq -t_f). \end{cases} \quad (2.1)$$

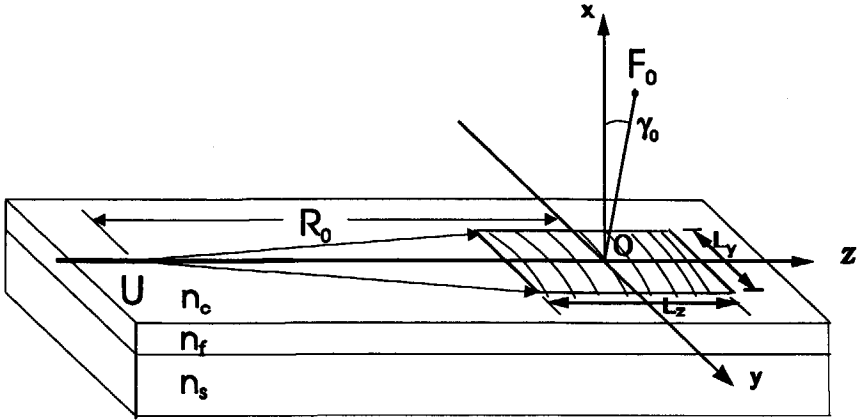


Figure 2.2: Configuration of the FGC.

We suppose that a line source along the x -direction, passing through the point $\mathbf{U}(0, 0, -R_U)$, emanates a diverging guided TE wave towards the grating. The distance R_U is assumed to be much larger than the dimensions of the FGC. The electric field vector of the incident wave in the unperturbed guide is approximately characterized by [11]

$$\vec{E}(x, y, z) = \text{const.} \frac{1}{\sqrt{R_{UQ}}} e^{i\Phi_{in}} E(x) \left(\frac{\vec{\beta}_0}{\beta_0} \times \vec{i} \right), \quad (2.2)$$

and

$$\frac{\partial^2}{\partial x^2} E(x) + (n^2(x)k_0^2 - \beta_0^2) E(x) = 0, \quad (2.3)$$

in which R_{UQ} is the distance between the point \mathbf{U} and an arbitrary point $\mathbf{Q}(0, y_Q, z_Q)$ of the exit plane, $\vec{\beta}_0$ has the direction of \vec{UQ} . β_0 is the propagation constant of the guided wave in the unperturbed planar guide. As an initial approximation, the small complex correction in the actual propagation constant of the guided wave inside the grating area is ignored, these corrections will be reconsidered in the next subsection. Φ_{in} is the phase difference of the guided wave at \mathbf{Q} relative to the phase at \mathbf{O} , and equals

$$\Phi_{in} = \beta_0(R_{UQ} - R_U). \quad (2.4)$$

If the distance R_U tends to infinity, the light beam becomes collimated. In that case, Eq.(2.4) must be replaced by

$$\Phi_{in} = \beta_0 z. \quad (2.5)$$

Since a step discontinuity exists between the unperturbed guide and the guide outside the FGC (see Fig. 2.1), the incident wave excites new waves at the FGC's outline. These consist of guided and radiated waves with TE- and TM-polarizations whose amplitudes are proportional to the corrugation depth [12]. In the following calculations, the corrugation depth is assumed small enough to neglect both those secondary waves and the phase step occurring in the incident wave because of the step discontinuity. This phase step will be reconsidered in Sec. 2.3. Our model can be readily extended to the case of a diverging guided TM mode as the incident wave. For that case, an expression for the wave function similar to Eq.(2.2) can be found (see Ref. [11]).

We aim at a design in which a uniform spherical wave, converging to a point $\mathbf{F}_0(f_0 \cos(\gamma_0), 0, f_0 \sin(\gamma_0))$ as shown in Fig. 2.2, is diffracted from the grating. The electric field vector \vec{E}_s of this spherical wave at \mathbf{Q} has the amplitude

$$E_s(0, y_Q, z_Q) = \frac{const.}{R_{F_0Q}} e^{-in_c k_0 (R_{F_0Q} - f_0)}, \quad (2.6)$$

where R_{F_0Q} is the distance between \mathbf{F}_0 and \mathbf{Q} , f_0 is the focal length of the FGC. The minus sign in front of the exponent of Eq.(2.6) indicates that the wave is convergent towards \mathbf{F}_0 .

The required grating pattern is determined from the phase difference Φ between the diverging guided wave and the required spherical wave converging to the point \mathbf{F}_0 . From Eqs.(2.4) and (2.6), Φ equals

$$\Phi = n_e k_0 (R_{UQ} - R_U) + n_c k_0 (R_{F_0Q} - f_0), \quad (2.7)$$

where $n_e = \frac{\beta_0}{k_0}$ is the effective refractive index. If R_U tends to infinity, Eq.(2.7) is replaced by

$$\Phi = n_e k_0 z + n_c k_0 (R_{F_0Q} - f_0). \quad (2.8)$$

The m -th grating line can be calculated from the grating pattern equation $\Phi = 2m\pi$. In reality, an FGC always causes some aberration in the spherical wave due to fabrication errors, such that a phase deviation $\Phi_{PD}(y, z)$ must be introduced here to describe this phenomena. Then the phase difference is modified into

$$\Phi' = \Phi + \Phi_{PD}. \quad (2.9)$$

2.3 Off-axis image formation and wavefront aberration

Although a nearly aberration-free FGC pattern can be designed and produced (according to Eq.(2.7)), deviations in the configuration outside the grating will degrade the focal spot quality. Therefore, it is necessary to estimate the limits of the allowable imperfections. Several causes affecting the image quality are:

- A wavelength shift in the incident wave: e.g. from λ_0 to λ' .
- Effective refractive index changes: The effective refractive index of the unperturbed guide may change from n_e to \tilde{n}_e due to the wavelength shift and to changes in the waveguide parameters, such as the refractive indices of the media (change to n'_c, n'_f, n'_s) and the average film thickness (change to t'_j). This causes a change from β_0 to β in the propagation constant of the unperturbed guide.
- The light source displacement: During the system alignment, the position of the light source may be shifted slightly from the designed position. Suppose then an off-axis line source along the x -direction passing through the point $\tilde{U}(0, -R_{\tilde{U}}\sin(\theta), -R_{\tilde{U}}\cos(\theta))$, as shown in Fig.2.3. Here, $R_{\tilde{U}}$ is the distance between the point \tilde{U} and the origin.

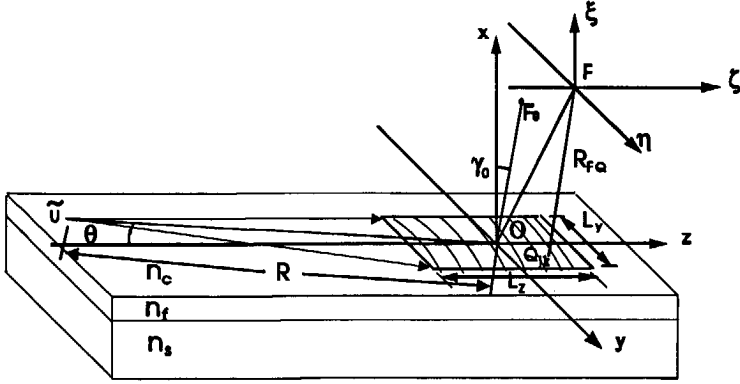


Figure 2.3: Image formation of using an off-axis diverging guided wave.

In this section and in Sec.3.7, the wavefront aberration and the tolerances related to these deviations will be discussed.

The phase difference Φ'_{in} of the incident guided wave between the points **Q** and **O** consists of three contributions. The first is simply due to the difference of two distances between each of those points and the source, if the whole path had the effective refractive index \tilde{n}_e of the unperturbed guide. The second contribution Φ_β accounts for the fact that between the source and the FGC's outline the actual refractive index is n'_e instead of \tilde{n}_e . Then, the third term Φ_{gr} accounts for the fact that, in the FGC-region, the actual effective index differs from \tilde{n}_e because β is changed into $\beta + \delta\beta(Q)$ by the presence of the grating. We write (see Eq.(2.4))

$$\Phi'_{in} = \beta(R_{OQ} - R_O) + \Phi_\beta + \Phi_{gr}(\delta\beta), \quad (2.10)$$

where $\beta = \tilde{n}_e k'$. Usually, the magnitude of $\delta\beta$ is four orders less than that of β . The quantity Φ_β is calculated from the difference in the distances measured from \tilde{U} to the intersections of the two rays \vec{UQ} and \vec{UO} with the front of the FGC at $z = -L_z$, multiplied by the difference of the propagation constant of the guided wave $n'_e k'$ outside the grating and that of the unperturbed guide β

inside. We obtain

$$\Phi_\beta = (n'_e - \tilde{n}_e)k' \left(\frac{L_z}{2} - R_{\tilde{v}} \cos(\theta) \right) \left\{ \sqrt{1 + \left(\frac{y_Q \cos(\theta) - R_{\tilde{v}} \sin(\theta)}{z_Q + R_{\tilde{v}} \cos(\theta)} \right)^2} - \sqrt{1 + \left(\frac{R_{\tilde{v}} \sin(\theta)}{R_{\tilde{v}} \cos(\theta)} \right)^2} \right\}. \quad (2.11)$$

If $R_{\tilde{v}}$ tends to infinity, $\Phi_\beta = (n'_e - \tilde{n}_e)k'[y_Q \tan(\theta) - z] \cos(\theta)$ and the first term at the right-hand side of Eq.(2.10) is replaced by $\beta z \cos(\theta)$. The last term in Eq.(2.10) will be calculated in Sec. 2.4.

If deviations of the configuration outside the FGC or fabrication errors of the FGC occur, the diffracted wave is aberrated and is no longer focused onto \mathbf{F}_0 . By introducing a new reference sphere with its center at the *point of reference* \mathbf{F} (which is determined by minimizing the wavefront aberration [13]), the field distribution of the wave at \mathbf{Q} is given by

$$\vec{E}'_s(Q) = \vec{E}_Q S(Q) e^{(-in'_c k'(R_{FQ} - f) + in'_c k'W)}, \quad (2.12)$$

where \vec{E}_Q is the complex amplitude vector which will be discussed in the next subsection. The pupil function S vanishes if \mathbf{Q} is outside the grating and equals unity within. f is the distance between \mathbf{F} and \mathbf{O} ; R_{FQ} is the distance between \mathbf{F} and \mathbf{Q} . By comparing the actual wavefront and the reference sphere, the wavefront aberration W can be obtained. The exponent in Eq.(2.12) is equal to

$$-in'_c k'(R_{FQ} - f) + in'_c k'W = -i(\Phi' - \Phi'_{in}). \quad (2.13)$$

The wavefront aberration has been calculated as [13]

$$W = \text{constant} - \tilde{\mu} \left\{ \frac{n_e}{n'_c} R_{UQ} + \frac{n_c}{n'_c} R_{F_0Q} \right\} + \left\{ \frac{\tilde{n}_e}{n'_c} R_{\tilde{v}Q} + R_{FQ} \right\} - \frac{\Phi_{FD}}{n'_c k'} + \frac{\Phi_\beta}{n'_c k'} + \frac{\Phi_{gr}(\delta\beta)}{n'_c k'}, \quad (2.14)$$

where $\tilde{\mu} = \frac{k_0}{k'}$; the constant term equals

$$\tilde{\mu} \left(\frac{n_e}{n'_c} R_U + \frac{n_c}{n'_c} f_0 \right) - \left(\frac{\tilde{n}_e}{n'_c} R_{\tilde{v}} + f \right). \quad (2.15)$$

Let the point Q be determined by the position vector \vec{R}_{OQ} , pointing from O to Q:

$$\vec{R}_{OQ} = \begin{bmatrix} x_Q \\ y_Q \\ z_Q \end{bmatrix} = \begin{bmatrix} 0 \\ r_Q \sin(\theta_Q) \\ r_Q \cos(\theta_Q) \end{bmatrix}, \quad (2.16)$$

where r_Q is the distance between the point Q and the origin O, θ_Q is the angle between \vec{R}_{OQ} and the unit vector \vec{k} .

Using the binomial expansion of R_{DQ} (D is either U, \tilde{U} , F_0 , or F), the wavefront deviation W can be written as

$$\begin{aligned} W = & -\frac{\Phi_{FD}}{n'_c k'} + \frac{\Phi_\beta}{n'_c k'} + \frac{\Phi_{gr}(\delta\beta)}{n'_c k'} + r_Q \left\{ \tilde{\mu} \left[\frac{n_e}{n'_c} a_U + \frac{n_c}{n'_c} a_{F_0} \right] - \left[\frac{\tilde{n}_e}{n'_c} a_{\tilde{U}} + a_F \right] \right\} \\ & - \frac{r_Q^2}{2} \left\{ \tilde{\mu} \left[\frac{n_e}{n'_c} \frac{1 - a_{\tilde{U}}^2}{R_U} + \frac{n_c}{n'_c} \frac{1 - a_{F_0}^2}{f_0} \right] - \left[\frac{\tilde{n}_e}{n'_c} \frac{1 - a_{\tilde{U}}^2}{R_{\tilde{U}}} + \frac{1 - a_F^2}{f} \right] \right\} \\ & - \frac{r_Q^3}{2} \left\{ \tilde{\mu} \left[\frac{n_e}{n'_c} \frac{a - a_{\tilde{U}}^3}{R_{\tilde{U}}^2} + \frac{n_c}{n'_c} \frac{a - a_{F_0}^3}{f_0^2} \right] - \left[\frac{\tilde{n}_e}{n'_c} \frac{a - a_{\tilde{U}}^3}{R_{\tilde{U}}^2} + \frac{a - a_F^3}{f^2} \right] \right\} + W_h, \quad (2.17) \end{aligned}$$

in which a_D follows from

$$a_D = m_D \sin(\theta_Q) + n_D \cos(\theta_Q) \quad (D = U, \tilde{U}, F_0, F), \quad (2.18)$$

where m_D and n_D are two components of the unit vector (l_D, m_D, n_D) along \vec{R}_{OD} . The terms of order r_Q^4 and higher are combined to the term W_h . Here, the constant term mentioned in Eq.(2.14) is exactly cancelled. The first term at the right-hand side of Eq.(2.17) may be represented by Zernike polynomials [14]:

$$\Phi_{FD} = \begin{cases} n_c k_0 \sum_{n=0}^N \sum_{l=1}^n A_{nl} R_n^l(r_Q) \sin(l\theta_Q) & (l > 0), \\ n_c k_0 \sum_{n=0}^N \sum_{l=-n}^0 A_{nl} R_n^l(r_Q) \cos(l\theta_Q) & (l \leq 0), \end{cases} \quad (2.19)$$

where N is the degree of the polynomial. According to Eq.(2.11), Φ_β contributes a small tilt to the wavefront aberration if the light source is far away from the grating, but appears to describe astigmatism when the light source

moves closer to the grating. This astigmatism term is approximately proportional to $(r_q \sin(\theta_q))^2$ and its magnitude is usually less than $\frac{\lambda'}{50}$. The third term in Eq.(2.17) also causes aberration in the final image of the FGC. Fortunately, it will appear to describe a uniform tilt only. After using the *displacement theorem* concerning a change of the reference sphere [15] to minimize this aberration, the remaining wavefront aberration is usually less than $\frac{\lambda'}{50}$. The displacement of the center of the reference sphere is in the order of $0.1\mu\text{m}$ in practical cases. The point of reference is chosen by minimizing the wavefront deviation while neglecting the second and third terms in Eq.(2.17). The off-axis image formation is characterized by [13]

$$\begin{bmatrix} m_F \\ n_F \end{bmatrix} = \tilde{\mu} \left(\frac{n_e}{n'_c} \begin{bmatrix} m_V \\ n_V \end{bmatrix} + \frac{n_c}{n'_c} \begin{bmatrix} m_{F_0} - A_{11} \\ n_{F_0} - A_{1-1} \end{bmatrix} \right) - \frac{\tilde{n}_e}{n'_c} \begin{bmatrix} m_{\bar{V}} \\ n_{\bar{V}} \end{bmatrix}, \quad (2.20)$$

$$\frac{1}{f} = \frac{1}{(1 + l_f^2)} \left\{ \tilde{\mu} \left[\frac{n_e (1 + l_V^2)}{n'_c R_V} + \frac{n_c}{n'_c} \left(\frac{(1 + l_F^2)}{f_0} + 8A_{21} \right) \right] - \frac{\tilde{n}_e (1 + l_{\bar{V}}^2)}{n'_c R_{\bar{V}}} \right\}. \quad (2.21)$$

Eq.(2.20) has been obtained by equalizing the coefficient of the first order term in r_q to zero, and specifies the direction of \overrightarrow{OF} . If, at the right-hand side of Eq.(2.21), the terms of order r_q^4 and higher are neglected, it appears that the only contributions independent of θ_q arise from the second-order terms. Minimizing the aberrations means that the sum of these terms must vanish. From Eq.(2.21) follows the length f of \overrightarrow{OF} . Now the position of \mathbf{F} has been specified, the remaining wavefront aberration can be calculated according to Eq.(2.14) without further approximation.

2.4 The field distribution of the focused wave in the exit plane

To calculate the field distribution of the focused wave, the FGC is divided into subgratings by covering it with a network consisting of $(J+1)$ radial lines and

($K+1$) circular arcs around the point \tilde{U} (note that in Eq.(2.12) the actual rectangular shape of the FGC is ascertained through the pupil function S). The radial lines are separated by equal angles ($d\varphi$) between subsequent lines, whereas the circular arcs shows equal increments (dr) in their radii of curvature (see Fig. 2.4a). Subsequent lines and arcs form meshes; we assume that their total numbers in the radial and tangential directions, J and K , to be even such that a distinct central point O (the origin of our coordinate system) occurs at the intersection of $j = \frac{J}{2} + 1$, $k = \frac{K}{2} + 1$. The network has nodes which are the intersections of the radial lines and the circular arcs. Around an arbitrary node Q_{jk} a corresponding subgrating G_{jk} exists as shown in Fig. 2.4b. That subgrating is delimited by lines at a distance from the k -th arc of $\pm \frac{dr}{2}$ in the r -direction and under an angle around the j -th line of $\pm \frac{d\varphi}{2}$ in the φ -direction.

The purpose of constructing this network in the exit plane is to determine the field amplitude $A(j,k)$ and the power $P(j,k)$ per unit length in the φ -direction, carried by the incident guided wave at the node Q_{jk} . In this dissertation, the amplitude distribution over the wavefront of the incident guided wave before entering the FGC is assumed to be uniform. Along a radial line, the fields at the nodes are calculated node after node, following the sequence of subgratings to increasing values of k . During the calculation, the diverging guided wave incident upon the nearly rectangular subgratings is locally regarded as collimated, supposing that the distance between the light source and the center of the FGC is much larger than the dimensions of the mesh.

As we explained in the Sec. 2.1, the subgrating can be approximated by a periodic and straight grating. The method from Ref. [10] is used to analyze grating couplers for waves at oblique incidence (*i.e.* the propagation direction of the incident guided wave and the grating vector are not parallel). In that paper, the profile function of a periodically corrugated surface of the waveguide could be expressed as a superposition of all possible harmonics such that the

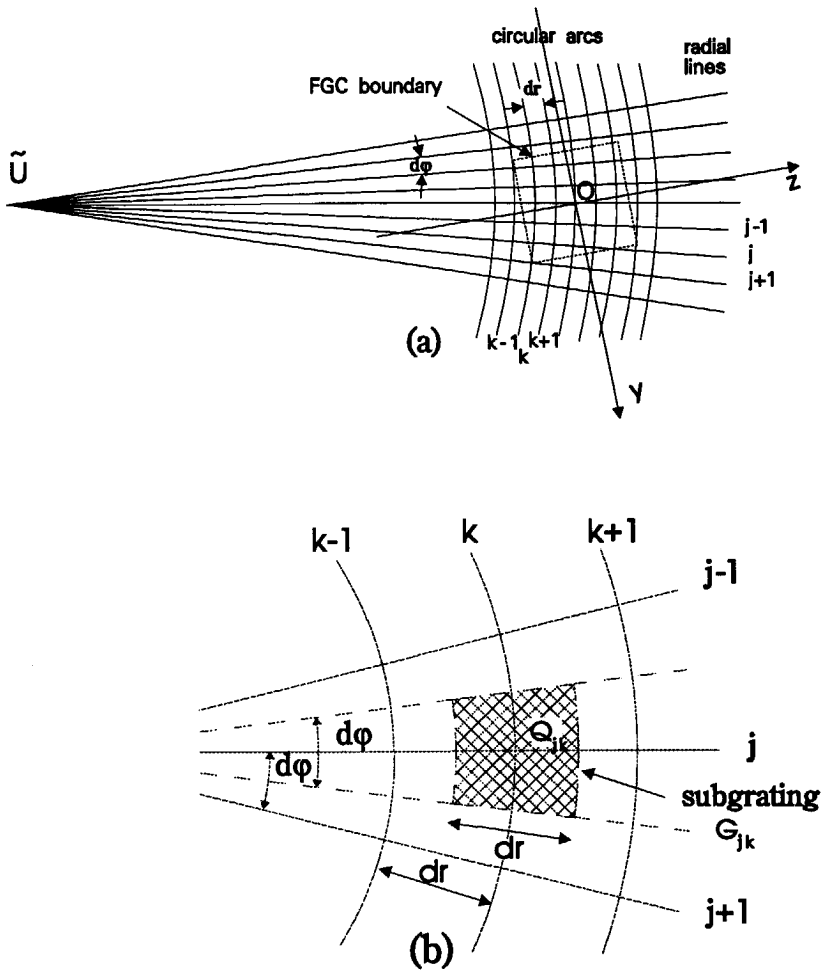


Figure 2.4: (a) Meshes composed of radial lines and circular arcs corresponding to a diverging guided wave, (b) the configuration of the subgrating G_{jk} .

field in the grating could be expressed by Floquet waves [16]; the equivalent boundary conditions were derived subsequently. In the case of oblique incidence, the incident guided TE-wave can couple to Floquet waves of TE-polarization as well as with Floquet TM-waves. However, the fields in each subgrating classified into TE- and TM-polarizations with respect to the local grating vector, must be transformed back to the global coordinates (x, y, z) . After the equivalent boundary conditions are applied at each interface of the waveguide, the complex amplitude vectors of the Floquet waves and the quantity $\delta\beta$ can be obtained. Therefore, the complex amplitude of the diverging guided wave along a radial line can be calculated by the amplitude transport equation:

$$A(j, k) = R_k A(j, k-1) e^{(\frac{1}{2}[\delta\beta(j, k-1) + \delta\beta(j, k)]dr)} \quad (j=1, 2, \dots, J; k=1, 2, \dots, K), \quad (2.22)$$

where $A(j, k)$ is the amplitude at Q_{jk} , $R_k = \sqrt{\frac{r_{k-1}}{r_k}}$, r_k being the radius of the k -th circular arc. For a collimated guided wave, $R_k = 1$. In Eq.(2.12), the complex amplitude vector \vec{E}_Q at Q_{jk} is equal to the sum of the complex amplitude vectors of the corresponding Floquet TE- and TM-waves multiplied by $A(j, k)$. Furthermore, \vec{E}_Q is linearly proportional to the corrugation depth [10]. Let $\delta\beta = \kappa + i\alpha$; κ is related to the phase correction Φ_{gr} and α is the attenuation coefficient. Eq.(2.22) can be split into two real equations

$$P(j, k) = (R_k)^2 P(j, k-1) e^{-[\alpha(j, k-1) + \alpha(j, k)]dr}, \quad (2.23)$$

$$\phi(j, k) = \left\{ \frac{\kappa(j, 1) + \kappa(j, k)}{2} + \sum_{m=2}^{k-1} \kappa(j, m) \right\} dr, \quad (2.24)$$

where $P(j, k) = |A(j, k)|^2$, ϕ is the phase increment due to the contribution of κ . From Eq.(2.10), the difference of the phase increment at Q_{jk} relative to that at \mathbf{O} is derived as

$$\Phi_{gr} = \phi(j, k) - \phi\left(\frac{J}{2} + 1, \frac{K}{2} + 1\right). \quad (2.25)$$

2.5 The field distribution around the focus

Once the field at each node is known, the field distribution around the focus can be obtained from a modified Huygens-Fresnel principle which operates with secondary plane waves, rather than with secondary spherical waves. A coordinate system (ξ, η, ζ) with its origin at the point of reference \mathbf{F} is introduced as shown in Fig. 2.3, the η -axis parallel to the y -axis and the positive ξ -direction parallel to the x -axis pointing away from the exit plane. An observation plane is chosen parallel to the exit plane, intersecting \overrightarrow{OF} at a point \mathbf{T} which not necessary coincides with \mathbf{F} , but lies nearby. The field \vec{E}_p with components (E_ξ, E_η, E_ζ) at a point $\mathbf{P}(\xi_P, \eta_P, \zeta_P)$ in the observation plane follows from [17]

$$\vec{E}_P(\xi_P, \eta_P, \zeta_P) = -i \frac{k'}{2\pi} \iint_{\Omega} R_{FQ} \vec{E}_Q[\vec{\sigma}(Q)] S(Q) e^{in'_c k' W} e^{in'_c k' \vec{\sigma} \cdot \vec{\rho}} d\Omega, \quad (2.26)$$

where $\vec{\sigma}$ denotes the unit vector with components $\sigma_x, \sigma_y, \sigma_z$ which are the direction cosines of \overrightarrow{QF} . $\vec{\rho}$ is the position vector of \mathbf{P} , Ω is the solid angle subtended by all σ -vectors.

Chapter 3

COMPUTATION RESULTS

3.1 Computational setup

Fig. 3.1 shows the flow chart of our computational setup based upon the model given in the previous sections. In our program, the change $\delta\beta$ is calculated node after node, then the field components and powers of the guided and the diffracted waves can be calculated. The power conservation is checked at each node by judging if the power decrement of the guided wave passing through the subgrating is equal to the power carried away by the diffracted waves. The former is calculated from α , the latter is calculated from the Poynting vectors of the diffracted waves. After the field components at all nodes have been calculated, the diffraction field in an observation plane around the point of reference can be calculated. By shifting the observation plane and with the aid of optimization, the *diffraction focus* F' (which is determined as the point where the maximum intensity occurs) can be determined uniquely if the wavefront aberration is small. In Sec. 3.4, it will be seen that the electric field E_η in the direction of the η -axis carries more than 88% of the electric field energy of the focused wave. Hence, for the determination of the diffraction focus only E_η is taken into consideration. Actually, E_η shows a single main peak only; more

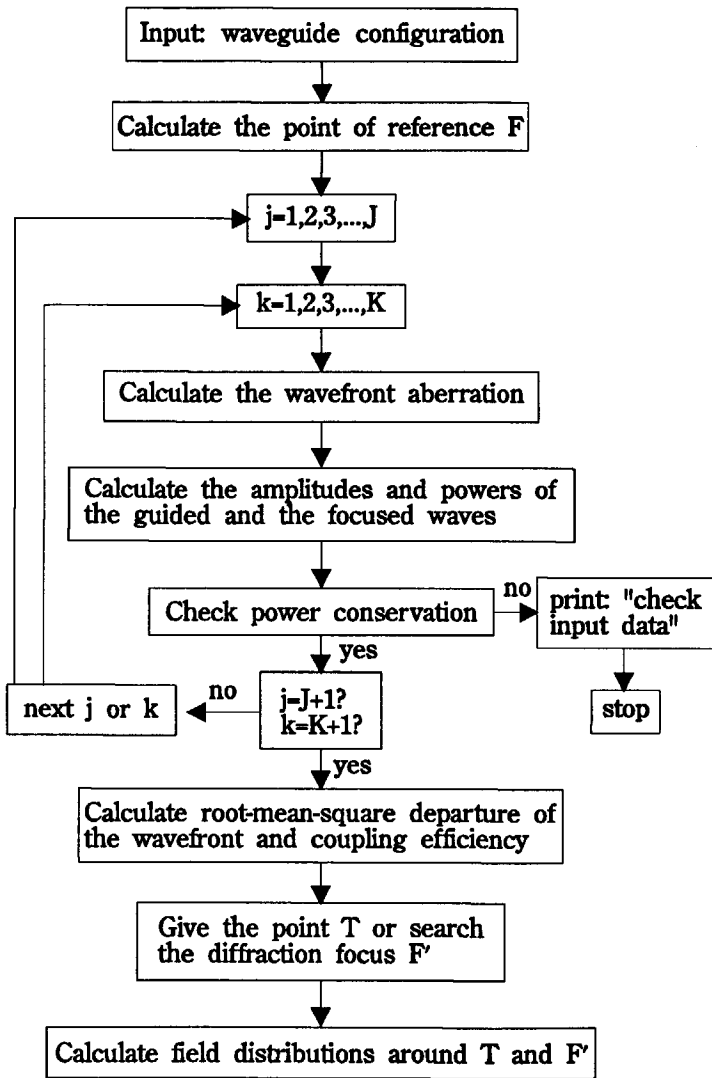


Figure 3.1: Flow chart of our computational setup.

(but much lower) peaks occur for the two other electric field components which cause a slightly broadening of the focal spot. In the presence of aberrations, the condition that the *root-mean-square departure* (RMSD) of the wavefront [15, 7] may not exceed $\frac{\lambda'}{14}$ can be used as a criterion for roughly judging the quality of the focal spot. A more accurate criterion is based upon the *Strehl intensity* $i(F')$ [15] which is a ratio of intensity at the diffraction focus in the presence of aberrations relative to that in the absence of aberrations. Following the conventional criterion [15], an FGC-system is considered to be well corrected if $i(F') \geq 0.8$. In Sec. 3.7, these two criteria will be compared in the evaluation of the tolerances of the FGC configuration. The coupling efficiency η^0 is defined as the power of the focused wave divided by the power of the incident guided wave. We define the focal spot diameter as the average of the sizes in the η - and ζ -directions of the region where the intensity drops to $\frac{1}{e^2}$ of the peak intensity. The focal spot diameter and the coupling efficiency η^0 are used to optimize the corrugation depth of the grating.

3.2 Comparison with earlier theories

In Ref. [9], Seligson provides a method to evaluate the field distributions in the exit plane and in an observation plane. His method is limited to the case that the incident guided wave is collimated, and neglects the quantity $\delta\beta$. Setting $\delta\beta = 0$ in Eq.(2.22), no attenuation of the incident guided wave inside the grating and no phase correction to the guided wave are taken into account. Besides, inaccuracies occur in that paper due to an inappropriate choice of the position of the exit plane and of the origin of the coordinate system. Here, we carry out the necessary corrections and compare the results. These corrections can be presented in two ways, as described below. Seligson's exit plane is defined as the film/substrate interface (see Fig. 2.1), located in the plane $x=0$ of a Cartesian coordinate system with its origin at the center of the FGC. The distance from

the plane $x=0$ to the plane at half-height of the corrugation ($x=h$) was defined as the film thickness. Outside the grating area the film thickness equals h , which is different from our thickness $t_f + \frac{t_g}{2}$. Some notations used in that paper are adopted here for convenient comparison. The entire grating pattern (see Eq.(A2) in Ref. [9]), which was designed to occur around the plane $x=0$, has been shifted in the positive x -direction to the plane $x = h$. In addition, Eq.(A10) of Ref. [9] contains an inaccuracy. The diffracted field expressed in terms of the vector potential $\vec{A}_I(x, y, z)$ in the cover is only valid in the region $x \geq h$, such that the vector potential in the exit plane ($x=0$) cannot be written as $\vec{A}_I(0, y, z)$. If the grating pattern is shifted as mentioned above, the vector potential of the focused wave in the plane $x=h$ can be obtained by using the method of the stationary phase, yielding

$$\vec{A}_I(h, y, z) = \tilde{\eta} \frac{R_x}{R_x - h} \vec{U}(q_y, q_z) e^{ik_0 q_c h} e^{-ik_0 R(y, z)}, \quad (3.1)$$

where $\tilde{\eta} = \frac{t_g}{4}$, R_x is the perpendicular distance from the focal point \mathbf{F}_0 in the design to the plane $x = 0$. $R(y, z)$ is the distance between \mathbf{F}_0 and a point \mathbf{Q} in the plane $x = 0$. (q_c, q_y, q_z) specify the wave vector pointing from \mathbf{Q} to \mathbf{F}_0 , where q_c is the transverse propagation constant in the cover. The factor $\frac{R_x}{(R_x - h)} e^{ik_0 q_c h}$ in Eq.(3.1) is our correction to Seligson's result. We will show that the argument of the y -component of the function $\vec{U} \exp(ik_0 q_c h)$ is almost constant across the FGC; then Eq.(3.1) entails that the focused wave will converge to a point which is shifted in the positive x -direction by a distance h relative to the point \mathbf{F}_0 . Furthermore, the amplitude of the wave is now multiplied by a factor $\frac{R_x}{(R_x - h)}$. Seligson noticed such a defocusing effect caused by a nearly paraboloidal wavefront across the FGC but did not calculate the exact defocusing.

Another way of correction is to redefine the exit plane and the origin of the coordinate system just as we did in Section 2.2. The grating pattern is designed at the exit plane and no shift occurs. By rewriting the field expressions in

Ref. [9] corresponding to these changes, one can prove that the final result of the vector potential in the exit plane is obtained as

$$\vec{A}_I(0, y, z) = \vec{\eta}\vec{U}(q_y, q_z)e^{ik_0q_c h}e^{-ik_0R(y,z)}. \quad (3.2)$$

This results corresponds to a diffracted field with a different amplitude and a different focus than that described by (3.1). The electric field can be obtained from the vector potential with the relation $\vec{E}_I = -\frac{\partial \vec{A}_I}{\partial t} = i\omega \vec{A}_I$, yielding

$$\vec{E}_I(0, y, z) = i\omega \vec{\eta}\vec{U}(q_y, q_z)e^{ik_0q_c h}e^{-ik_0R(y,z)}. \quad (3.3)$$

Now, we compare the results concerning the field distribution of the diffracted wave in the exit plane between our and Seligson's calculations, as given in Eqs.(2.12) and (3.3), respectively. The comparison has to be achieved under the condition $\delta\beta = 0$ and in the absence of configuration deviations inside or outside the FGC. In fact, the field of the focused wave obtained under these conditions is exactly the resultant field of the corresponding Floquet TE- and TM-waves. To compare Eqs.(2.12) and (3.3), we disregard the equal exponential factors containing the distance from \mathbf{Q} to \mathbf{F}_0 , as well as the pupil function. Then, introducing \vec{e}_s with the components (e_{sx}, e_{sy}, e_{sz}) as the remaining parts of the complex electric field strengths, we have

$$\vec{e}_s = \vec{E}_Q \quad \{\text{from Eq.(2.12)}\}, \quad (3.4)$$

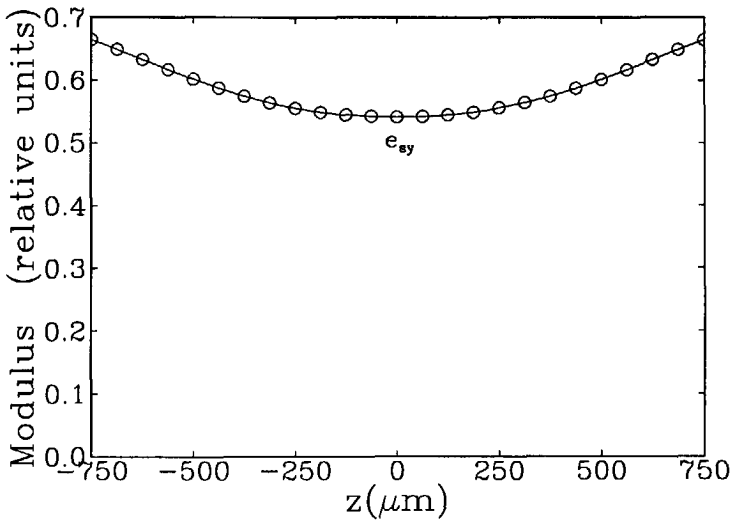
$$= -i\omega \vec{U}(q_y, q_z)e^{ik_0q_c h} \quad \{\text{from Eq.(3.3)}\}. \quad (3.5)$$

The example given in Ref. [9] is chosen as the example (see Table 3.1) for comparison of the numerical results. The direction cosines of \vec{OF} are chosen as $(1, 0, 0)$.

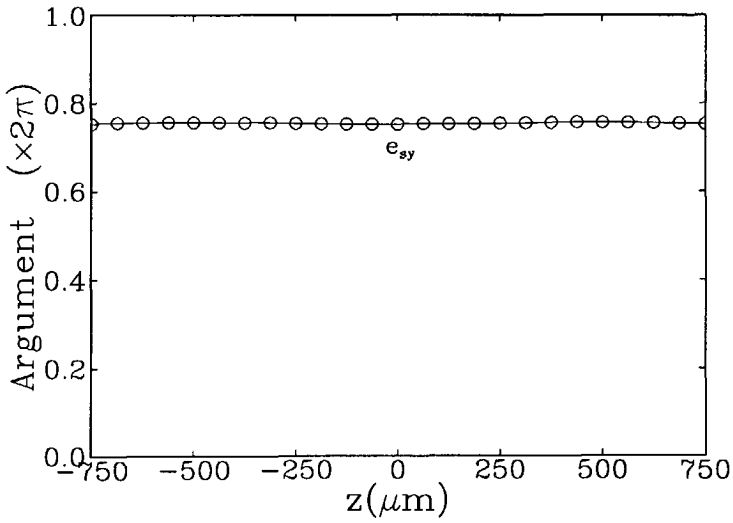
Table 3.1: waveguide parameters for the example

f	N.A.	grating aperture	λ'_0	t_f	n_c	n_f	n_s	n_e
1mm	0.6	$1.5 \times 1.5\text{mm}^2$	632.8nm	$0.9\mu\text{m}$	1.0	1.56	1.47	1.537

The results of calculating \vec{e}_s are presented in Figs 3.2-3.4, in which Seligson's and our results are shown by lines and symbols, respectively. These results appear to be identical. However, our method allows including a non-vanishing $\delta\beta$ such that the optimized corrugation depth of the grating can be determined. Fig. 3.2 shows the modulus and argument of e_{sy} along the z -axis. Due to normal incidence of the guided wave on the grating, the focused diffracted electric field components in the x - and z -directions vanish at the z -axis. The modulus of e_{sy} decreases from the edges at the z -axis toward the center of the grating and toward the edges at the y -axis as shown in Figs. 3.2 and 3.3. At the y -axis, no electric field exists in the z -direction (because the guided wave couples to radiated waves with a different (TM-) polarization with respect to the local grating vector) [10, 18]. Away from the y - and z -axes, all electric field components in the x -, y - and z -directions have non-vanishing values. Fig. 3.4 shows the moduli and arguments of the components of \vec{e}_s at $y = 750\mu m$. The modulus of e_{sz} increases toward the corners of the FGC and has maximum values at $x \pm y = 0$. Since the grating pattern is symmetric with respect to the z -axis, all moduli of the components of \vec{e}_s are symmetric with respect to that axis. The arguments of the components of \vec{e}_s are almost constant across the FGC except for the jumps of π in e_{sx} at the z -axis and in e_{sz} at the y - and z -axes (only point symmetry at the origin O). Those arguments (especially that of e_{sy}) are quite important for designing FGC's, extra aberrations may occur if those arguments are not constant. In Seligson's method, the actual grating was treated as a single entity, but in our model the grating is divided into subgratings. We have shown that in this case our the numerical results are identical with Seligson's, which indicates that these approximations are acceptable.

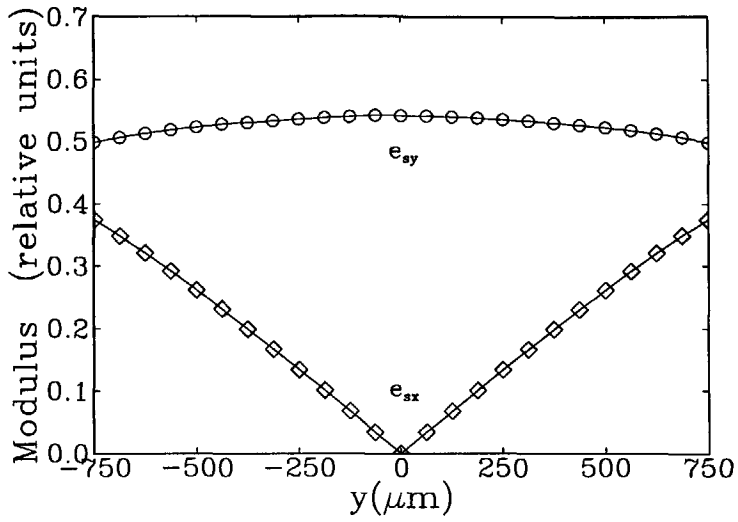


(a)

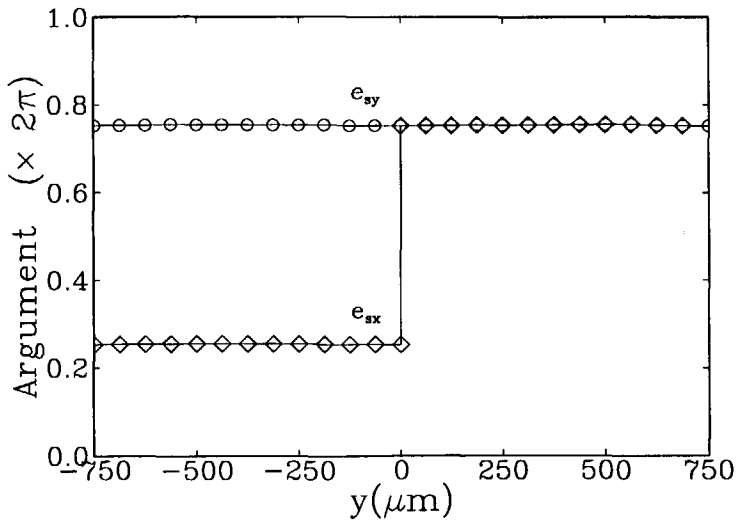


(b)

Figure 3.2: (a) Modulus and (b) argument of e_{sy} at the z -axis. Solid lines —: Seligson's results, symbols $\circ \circ \circ$: ours.

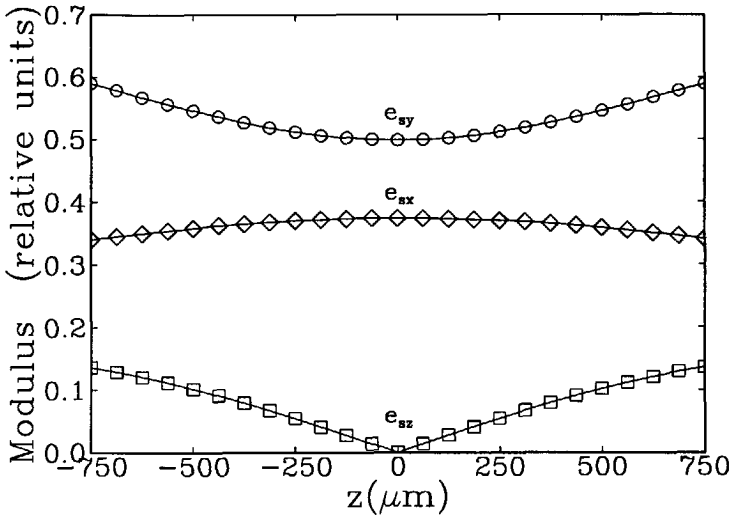


(a)

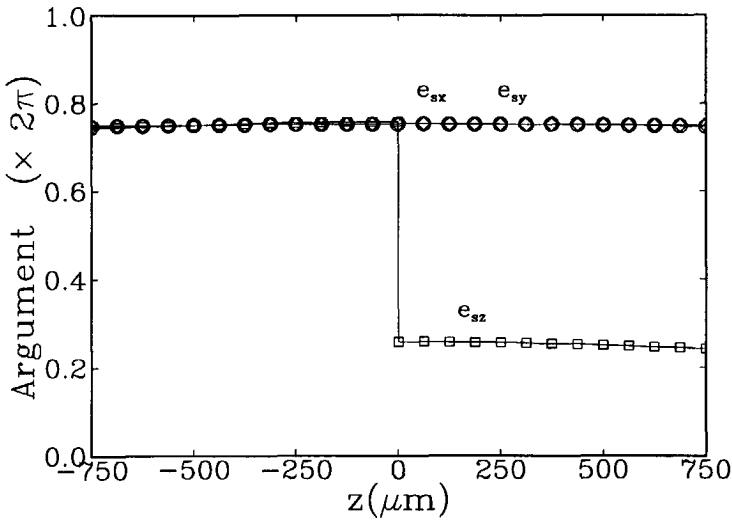


(b)

Figure 3.3: (a) Moduli and (b) arguments of e_{sx} and e_{sy} at the y -axis. Solid lines —: Seligson's results, symbols $\circ \circ \circ$, $\diamond \diamond \diamond$: ours.



(a)



(b)

Figure 3.4: (a) the modulus and (b) argument of e_{sx} , e_{sy} and e_{sz} at $y=750\mu m$.

Solid lines —: Seligson's results, symbols $\circ \circ \circ$, $\diamond \diamond \diamond$ and $\square \square \square$: ours.

3.3 Field distribution in the exit plane

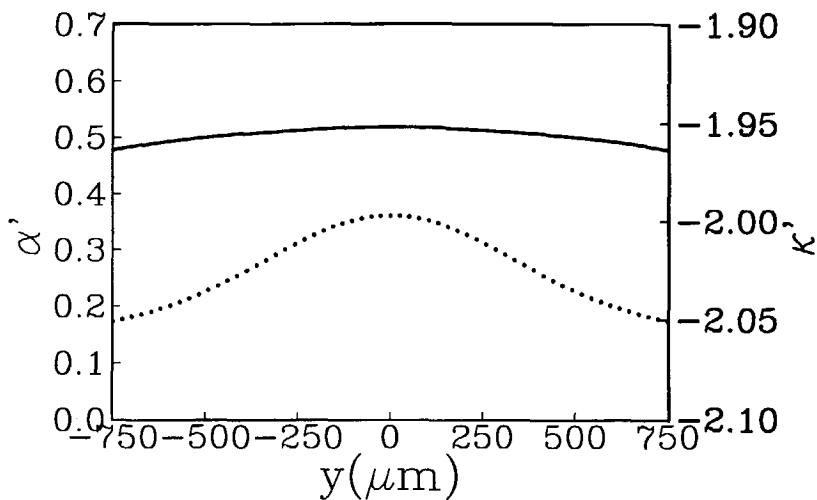
In our computation $\delta\beta$ will be obtained from the formulas in Ref. [10]. It can be proven that the formulas for calculating the amplitudes of the Floquet waves and $\delta\beta$ in Ref. [18] are equivalent to those obtained in Ref. [10]. The quantity $\delta\beta$ is proportional to $\tilde{\eta}^2$ [10, 18]. We define the normalized parameters α' and κ' from $\delta\beta = \kappa + i\alpha$ as

$$\alpha' = \frac{\alpha}{\lambda^3 |\tilde{\eta}|^2}, \quad \kappa' = \frac{\kappa}{\lambda^3 |\tilde{\eta}|^2}, \quad (3.6)$$

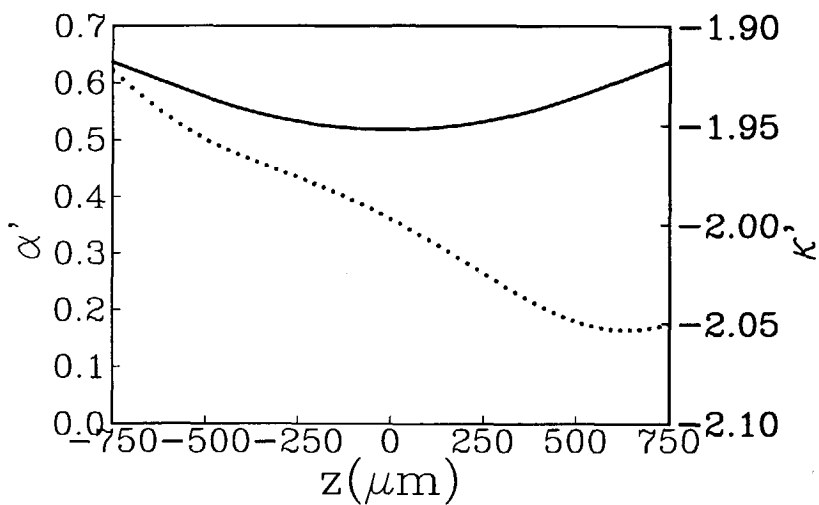
where α' and κ' are dimensionless and independent of the corrugation depth. The values of α' and κ' along the y - and z -axes are shown in Fig. 3.5. If $\delta\beta$ is taken into account, the precision of the field calculations in the exit plane and around the focus depends upon the numbers J and K . If they both exceed 40, the inaccuracy in the calculated field becomes insignificant (less than 0.5%). From now on, J and K are chosen as 50. Taking the corrugation depth as $60nm$ for the example given in Table 3.1, the statistical attenuation coefficient α_s , as calculated from the values at the nodes equals $20.9 \pm 1.4(dB/cm)$. The coupling efficiency is then 0.3. The moduli of the normalized complex amplitudes of the focused wave are shown for each field component in Fig. 3.6 (a)-(c). Because of the attenuation of the guided wave, the moduli have no symmetry around the plane $z=0$ but are symmetrical with respect to the plane $y=0$. The last two terms at the right-hand side of Eq.(2.10) contributes some aberration to the wavefront, the wavefront deviation in the exit plane appears to describe tilt only, as can be seen from the argument of E_{Q_y} shown in Fig. 3.6 (d).

3.4 Field distribution around the focus

Here, the field distribution in the observation plane, which contains the diffraction focus, will be calculated. By minimizing the wavefront aberration and



(a)



(b)

Figure 3.5: Values of α' (solid line) and κ' (dotted line) at the (a) y - and (b) z -axes.

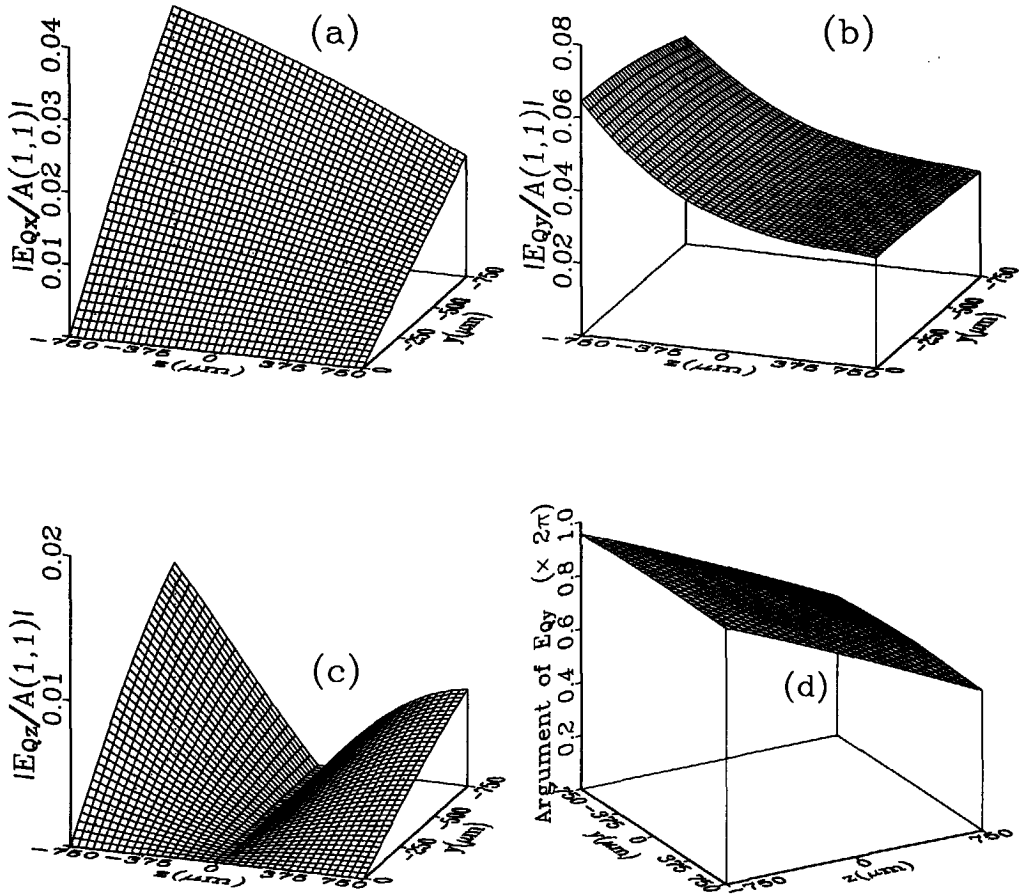


Figure 3.6: Moduli of the normalized complex field amplitudes of (a) E_{Qz} , (b) E_{Qy} and (c) E_{Qz} ; (d) the argument of E_{Qy} .

maximizing the focused intensity, we have computed that the point of reference and the diffraction focus occur at $(1\text{mm}, 0, 0)$ and $(1\text{mm}, 0, -0.22\mu\text{m})$ in the x, y, z -coordinate system, respectively. The wavefront aberration is a tilt (see Fig. 3.6 (d)), which causes the diffraction focus to be displaced over the (experimentally seen insignificant) distance of $0.22\mu\text{m}$ in the negative z -direction with respect to the point of reference. Fig. 3.7 shows the intensity distributions (normalized to the peak intensity of the η -component $I_{\eta F'}$) for the three field components in the plane $\xi = 0$. E_η carries 88.4% of the electric field energy

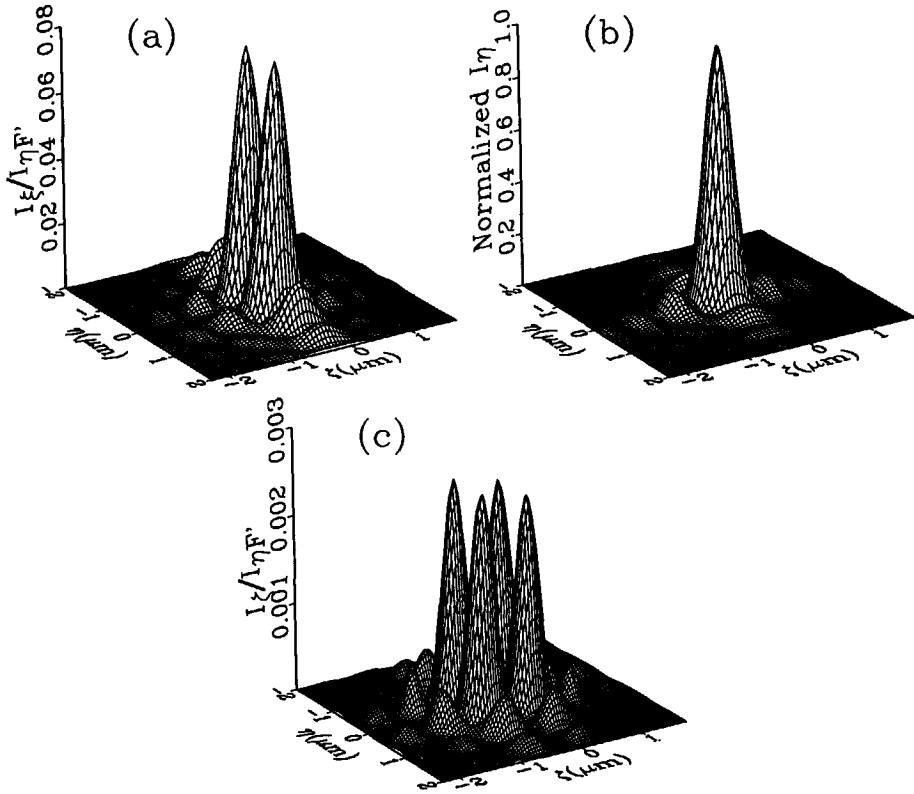


Figure 3.7: Intensity patterns for three electric field components (a) E_ξ , (b) E_η and (c) E_ζ .

of the focused wave; E_ζ transports 0.78% of the energy and shows four peaks, while E_ξ carries the remaining energy and shows two peaks. Those peaks can also be found in the field behind a spherical aplanatic lens [19], but there is some distinction between the FGC and such a lens. Behind the FGC, the intensity for E_η is a few per cent lower than that for the lens. In addition, the maximum intensity of the first side lobe behind the FGC is about five times as large as that behind the lens. This means that using the FGC more intensity is diffracted away from the central peak, such that the field distribution is broadened. These effects become more serious when the numerical aperture increases. In the ζ -direction, the side lobe nearest to the peak at the side of the light source is higher than the corresponding one at the other side. The intensities of the ξ - and ζ -components vanish at the ζ -axis due to the fact that the x - and z -components of the electric fields E'_{sx} and E'_{sz} in the exit plane are odd in y : $E'_{sz}(0, -y, z) = -E'_{sz}(0, y, z)$ and $E'_{sx}(0, -y, z) = -E'_{sx}(0, y, z)$. The focal spot diameter has been calculated as $0.76\mu m$. In that spot, E_η carries 19.4% of the input electric field energy of the incident guided wave.

3.5 The influence of the corrugation depth

The field amplitudes of the focused wave is proportional to the corrugation depth t_g , and the attenuation coefficient of the guided wave is proportional to t_g^2 . To obtain a high coupling efficiency, t_g should be chosen as large as possible. If the corrugation is chosen too large, however, the main peak of the diffraction field is broadened in the ζ -direction because the effective aperture of the FGC becomes smaller. Table 3.2 shows for the values $t_g = 68nm$, $80nm$ and $90nm$, the results for η^0 , for the average remaining power in the guided wave after passing through the FGC and for the ratio of the focal spot widths in the ζ - and η -directions at $\frac{1}{e^2}$ of the maximum intensity. In order to prevent the focal spot from broadening and to realize high coupling efficiency, we propose to

Table 3.2: The broadening effect of the focal spot as t_g increases

t_g	η^0	average remaining power	ratio of the spot widths of the guided wave
68nm	0.333	16.0%	1.045
80nm	0.362	7.7%	1.10
90nm	0.376	3.5%	1.21

optimize in future designs the corrugation depth until the average power of the guided wave decays to $\frac{1}{e^2}$ of input power after the wave passing the FGC.

3.6 The diffraction image in the presence of aberrations

Supposing the collimated guided wave to be obliquely incident upon the FGC under an angle of $\theta = 0.058^\circ$, the wavefront contains a combination of various aberrations among which coma is predominant. The point of reference and the diffraction focus occur at $(1mm, 1.6\mu m, 0)$ and $(1mm, 0.22\mu m, -0.21\mu m)$ in the x, y, z -coordinate system, respectively. The RMSD equals 0.22λ . The intensity distribution of E_η in the plane of $\xi=0$ is shown in Fig. 3.8. The Strehl intensity at the diffraction focus equals 0.8, such that the system can still be regarded as well-corrected.

In the following case, a diverging incident wave is incident upon a FGC which has the same parameters as in the previous example, except that the FGC is designed for this incident wave. A line source along the x -direction passing through U is supposed to be locate at $(0, 0, 15mm)$ in the x, y, z -coordinate system. This FGC has almost the same focusing characteristics as the FGC for the collimated incident wave, with practically the same η^0 , focal spot diameter and field distribution. In this example, the allowable limit for the light source shift along the

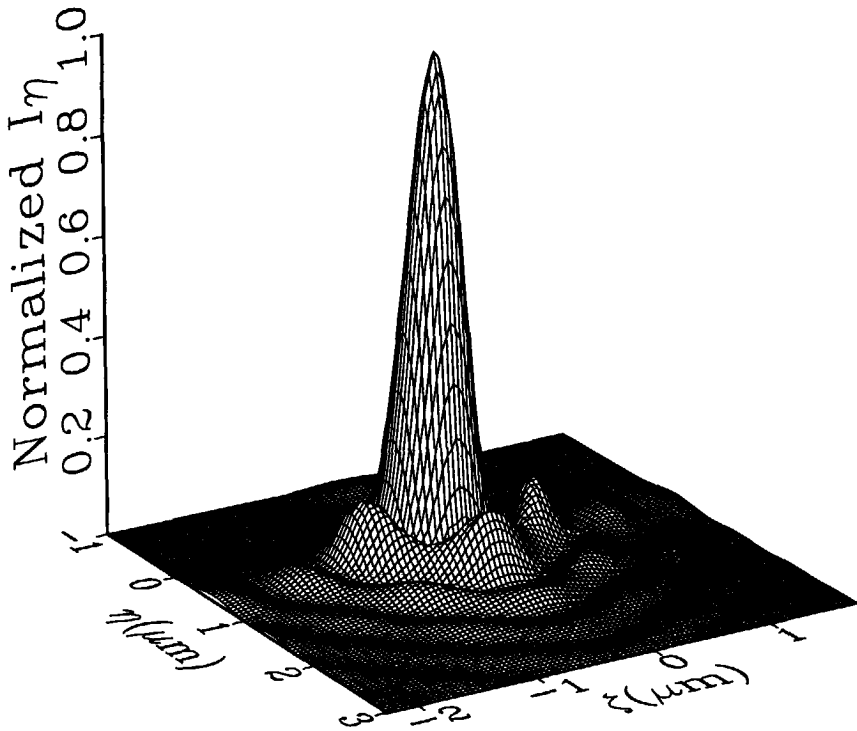


Figure 3.8: Intensity pattern for E_η if $\theta=0.058^\circ$.

negative z -axis is calculated as $125\mu m$, while $i(F')=0.8$. Under this condition, the point of reference and the diffraction focus occur at $(999.6\mu m, 0, 0)$ and $(999.6\mu m, 0, -0.2\mu m)$, respectively. The RMSD is calculated as 0.08λ . The intensity distribution for E_η is shown in Fig. 3.9. Astigmatism predominates in this case.

These two examples indicate that the quality of FGC's imaging is very sensitive to the incident wave configuration. For FGC's, coma and astigmatism are essential and considerable aberrations.

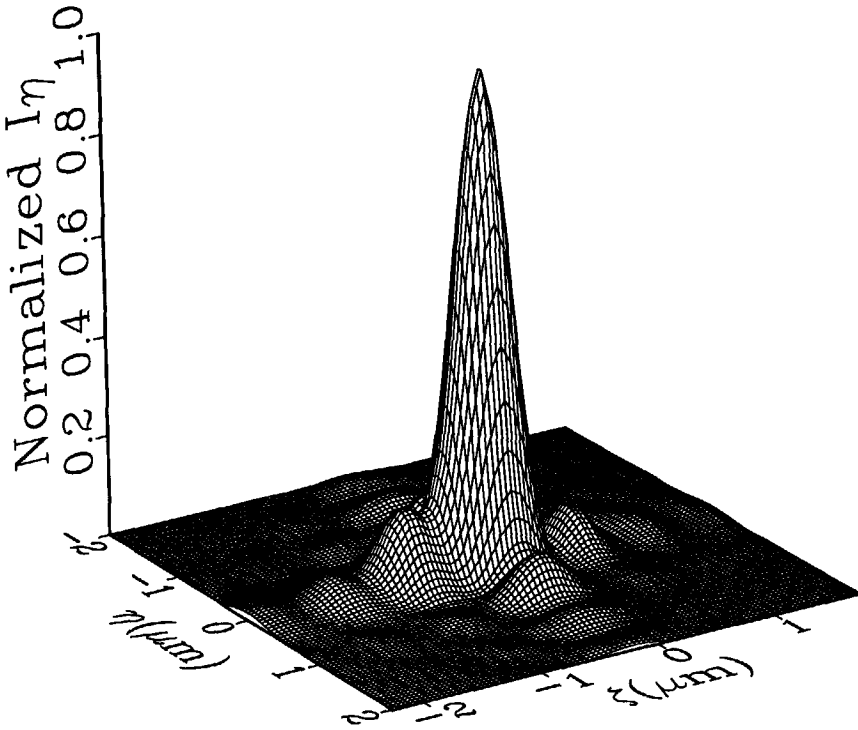


Figure 3.9: Intensity pattern for E_n if the diverging incident source is shifted over $125\mu\text{m}$ along the negative z -axis.

3.7 Tolerances for the FGC structure

Calculating allowable limits for each kind of deviation as introduced in Sec. 2.3 by imposing $i(F')=0.8$, provides information concerning the tolerances of an FGC related to these deviations. These tolerances are crucial and predict accuracy requirements of equipment for production and measurement of FGC's. The FGC's tolerances for the example of the diverging incident wave discussed in the previous subsection are given in Table 3.3.

Table 3.3: The parameter values for the example of the diverging incident wave, calculated for a Strehl intensity of 0.8

parameters	tolerances	RMSD (λ')	focal spot diameter (μm)	$\frac{(\tilde{n}_e - n_e)}{n_e}$
θ	0.053°	0.20	0.78	0
$t'_f - t_f$	$38.6nm$	0.20	0.77	9.2×10^{-4}
$\lambda' - \lambda$	5.5\AA	0.19	0.80	-2.0×10^{-5}
$R_v - R_u$	$125\mu m$	0.08	0.86	0

The criterion $\text{RMSD} \leq \frac{\lambda'}{14} \approx 0.07\lambda'$ would be less severe than the values in Table 3.3; but that criterion is inappropriate because it was obtained under the assumption that the field amplitudes are uniform across the exit plane [15].

Chapter 4

HOLOGRAPHICAL SETUP FOR RECORDING FGC'S

4.1 Basic setup

Electron beam techniques have been used to produce FGC's with near diffraction-limited performance [6]. However, it is difficult to make gratings larger than a few millimeters with existing *e*-beam equipment, because of stability problems [20]. Besides, it takes about 30 minutes to write a single FGC-pattern of $2 \times 2 \text{mm}^2$ while using *e*-beam writing [6]. Obviously, this throughput will be too low for future mass production. To overcome this drawback of *e*-beam writing, holographic techniques are chosen to produce FGC's. In general, the photoresist used to produce gratings with a periodicity around $0.25 \mu\text{m}$ by holographic techniques is only sensitive for wavelengths ranging from blue to far ultraviolet, whereas the applications for communication demand the use of red or infrared light. This makes it possible to use gratings in photoresist instead of gratings etched in the waveguide material. Our light source for recording holograms is an argon-ion laser (Spectra-Physics; model 2020-05) with the maximum output power of 400mW . The laser oscillates at a line within a narrow range of

wavelengths around $363.8nm$, selected with the aid of a prism in the cavity. From the frequency distribution (full width at half maximum) of $6GHz$ given in the operation manual of the argon laser, the linewidth is calculated to be $0.00265nm$. The optical cavity length of the laser is $1.1m$. From the resonance condition $\nu_m = \frac{mc}{2L}$ for a standing wave within the optical cavity, where ν_m is the frequency, c the speed of the light, L the optical cavity length, and m the (integer) mode number, the spacing of the longitudinal modes is $136.1MHz$. The FGC is recorded onto a chip which has been covered with photoresist, placed vertically in the setup of Fig. 4.1. The laser light is linearly polarized with the electric field in the vertical direction. The coherence length is about $50mm$. The beam diameter is $1.05mm$ at the exit pupil of the laser. The beam divergence is $0.53mrad$ (full angle). A He-Ne laser working at a wavelength of $632.8nm$ has been chosen as the reconstruction light source for demonstrating the operation of our FGC's.

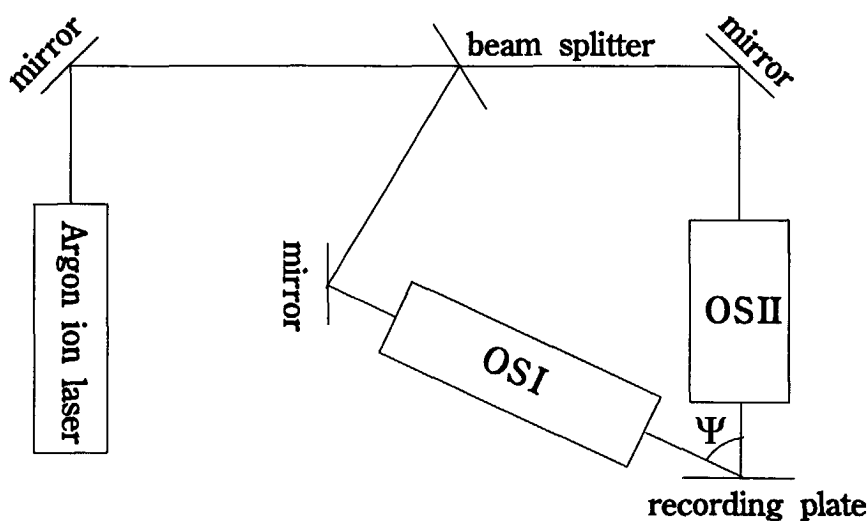


Figure 4.1: A schematic setup for making FGC's by holography.

4.2 The design method

Recording an FGC at one wavelength and reconstruction at another results in aberrations in the reconstructed beam which must be compensated either in the recording or in the reconstruction process. Similar aberration compensations, for a wavelength shift at reconstruction, have been described for the production of holographic optical elements (HOE's); [21, 22] describe the correction in the recording phase, [23] during reconstruction. In principle, the methods to design an optical system for producing a HOE can be applied directly to design the optics for making FGC's. The optical systems for recording (OS I and OS II in Fig. 4.1) may be composed of conventional objectives, HOE's or combinations of both. A method for designing an optical system consisting entirely of HOE's has been proposed [24]. Using HOE's has the advantage of low material costs, while their easy reproduction allows for a cheap duplication of the recording system. To produce those HOE's, however, other HOE's are required such that a sequence of subsequent recordings becomes needed; the intermediate steps are likely to introduce new aberrations by misalignment, which cannot easily be compensated for. That makes this design technique very difficult to use. For this reason, we propose a system of conventional lenses for the optical recording system. We restrict the discussion to an interference configuration in which one branch contains a collimating optical system (OS I in Fig. 4.1), while the other system (OS II) is designed such that the interference pattern at the recording plate has exactly the shape of the the required FGC-lines. Actually, the period and curvature of those lines now is determined by both the angle ψ between the branches and the divergence of the beam coming from OS II. In addition, this system has to be designed such that aberrations from a wavelength shift during reconstruction are compensated. From grating theory, the phase difference Φ (as seen in Eq.(2.8)) between the guided wave and the required focused wave diffracted by the FGC, determining the required grating pattern, equals the

phase difference $\tilde{\Phi}$ in the interference pattern during recording. This latter phase difference results from the plane wave from OS I and the wave from OS II. Then, the wavefront shape of the beam coming from OS II can be calculated; as performed in detail later in this section. If the phase of the reconstructed wave equals that of the collimated wave of Fig. 4.2, the wavefront aberration of the beam coming from OS II turns out to be spherical aberration only such that a rotationally symmetric system can be used to generate it. In the sequel, we'll

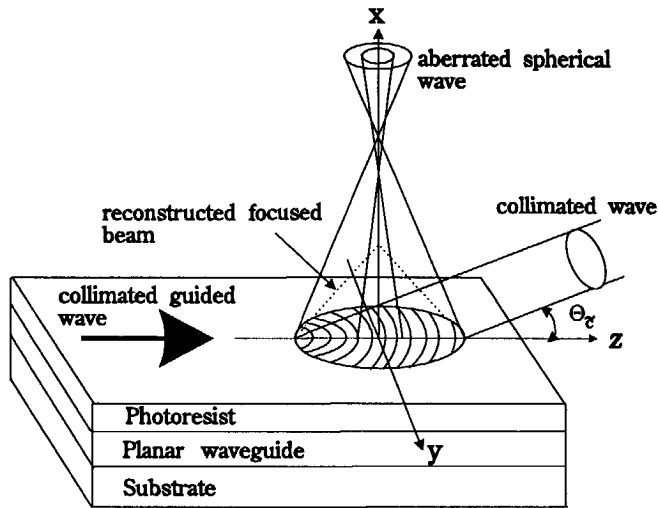


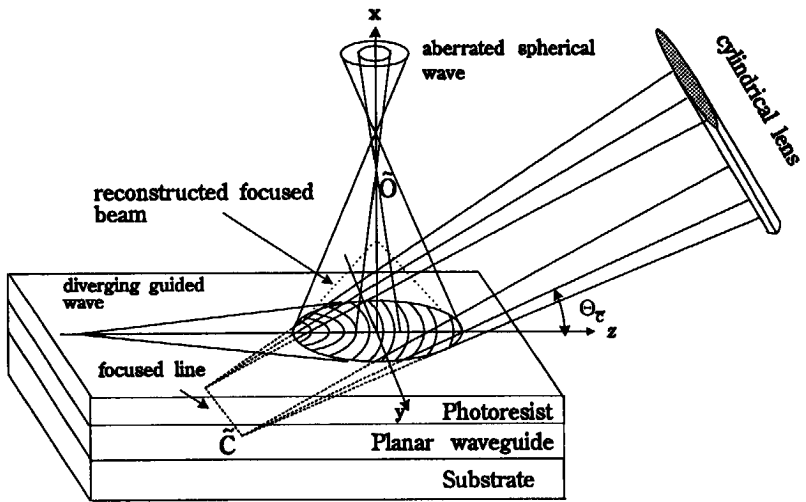
Figure 4.2: A schematic setup for making FGC's by holography using a collimated wave with an aberrated spherical wave.

often concentrate on the case that the guided wave is collimated. This means no loss of generality, since a guided wave beam which is originally diverging or converging can be collimated with the aid of an integrated waveguide grating lens [25, 26, 27], waveguide Fresnel lenses [28] or waveguide refracting lenses [29, 30].

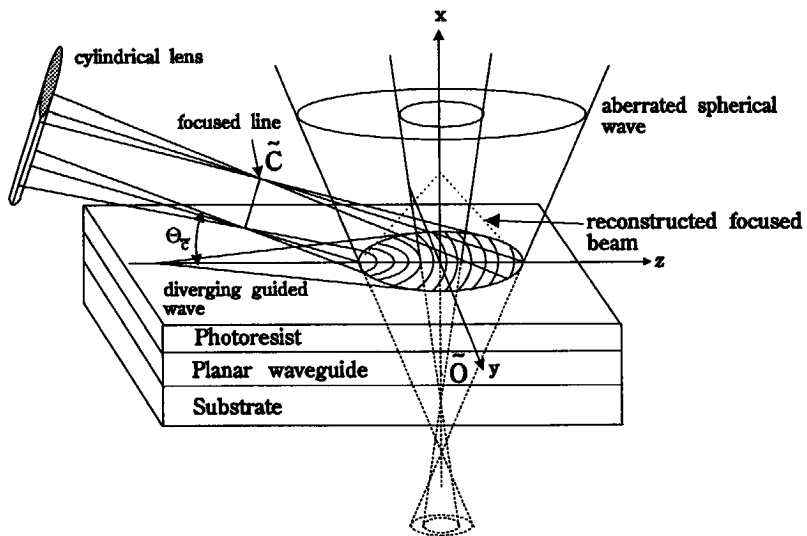
Actually, a design method useful for OS II-like systems, using ray optics, was first published in Ref. [22] for the purpose of producing HOE's. In another

publication [20], an equivalent but somewhat different method, starting from the phase matching between Φ and $\tilde{\Phi}$, led to more complicated calculations than Ref. [22] which, however, allows wider applications if at reconstruction the diffracted wave has to be astigmatic. In this section, the method of Ref. [20] will be extended for a diverging guided wave incident upon a FGC (without introducing the collimating components mentioned before). To cope with this divergence, the collimated wave from OSI in Fig. 4.1 has to be replaced by another wave form. In fact, the FGC appears to be produced by recording the interference pattern of a converging cylindrical wave (with a specific distance between its focused line and the center of the FGC) and an aberrated spherical wave, as described later in this section. The line source \tilde{C} of the cylindrical wave is located in the plane $y = 0$. Similar to the FGC for the collimated guided wave, the phase of the cylindrical wave can match the phase of the diverging guided wave at reconstruction by adjusting the tilt angle $\theta_{\tilde{C}}$ ($= 90^\circ - \Psi$) that the optical axis of the cylindrical wave makes with the recording plate, then the system OSII can be kept the same. Two different combinations of the systems OSI and OSII can, in principle, generate the same FGC pattern, but with aberrations of opposite signs, as shown in Figs. 4.3(a) and (b). The difference between these two system arrangements concerns the position of the paraxial focus of the aberrated spherical wave. If this focus occurs above the planar waveguide, the diverging wave shows a negative spherical aberration (as will be seen from Eq.(4.16)), similar to that of a positive lens. To our knowledge, no publication of experimental results has been reported about this kind of system arrangement. For the paraxial focus below the interference pattern, a near diffraction-limited performance of an off-axis HOE has been obtained at reconstruction with a shifted wavelength [22]. Heitmann and Ortiz [8] used this kind of system arrangement to produce FGC's, but made no attempt to correct aberrations.

The electric field in the recording plane ($x=0$) is the superposition of the



(a)



(b)

Figure 4.3: Proposed holographic setups for making FGC's (a) using a converging cylindrical wave with an aberrated diverging spherical wave (b) using a diverging cylindrical wave with an aberrated converging spherical wave.

cylindrical and the aberrated spherical waves; we have

$$E_h(Q) = E_{\tilde{C}}(Q)e^{-in_a k_h (R_{\tilde{C}Q} - R_{\tilde{C}})} + E_{\tilde{O}}(Q)e^{[in_a k_h (R_{\tilde{O}Q} - R_{\tilde{O}}) + in_a k_h W_{\tilde{O}}]} \quad (4.1)$$

(diverging wave),

$$= E_{\tilde{C}}(Q)e^{in_a k_h (R_{\tilde{C}Q} - R_{\tilde{C}})} + E_{\tilde{O}}(Q)e^{[-in_a k_h (R_{\tilde{O}Q} - R_{\tilde{O}}) + in_a k_h (-W_{\tilde{O}})]} \quad (4.2)$$

(converging wave).

Here n_a is the refractive index of air while $k_h = \frac{2\pi}{\lambda_h}$, λ_h being the recording wavelength. $E_{\tilde{C}}(Q)$ and $E_{\tilde{O}}(Q)$ are the amplitudes of the cylindrical and the aberrated spherical waves at an arbitrary point Q in the recording plane, respectively. For our holographic setup, $E_{\tilde{C}}(Q)$ and $E_{\tilde{O}}(Q)$ will be discussed in more detail in Sec. 4.4. $R_{\tilde{C}Q}$ is the shortest distance between Q and the line \tilde{C} . $R_{\tilde{C}}$ is the shortest distance between the origin O and \tilde{C} . In Eqs.(4.1) and (4.2), a reference sphere with its center at the point of reference \tilde{O} has been introduced to calculate the wavefront aberration $W_{\tilde{O}}$ ($-W_{\tilde{O}}$) due to the wavelength shift. This wavefront aberration is calculated by comparing the actual wavefront with the reference sphere. $R_{\tilde{O}}(Q)$ is the distance between \tilde{O} and Q . $R_{\tilde{O}}$ is the distance between the origin and \tilde{O} . The power transmission function $\tau(Q)$ of the recording after processing equals

$$\tau(Q) = E_{\tilde{C}}^*(Q)E_{\tilde{O}}(Q)e^{\pm in_a k_h (R_{\tilde{C}Q} - R_{\tilde{C}} + R_{\tilde{O}Q} - R_{\tilde{O}} + W_{\tilde{O}})} + \text{its complex conjugate}, \quad (4.3)$$

$$= 2|E_{\tilde{C}}^*(Q)E_{\tilde{O}}(Q)| \cos\{n_a k_h [R_{\tilde{C}Q} - R_{\tilde{C}} + R_{\tilde{O}Q} - R_{\tilde{O}}] + W_{\tilde{O}} \pm \arg(E_{\tilde{C}}^*(Q)E_{\tilde{O}}(Q))\}, \quad (4.4)$$

the plus sign applying to diverging and the minus sign to converging aberrated waves. The last term in the argument of the \cos -function in Eq.(4.4) is the argument of $E_{\tilde{C}}^*(Q)E_{\tilde{O}}(Q)$. This argument is the difference of the phase deformations coming from the systems OSI and OSII. Each phase deformation is the summation of all the phase changes occurring at the antirefraction coatings on the refracting surfaces in the systems OSI and OSII. That argument describes a wavefront aberration (which is a combination of defocusing, tilt and residual aberration) to the reconstructed beam, and can be disregarded if the residual

aberration is much smaller than the root-mean-square departure of $\frac{\lambda_h}{14}$. The phase recorded in the interference pattern $\tilde{\Phi}$ then equals

$$\tilde{\Phi} = n_a k_h (R_{\tilde{c}Q} - R_{\tilde{c}} + R_{\tilde{\delta}Q} - R_{\tilde{\delta}} + W_{\tilde{\delta}}) \pm \arg(E_{\tilde{c}}^*(Q)E_{\tilde{\delta}}(Q)). \quad (4.5)$$

Apart from the argument in Eq.(4.5), the patterns produced in the systems shown in Figs. 4.3(a) and (b) are the same. From Eq.(2.9), the phase difference Φ' between the diverging guided wave and the reconstructed wave must be equal to the phase difference $\tilde{\Phi}$; we have

$$\begin{aligned} n_e k_0 (R_{UQ} - R_U) + n_c k_0 (R_{F_0Q} - f_0) + \Phi_{PD} = \\ n_a k_h (R_{\tilde{c}Q} - R_{\tilde{c}} + R_{\tilde{\delta}Q} - R_{\tilde{\delta}} + W_{\tilde{\delta}}) \pm \arg(E_{\tilde{c}}^*(Q)E_{\tilde{\delta}}(Q)). \end{aligned} \quad (4.6)$$

Φ_{PD} describes the deviation from the phase in the designed interference pattern due to fabrication errors and equals

$$\begin{aligned} \Phi_{PD} = n_a k_h (R_{\tilde{c}Q} - R_{\tilde{c}} + R_{\tilde{\delta}Q} - R_{\tilde{\delta}} + W_{\tilde{\delta}}) - n_e k_0 (R_{UQ} - R_U) \\ - n_c k_0 (R_{F_0Q} - f_0) \pm \arg(E_{\tilde{c}}^*(Q)E_{\tilde{\delta}}(Q)). \end{aligned} \quad (4.7)$$

As will be seen in Fig. 4.10, the last term in Eq.(4.7) is mainly related to a defocusing combined with a negligible fourth-order spherical aberration while producing FGC's with a maximum numerical aperture of 0.5 in our system, no further optimization to minimize the defocusing and the aberration has been carried out. As an approximation, the last term in Eq.(4.7) is neglected and vanishing of the phase deviation Φ_{PD} is assumed during the system design. Then, from Eq.(4.7) we deduce

$$\begin{aligned} n_e k_0 (R_{UQ} - R_U) - n_a k_h (R_{\tilde{c}Q} - R_{\tilde{c}}) \\ = -n_c k_0 (R_{F_0Q} - f_0) + n_a k_h (R_{\tilde{\delta}Q} - R_{\tilde{\delta}} + W_{\tilde{\delta}}). \end{aligned} \quad (4.8)$$

For a spherical wave converging to a point F_0 as shown in Fig. 2.2, the angle γ_0 equals zero if the point obtained by projecting F_0 onto the plane $x=0$ coincides with the origin \mathbf{O} (the center of the FGC); otherwise, $\gamma_0 \neq 0$. For the same

focal length, the spherical wave is tilted with respect to that of $\gamma_0 = 0$ such that the FGC for $\gamma_0 < 0$ is decentered along the z -direction with respect to that for $\gamma_0 = 0$. An FGC that focuses the beam onto a point in the plane $y = 0$ outside the x -axis ($\gamma_0 \neq 0$) can be also constructed in the same optical system by using a decentered aperture masking, but then the length of the FGC, L_z , is reduced. Assuming $\gamma_0 = 0$, Eq.(4.8) can be rewritten in a more explicit form as

$$\begin{aligned} & n_e k_0 \{ \sqrt{[R_U + r_Q \cos(\theta_Q)]^2 + [r_Q \sin(\theta_Q)]^2} - R_U \} \\ & - n_a k_h \{ \sqrt{[R_{\tilde{c}} + r_Q \cos(\theta_Q) \cos(\theta_{\tilde{c}})]^2 + [r_Q \sin(\theta_Q) \cos(\theta_{\tilde{c}})]^2} - R_{\tilde{c}} \} \\ & = -n_e k_0 [\sqrt{f_0^2 + r_Q^2} - f_0] + n_a k_h [\sqrt{R_{\tilde{c}}^2 + r_Q^2} - R_{\tilde{c}} + W_{\tilde{c}}], \end{aligned} \quad (4.9)$$

where $\theta_{\tilde{c}}$ is the tilt angle of the cylindrical wave with respect to the yz -plane.

If the left-hand side of Eq.(4.9) vanishes, the wavefront aberration of the system OS II is a spherical aberration only such that a rotationally symmetrical system can be used to generate it. This left-hand side of Eq.(4.9) vanishes if:

$$\cos(\theta_{\tilde{c}}) = \frac{n_e \lambda_h}{n_a \lambda_0}, \quad (4.10)$$

and

$$R_{\tilde{c}} = R_U \cos(\theta_{\tilde{c}}). \quad (4.11)$$

These conditions express a phase-matching of the cylindrical and the diverging guided waves. For a typical case of $\lambda_0 = 632.8 \text{ nm}$, $\lambda_h = 363.8 \text{ nm}$ and $n_e = 1.58$, the angle $\theta_{\tilde{c}}$ is 24.722° . If R_U tends to infinity (*i.e.* a collimated guided wave), the cylindrical wave can be replaced by a collimated beam ($R_{\tilde{c}}$ tending to infinity) such that Eq.(4.9) is changed into

$$\begin{aligned} & n_e k_0 z - n_a k_h z \cos(\theta_{\tilde{c}}) \\ & = -n_e k_0 [\sqrt{f_0^2 + r_Q^2} - f_0] + n_a k_h [\sqrt{R_{\tilde{c}}^2 + r_Q^2} - R_{\tilde{c}} + W_{\tilde{c}}]. \end{aligned} \quad (4.12)$$

The system OS I can be orientated such that the angle with respect to the plane $x = 0$ equals $\theta_{\tilde{c}} = \cos^{-1}(\frac{n_e \lambda_h}{n_a \lambda_0})$ to match the phase of the collimated guided wave.

If Eqs.(4.10) and (4.11) are satisfied, Eq.(4.9) becomes

$$n_c k_0 (\sqrt{f_0^2 + r_Q^2} - f_0) = n_a k_h (\sqrt{R_{\tilde{O}}^2 + r_Q^2} - R_{\tilde{O}} + W_{\tilde{O}}). \quad (4.13)$$

Eq.(4.13) expresses a phase-matching of the focused wave in the reconstruction process and the aberrated spherical wave during recording.

Using the binomial expansion, the wavefront aberration $W_{\tilde{O}}$ can be written as

$$W_{\tilde{O}} = \frac{1}{2n_a k_h} \left(\frac{n_c k_0}{f_0} - \frac{n_a k_h}{R_{\tilde{O}}} \right) r_Q^2 - \frac{1}{8} \left(\frac{n_c k_0}{f_0^3} - \frac{n_a k_h}{R_{\tilde{O}}^3} \right) r_Q^4 + \dots \quad (4.14)$$

Minimizing the wavefront aberration such that the second order term in r_Q vanishes, the point of reference \tilde{O} is found from

$$R_{\tilde{O}} = \frac{\lambda_0 n_a}{\lambda_h n_c} f_0. \quad (4.15)$$

Then, Eq.(4.14) becomes

$$W_{\tilde{O}} = -\frac{1}{8n_a k_h} \left(\frac{n_c k_0}{f_0^3} - \frac{n_a k_h}{R_{\tilde{O}}^3} \right) r_Q^4 + \dots \quad (4.16)$$

The r_Q^4 and higher order terms represent spherical aberration and must be compensated. This compensation will be discussed in more detail later in this section. If the phase in the reconstruction process given at the left-hand side of Eq.(4.13) is expressed in terms of the recording wavelength, we have

$$n_c \frac{2\pi}{\lambda_0} (\sqrt{f_0^2 + r_Q^2} - f_0) = n_p \frac{2\pi}{\lambda_h} [n_a (\sqrt{f_0^2 + r_Q^2} - f_0)], \quad (4.17)$$

where $n_p = \frac{n_c \lambda_h}{n_a \lambda_0}$; $n_p < 1$ in our previous example. The optical path in the recording beam from system OS II is, as compared to that in the reconstructed beam, exactly scaled down by a factor of the wavelength ratio $\frac{\lambda_0}{\lambda_h}$. As seen from the right-hand side of Eq.(4.17), that phase can be obtained by a spherical wave with a wavelength of λ_h which diverges from a point at the back side of a fictitious plane plate to its front side if the plate's refractive index and thickness are n_p and $n_a f_0$, respectively. From Eqs.(4.17) and (4.13), the

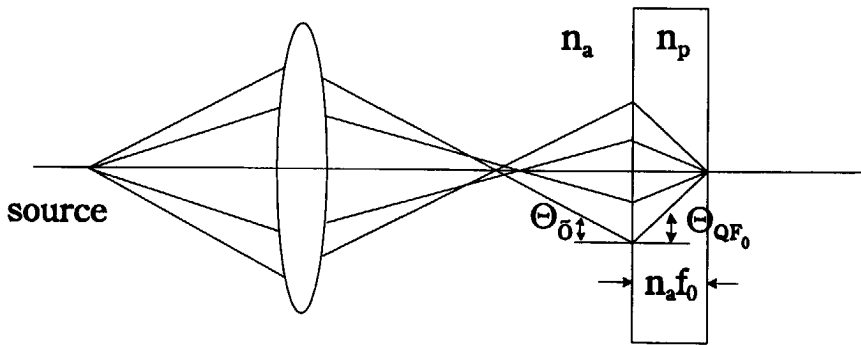
spherical aberration in Eq.(4.16) can be exactly compensated by introducing such a fictitious plane plate, placed at the exit plane of the FGC (the plane $x=0$) during the optimization of an optical system design. As shown in Figs. 4.4(a) and (b), this technique can be used to design a system for both cases: diverging as well as converging spherical waves (see Fig. 4.3). The rays which are refracted at the exit plane propagate to the virtual focus which coincides with the required focus F_0 . However, the optical path length in the fictitious plate is negative for the diverging spherical wave (opposite sign as the wavefront aberration of the diverging wave as given in Eq.(4.1)), but positive for the converging one such that, tracing a single ray from the point source through the OS II to the virtual focus, the difference between the optical ray path and that for the ray along the optical axis of the system is always kept zero.

As proven in Ref. [22], a relationship similar to Snell's law can be derived:

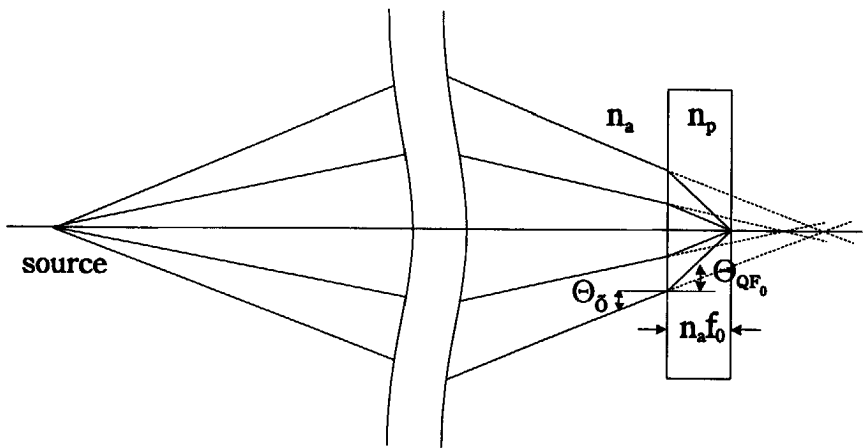
$$\sin(\theta_{\hat{o}}) = n_p \sin(\theta_{QF_0}). \quad (4.18)$$

where θ_{QF_0} is the angle that the ray $\overrightarrow{QF_0}$ makes with the normal to the yz -plane at Q . $\theta_{\hat{o}}$ is the angle that the ray normal to the aberrated wavefront makes with the normal to the yz -plane at Q , as shown in Fig. 4.4.

For producing an FGC with $N.A. = 0.7$, the recording optics must have a numerical aperture of 0.4 at the image side (calculated from Eq.(4.18), if $n_p = 0.57$). Correction of the spherical aberration for such a high numerical aperture system is difficult because a considerable spherical aberration of very high order occurs. With a slight reduction in numerical aperture, the system OS II can be simplified. A way to reduce the numerical aperture of the system OS II without losing the numerical aperture of FGC's is to use a laser light with a shorter wavelength in the recording process.



(a)



(b)

Figure 4.4: Using a fictitious plate as a design technique to optimize an optical system (a) for a diverging spherical wave (b) for a converging one.

4.3 The design of the optical systems

As discussed in preceding section, two possibilities exist (see Fig. 4.3) for the system arrangement to produce the same interference pattern for a good point-shaped focus at the back side of the fictitious plane plate. Their difference can be expressed as:

- (a) a negative spherical aberration if the paraxial focus occurs in front of the plate;
- (b) a positive spherical aberration if the paraxial focus occurs behind the plate.

However, situation (b) cannot be generated by a simple positive lens. To create situation (a), our holographic setup must have a similar arrangement as shown in Fig. 4.3(a). In the following account, the cylindrical wave is replaced by a collimated one because of the use of a collimated guided wave in our experiments. Using the design technique announced in the preceding section, the design of system OS II was achieved with the aid of the optical design program OPTSYS [31]. FGC's are to be recorded holographically at the wavelength of $363.8nm$, and to be used at the wavelength of $632.8nm$ for coupling a focused wave out of the waveguide from an incident collimated guided wave. The total system was designed to produce FGC's with the focal length of $2mm$. During the optimization of the system design, a fictitious plate (as mentioned in Sec. 4.2) was thought in the exit plane of the FGC. Its refractive index and thickness of the fictitious plane plate were taken as 0.574905 and $2mm$, respectively. The wavefront aberration caused by the wavelength shift between the recording and reconstruction processes was calculated from Eqs.(4.14) and (4.15) and is shown in Fig. 4.5. The system OS II, which consists of five lenses as shown in Fig. 4.6, has been designed to generate this required wavefront aberration as closely as possible. The lens parameters of the eventual design are listed in Table4.1. The system has been corrected up to $N.A. = 0.32$ to allow recording of FGC's with a

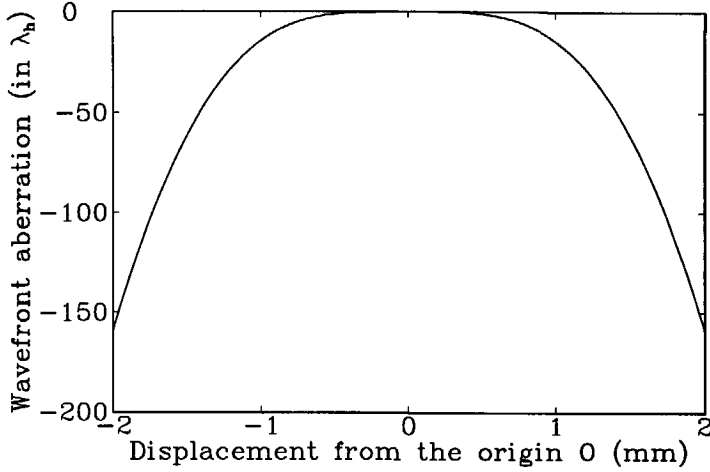


Figure 4.5: The spherical aberration caused by the wavelength shift, and required to be generated by the system OS II.

maximum numerical aperture of 0.55. The residual wavefront error W_{er} (being the deviation from the required wavefront at the front surface of the fictitious plane plate) of this system as a function of $\sin(\theta_{QF_0})$, calculated for $363.8nm$ in air, is shown in Fig. 4.7. The residual wavefront error at the reconstruction wavelength is found by multiplication with the wavelength ratio $\frac{\lambda_0}{\lambda_h}$ (not scaled down by the same factor as stated in Ref. [20]). If this error is expressed in Zernike polynomials (see Eqs.(2.19)) by a least square fitting [14], it can be fed back to our computational program to compute the related phase deviation Φ_{PD} (see Eqs.(2.9) and (4.7)) for analyzing its influence on the field distribution around the focus. Here, W_{er} is expressed as two polynomials:

$$\begin{aligned}
 W_{er} &= \sum_{n=0}^N A_{n0} R_n^0(\rho) \quad (n \text{ is even}, 0 \leq \rho \leq 1), \\
 &= \sum_{n=0}^N C_n \rho^n,
 \end{aligned} \tag{4.19}$$

Table 4.1: The parameter values of the system OSII optimized for an axial point object source at a distance 137.165mm in front of the system

Lens no.	Thickness(mm)	Radius of curvature (mm)	Refractive index
L_1	7.893	-33.333/-23.44	1.53674(BK7)
Air gap	7.834		1.00000
L_2	9.320	-10.72/-14.45	1.53674(BK7)
Air gap	5.998		1.00000
L_3	6.001	104.71/-87.1	1.53674(BK7)
Air gap	0.820		1.00000
L_4	5.955	32.25/186.2	1.53674(BK7)
Air gap	0.100		1.00000
L_5	5.200	15.85/29.51	1.53674(BK7)
Air gap	19.810		1.0000

where N is the degree of the Zernike polynomials. $\rho = \frac{r_Q}{r_{Q,max}}$, $r_{Q,max} = 2mm$ is the maximum value of r_Q . For a rotationally symmetric wavefront, the superscript l in the radial components $R_n^l(\rho)$ of the Zernike polynomials equals zero and n has even values only. $R_0^0(\rho)$ is a constant term. $R_2^0(\rho)$ describes the defocusing. The terms of order $R_4^0(\rho)$ and higher describe third order and higher order spherical aberrations, respectively. The coefficients of these polynomials are given in Table 4.2.

The optical system turned out very difficult to produce because of critical tolerances concerning decentering and tilt (see Table 4.3), and difficulties to make the required wide-band antireflection coating. To overcome the problem of decentering, the second lens L_2 is chosen to be slightly adjustable in the directions perpendicular to the axis such that additional aberrations resulting from assembly inaccuracies could be compensated. Since the system has a

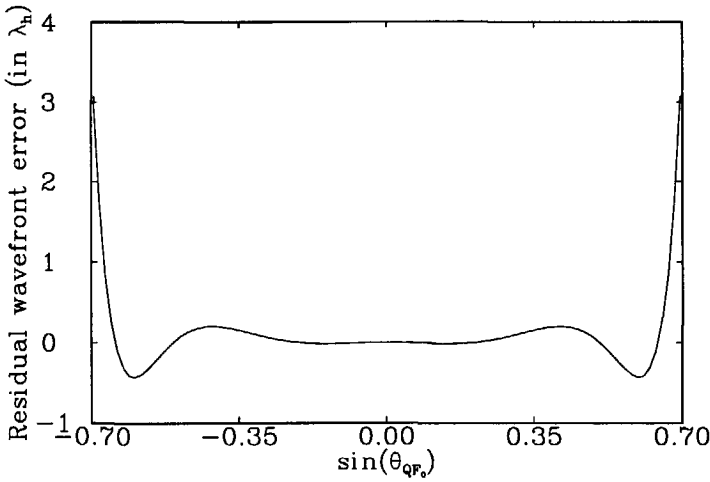


Figure 4.7: The residual wavefront error of the system OS II calculated at the wavelength of $363.8nm$ in air.

considerable spherical aberration, it is impossible to adjust the lens directly because the focal spots is always large. A correcting lens is placed in front of the system to obtain a well-corrected image for adjusting the lens (see Fig. 4.8). The system working with the correcting lens has been corrected up to $N.A. = 0.29$ for a light source with a wavelength ranging from $363.8nm$ to $632.8nm$ by changing the distance between the lens and the system. Fig. 4.8 shows the marginal rays

Table 4.2: The coefficients of the polynomials for the best fit of the residual wavefront error W_{er} (units: meter).

$A_{0\ 0}$	$A_{2\ 0}$	$A_{4\ 0}$	$A_{6\ 0}$	$A_{8\ 0}$	$A_{10\ 0}$	$A_{12\ 0}$	$A_{14\ 0}$
1.674×10^{-7}	4.413×10^{-7}	6.188×10^{-7}	4.357×10^{-7}	2.109×10^{-8}	-4.732×10^{-8}	1.796×10^{-8}	-4.454×10^{-9}
C_0	C_2	C_4	C_6	C_8	C_{10}	C_{12}	C_{14}
0	-4.474×10^{-7}	1.339×10^{-5}	6.962×10^{-5}	1.393×10^{-4}	-1.358×10^{-4}	7.01×10^{-5}	-1.528×10^{-5}

Table 4.3: The fabrication tolerances calculated for the system OSII with $N.A. = 0.32$, in which maxima of $25\mu m$ have been set for the uncritical tolerances that are indicated by a dot .

Lens no.	Thickness error (μm)	Error in radius of curvature (Newton's rings)	Decentering error (μm)	Tilt ($m rad$)	Axial element displacement (μm)
L_1	25.	3	8	2.0	25.
L_2	9	2	8	0.2	25.
L_3	25.	3	15	2.0	25.
L_4	25.	3	25.	2.0	25.
L_5	25.	3	4	0.2	25.

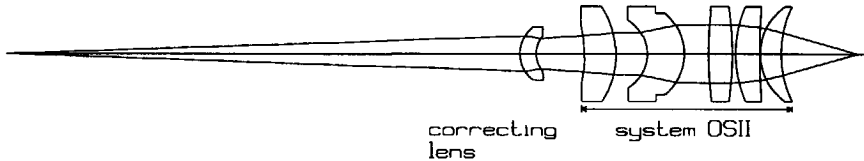


Figure 4.8: A lens used to correct the aberration of the system OS II during the alignment at the wavelength of $632.8nm$.

from an axial point source with a wavelength of $632.8nm$. The parameters and fabrication tolerances of the correcting lens are given in Table.4.4.

Although the correcting lens has been optimized for use at a wavelength of $363.8nm$, normal microscopes cannot be used to observe the image point directly because of the excitation of fluorescent light. The light of the He-Ne laser is aligned to the light path of the UV beam as closely as possible such that the correcting lens can be used for the adjustment with microscopic observation. The correcting lens and the most critical lens (L_2) in system OS II must have very low reflectances under an angle of incidence up to 45° at the

Table 4.4: Parameter values and fabrication tolerances of the correcting lens optimized for an axial point source at a distance of $138.241mm$ in front of the lens and an image formed at a distance of $18.988mm$ behind the last surface of the system OS II.

Parameters			
	Thickness(mm)	Radius of curvature(mm)	Refractive index
Correcting lens	4.092	9.33/7.41	1.45707(SiO ₂)
Air gap	12.146(to OS II)		1.00000
Tolerances			
Thickness (μm)	Radius (Newton's rings)	Decentering (μm)	Tilt ($m rad$)
10	3	6	0.5

refracting surfaces for the wavelength $363.8nm$ and up to 35° for $632.8nm$. A $360-700nm$ wide-band antireflection coating with an average reflectance lower than 1% could satisfy these requirements. Two kinds of antireflection coatings have been used in our lens system. The two-layer coatings as characterized in Fig. 4.9(a) are applied to the correcting lens and at one side of L_2 in system OS II. Three-layer coatings as shown in Fig. 4.9(b) are applied to the rest of the lens surfaces including the lenses of system OSI. For FGC's with a numerical aperture smaller than 0.48, the phase change introduced by these coatings approximately raises to the second power of the distance to the system axis and causes a deformation (being the deviation from the paraboloid) less than 0.125 radian (corresponding to $\frac{\lambda_h}{50}$). The phase contribution, whose profile is indicated by the dotted parabolic curve in Fig. 4.10, describes defocusing and is removable by refocusing the reconstructed beam. The phase deformation contributes spherical aberrations to the reconstructed wave. For making an FGC with a numerical aperture smaller than 0.45 (corresponding to a grating

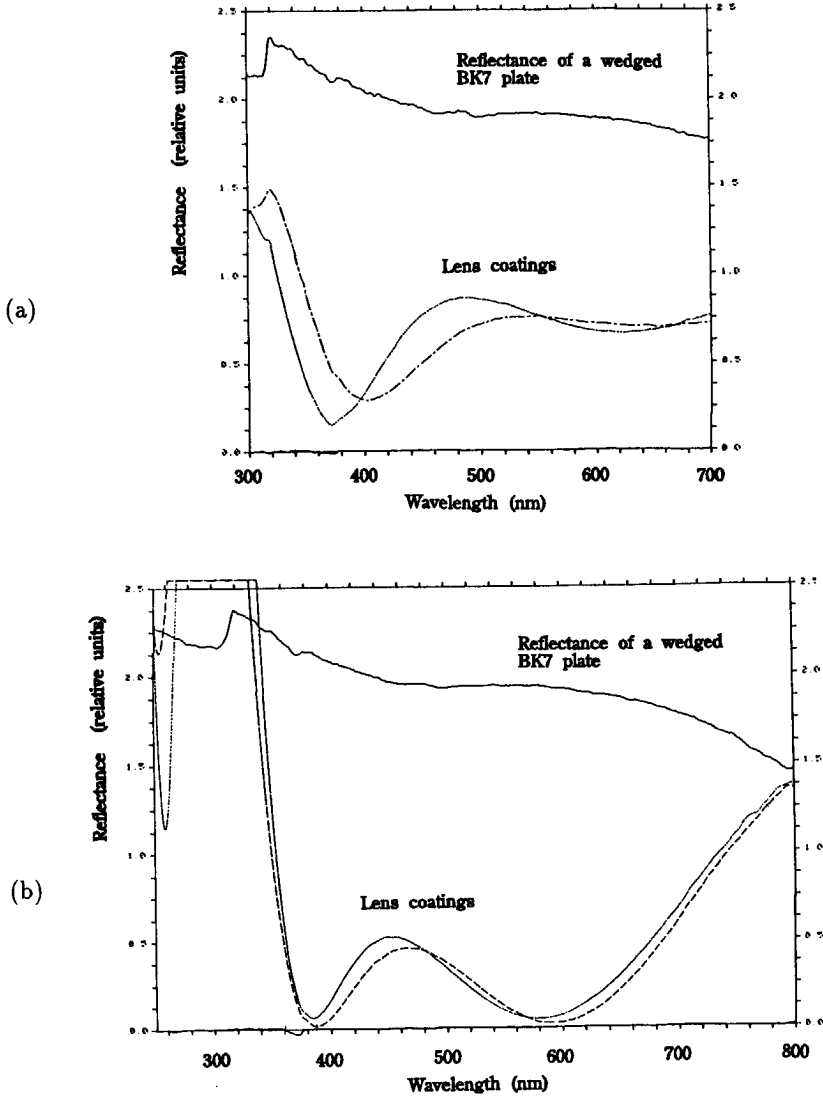


Figure 4.9: Characteristics for the antireflection coatings used in our lens system, reflectance curves as a function of the wavelength, as well as the reflectance curve of a wedged BK7 glass plate (to avoid the reflection from the back side of glass plate), measured at the angle of incidence 6° at the front surface of the plate, (a) two-layer coating (b) three-layer coating.

diameter of 2mm), the phase deformation is insignificant such that the phase change can be disregarded.

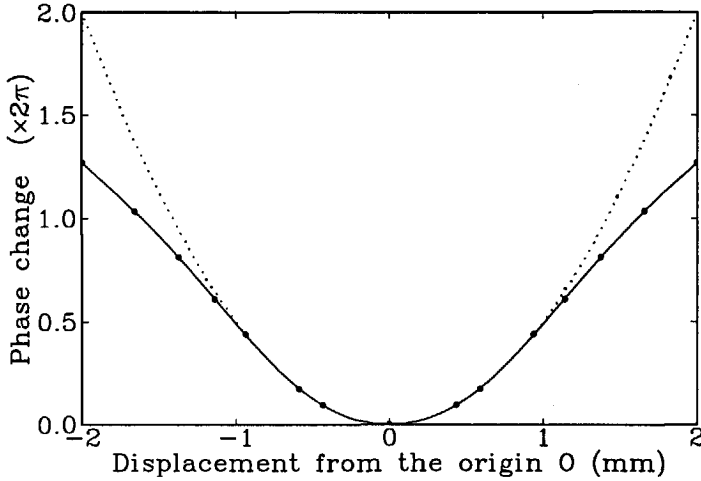


Figure 4.10: The phase change introduced by the coatings (solid line) and the best fit of the parabolic curve (dotted line).

The system OSI consists of an eyepiece and a telephoto-objective with a telephoto ratio [32] of 0.78, which are designed separately and checked by calculating the Gaussian beam propagation with the $ABCD$ law, to confirm the parallelism of the outcoming beam (0.1mrad). The eyepiece and objective have focal lengths of 50.9mm and 222.2mm , respectively. The lateral magnification of system OSI is $4.5\times$ and can be increased to $12\times$ by replacing the eyepiece. The parameters of the system OSI are given in Table 4.5. Fabrication tolerances for the system OSI are not so critical as those of the system OSII, usual fabrication tolerances for an optical system have been assumed [33].

The layout of our holographical setup is shown in Fig. 4.11. The UV-light is split by a 70/30 beam splitter (30% reflection) into two beams. The beam propagating through system OSII is spatially filtered by a $2\mu\text{m}$ pinhole behind

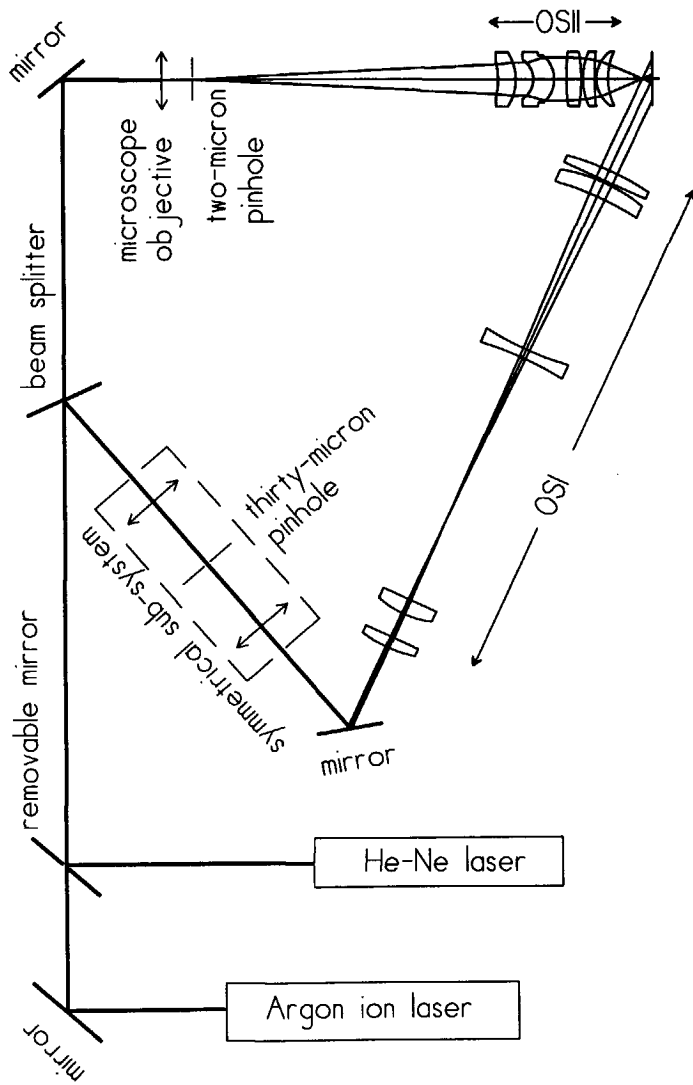


Figure 4.11: The layout of our holographic setup.

Table 4.5: The parameter values of the system OSI optimized for the Ar-ion laser.

Eyepiece			
Lens no.	Thickness(mm)	Radius(mm) of curvature	Refractive index
L_1	5.00	61.66/ ∞	1.53674(BK7)
Air gap	11.67		1.00000
L_2	7.00	42.66/ ∞	1.53674(BK7)
Air gap	120.90		1.00000
Objectives			
L_3	4.00	-151.36/134.90	1.53674(BK7)
Air gap	76.00		1.00000
L_4	7.00	-134.90/-79.43	1.53674(BK7)
Air gap	1.00		1.00000
L_5	5.00	∞ /-123.03	1.53674(BK7)
Air gap	-		1.0000

a 60 \times microscope objective. Fig. 4.12 shows a cross-section of the diffraction patterns (along the horizontal axis passing through the center of the beam) at a distance of 137.0mm behind the 2 μ m pinhole, measured by a UV-detector with a 0.5mm pinhole in front if 60 \times and 40 \times microscopes are used. The 40 \times microscope has a much stronger absorption (90% power absorption) than the 60 \times microscope (15% power absorption) such that the 60 \times microscope with the 2 μ m pinhole is still the better combination. Roughly, 15% of the incident light power can pass through the 2 μ m pinhole. 53.5% of the power behind the pinhole can enter the system OSI.

If OSI is shifted its pinhole, necessary to filter out the undesired light contributions, must be realigned. This is awkward for a pinhole inside the system

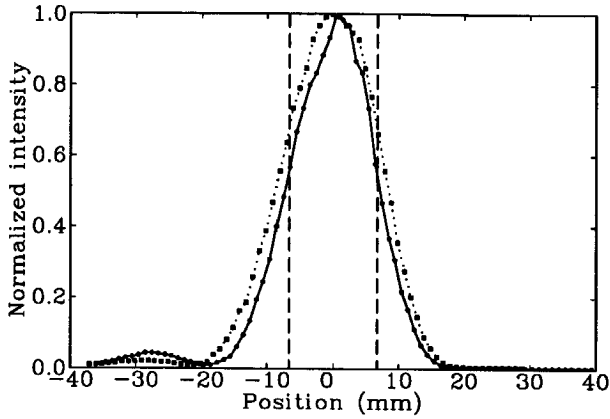


Figure 4.12: Cross-section of the diffraction patterns of a $2\mu\text{m}$ pinhole illuminated by a converging wave from a $60\times$ microscope (solid line) and a $40\times$ microscope (dotted line). The range between two vertical dashed lines shows the clear aperture of the entrance pupil.

OSI. Therefore, a symmetrical sub-system is used to filter the incident light. To minimize any possible aberration introduced by this sub-system, two identical lenses with a focal length of 50mm are placed symmetrically around the central axis, while a $30\mu\text{m}$ pinhole is inserted. Since the working distance of the system OSI is short ($\approx 19\text{mm}$), the maximum tilt angle $\theta_{\tilde{c}}$ (see Fig. 4.2) of the system OSI is limited to 30° such that the effective refractive index of the guided wave was limited to the range $1.506 < n_e < 1.739$, as calculated from Eq.(4.10).

4.4 Calculation of the intensity distribution in the recording plane

To form a high quality grating by two-beam holographic interference, the beams should have equal and uniform intensities. A method which is capable of calculating the intensity distribution in the recording plane for light passing through a system would be useful to evaluate the performance of a holographic setup. This evaluation is achieved by using a method of calculating the flux density (energy per unit area per unit time) [34], as developed by D.G. Burkhard and D.L. Shealy. The entrance pupil of an optical system is divided into small rectangles by covering it with a network of fictitious lines. The part of the field entering through each mesh is now approximated by a constant field, having the value of the actual field in the mesh center. Then, each mesh is illuminated by a known amount of energy, such that the initial value of the flux density over that mesh is known. Tracing the path of a single ray that passes through the center of each mesh through an optical system, the flux density at the intersection point of that ray with the image plane or with any other surface in the system can be calculated. From flux conservation, each element of a wavefront is related to an specific element on a refracting surface. From the value of the flux density over the element on the refracting surface, the flux density over the element of the wavefront is calculated by projection. Fig. 4.13 shows an example comprising three refracting surfaces S_1 , S_2 and S_3 . The area elements of the wavefronts $d\mathcal{W}_I(S_1)$, $d\mathcal{W}_I(S_2)$ and $d\mathcal{W}_I(S_3)$, respectively, are mapped onto the elements dS_1 , dS_2 and dS_3 of the surfaces by projection, yielding

$$d\mathcal{W}_I(S_1)=dS_1\cos(\theta_{I,1}), \quad d\mathcal{W}_I(S_2)=dS_2\cos(\theta_{I,2}), \quad d\mathcal{W}_I(S_3)=dS_3\cos(\theta_{I,3}), \quad (4.20)$$

where $\theta_{I,1}$, $\theta_{I,2}$ and $\theta_{I,3}$ are the angles of incidence that the rays make with the normals to the refracting surfaces S_1 , S_2 and S_3 , respectively. When the

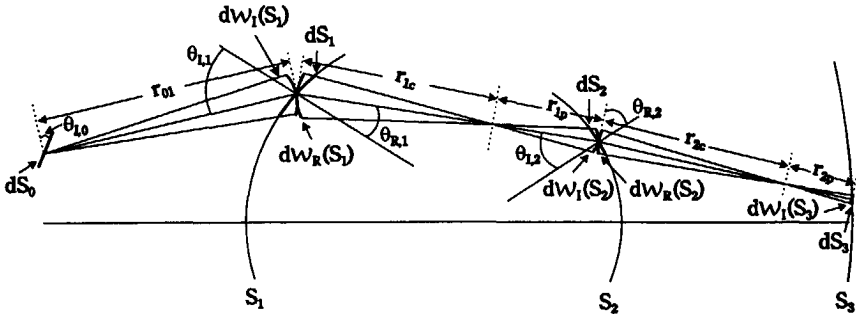


Figure 4.13: Wavefront elements at refracting surfaces S_1 , S_2 and S_3 when a wave originates from dS_0 , is refracted by dS_1 and dS_2 and imaged onto dS_3 .

wavefront leaves dS_1 or dS_2 after refraction, we have

$$dW_R(S_1) = dS_1 \cos(\theta_{R,1}), \quad dW_R(S_2) = dS_2 \cos(\theta_{R,2}), \quad (4.21)$$

where $\theta_{R,1}$ and $\theta_{R,2}$ are the angles of refraction.

If the light emanates from a source along the ray path from dS_0 to dS_3 as shown in Fig. 4.13, the flux density over dS_3 is, from Eqs.(4.20) and (4.21), written as [34]

$$\begin{aligned} \Upsilon_{dS_0-dS_3} &= \sigma_0 \rho_1 \rho_2 \cos(\theta_{I,1}) \frac{dS_1 dS_2}{dS_2 dS_3} \\ &= \sigma_0 \rho_1 \rho_2 \frac{\cos(\theta_{I,1}) \cos(\theta_{I,2}) \cos(\theta_{I,3})}{\cos(\theta_{R,1}) \cos(\theta_{R,2})} \frac{dW_R(S_1) dW_R(S_2)}{dW_I(S_2) dW_I(S_3)}, \end{aligned} \quad (4.22)$$

where ρ_1 and ρ_2 are the transmission coefficients at the surfaces S_1 and S_2 , respectively. For a point source, $\sigma_0 = \frac{I_0}{r_{01}^2}$ where I_0 is called the photometric intensity and r_{01} is the distance along the ray path between the source and the surface S_1 . For an extended source with an area element dS_0 radiating in accordance with Lambert's law, $\sigma_0 = \frac{B_0 \cos(\theta_{I,0})}{r_{01}^2}$ where B_0 is the surface brightness and $\theta_{I,0}$ is the angle between the ray and the normal to dS_0 .

The area element of each wavefront can be expressed in terms of the principal radii of curvature of the wavefront. The principal curvatures in a point of a surface are determined by the two curvatures through that point, lying in that

surface, which have the maximum and minimum curvature, respectively. The reciprocals of these curvatures are called the radii of curvatures. The normals to the curves coincide with the normal to the surface. The loci of the principal radii of curvature of the wavefront after refraction define convergence points, in general there are two focal points for each wavefront element. Fig. 4.14 shows the principal radii of the curvature r_{2c} and r'_{2c} of the wavefront as it leaves dS_2 ; r_{2p} and r'_{2p} are the corresponding principal radii of curvature when it reaches dS_3 where $r_{2p} = r_{2c} - r_{23}$ and $r'_{2p} = r'_{2c} - r_{23}$. r_{23} is the distance along the ray path between the surfaces S_2 and S_3 . Similarly, if r_{1c} and r'_{1c} are principal curvatures after the wavefront is refracted by dS_1 , the corresponding principal curvatures when it reaches dS_2 are $r_{1p} = r_{1c} - r_{12}$ and $r'_{1p} = r'_{1c} - r_{12}$. The area element on

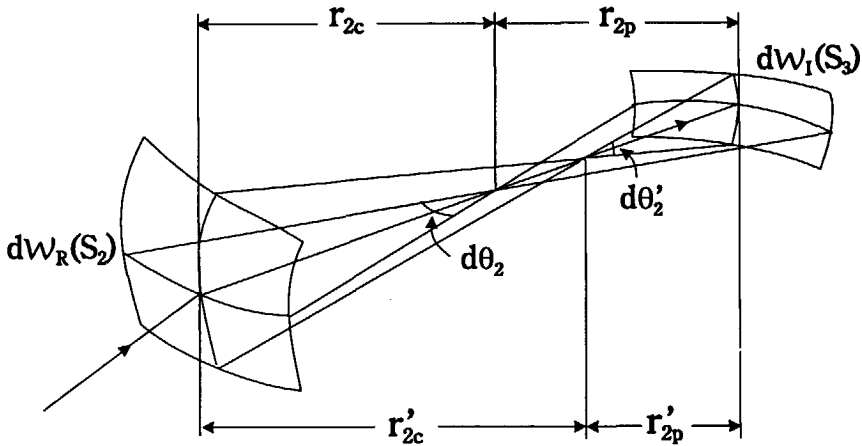


Figure 4.14: The two principal radii of curvature r_{2c} and r'_{2c} of the wavefront $dW_R(S_2)$ after refraction by the surface element dS_2 (not shown), the two principal radii of curvature r_{2p} and r'_{2p} of the wavefront $dW_1(S_3)$ diverging from the focuses, reaching the surface element dS_3 (not shown).

each wavefront can be expressed as

$$dW_R(S_2) = r_{2c}r'_{2c}d\theta_2d\theta'_2, \quad dW_1(S_3) = r_{2p}r'_{2p}d\theta_2d\theta'_2,$$

and likewise,

$$d\mathcal{W}_R(S_1) = r_{1c}r'_{1c}d\theta_1d\theta'_1, \quad d\mathcal{W}_I(S_2) = r_{1p}r'_{1p}d\theta_1d\theta'_1, \quad (4.23)$$

where $d\theta_2$ is the angle subtended at one of the focal points of the wavefront by the corresponding curve which determines one of the principal curvatures, as shown in Fig. 4.14. $d\theta'_2$ is the angle subtended at the other focal point of the wavefront by the corresponding curve. Similar definitions are applied to $d\theta_1$ and $d\theta'_1$.

Substituting Eq.(4.23) into Eq.(4.22) , we have

$$\Upsilon_{ds_0-ds_3} = \sigma_0\rho_1\rho_2 \frac{\cos(\theta_{I,1})\cos(\theta_{I,2})\cos(\theta_{I,3})}{\cos(\theta_{R,1})\cos(\theta_{R,2})} \left(\frac{r_{1c}r'_{1c}}{r_{1p}r'_{1p}} \right) \left(\frac{r_{2c}r'_{2c}}{r_{2p}r'_{2p}} \right). \quad (4.24)$$

This equation will be referred to as the flux density equation.

To use this flux density equation, the principal radii of the curvature for the incident and refracted wavefronts at each surface must be determined. Principal radii of curvature of the wavefront are, however, related to the normal curvatures which are the curvatures of the intersection curves of the wavefront with the plane of incidence, and with the plane containing the ray, perpendicular to the plane of incidence, respectively. r_{\parallel} is the radius of the normal curvature of the curve formed by the intersection of the plane of incidence with the considered surface. r_{\perp} is the radius of the normal curvature of the curve formed by the intersection of the considered surface with the plane containing the ray, perpendicular to the plane of incidence. After some calculations using differential geometry, the radii of the normal curvatures for a wavefront after refraction by a refracting surface can be obtained from [34]

$$\frac{1}{r_{\perp}(R)} = \frac{\gamma_n}{r_{\perp}(I)} + \frac{\Omega_S}{r_{\perp}(S)}, \quad (4.25)$$

$$\frac{1}{r_{\parallel}(R)} = \frac{\gamma_n}{r_{\parallel}(I)} \frac{\cos^2(\theta_I)}{\cos^2(\theta_R)} + \frac{\Omega_S}{r_{\parallel}(S)\cos^2(\theta_R)}, \quad (4.26)$$

$$\tau_R = \frac{\gamma_n \cos(\theta_I) \tau_I}{\cos(\theta_R)} + \frac{\Omega_S \tau_S}{\cos(\theta_R)}. \quad (4.27)$$

Eqs.(4.25) and (4.26) are known as the Coddington equations. For refraction, the ratio of the refractive indexes equals $\gamma_n = \frac{n(I)}{n(S)}$ and $\Omega_s = -\gamma_n \cos(\theta_I) + \cos(\theta_R)$. For reflection, $\gamma_n = 1$ and $\Omega_s = -2\cos(\theta_I)$. τ_I , τ_s and τ_R are the torsions of the incident wavefront, the refracting surface and the wavefront after refraction, respectively. $r_{\perp}(S)$, $r_{\parallel}(S)$ and τ_s are the parameters related to the refracting surface and the plane of incidence of the incoming wave. $r_{\perp}(I)$, $r_{\parallel}(I)$ and τ_I are the same parameters related to the incoming wave. Ref. [34] provides the formulas for calculating those parameters and the formulas linking the principal curvatures and the normal curvatures as well. $r_{\perp}(R)$, $r_{\parallel}(R)$ and τ_R for the refracted wave are then calculated from Eqs.(4.25), (4.26) and (4.27). For meridional rays in a rotationally symmetrical system, all terms in Eq.(4.27) can be proven to be zero. Then, the normal curvatures are identical with the principal curvatures (see [34]). In Ref. [34], for several structures the flux density has been calculated using (4.25)-(4.27). The way to eliminate the singularity that may occur in Eq.(4.24) can be also found in that reference.

Now, the flux density equation is used to calculate the intensity distribution in the recording plane for the beam passing through OS II. The loss due to reflection, absorption or scattering in the system are neglected which is acceptable for a structure consisting of materials with a good homogeneity, well-polished surfaces and high-quality antireflection coatings. The position of the recording plane is located in the front surface of the fictitious plate in the system design. Knowing that the intensity of a spherical wave originating from an axial point source is uniform, the normalized flux density of the beam in the recording plane has been calculated and is shown in Fig. 4.15 by the solid line. In Ref. [20], a system was proposed by G.N. Lawrence et al. for making FGC's with a focal length of 1.5mm by holographical recording at a wavelength of 480nm for use at a wavelength of 790nm. For comparison, this system is modified for making FGC's with a focal length of 2.0mm assuming the same wavelengths, as shown in Fig.4.16. The parameters of this system are given in Table 4.6

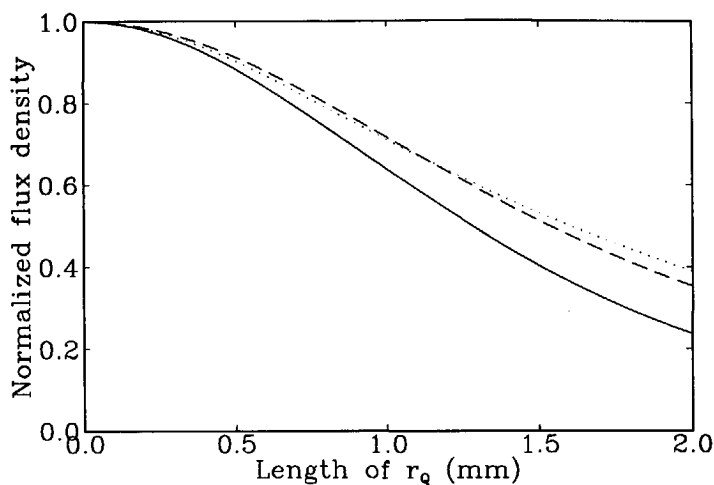


Figure 4.15: Flux density as a function of r_q in the recording plane for our system (indicated by a solid line), the modified Lawrence system (dotted line) and for back-propagation from a focal point at the back of the fictitious plate (dashed line).

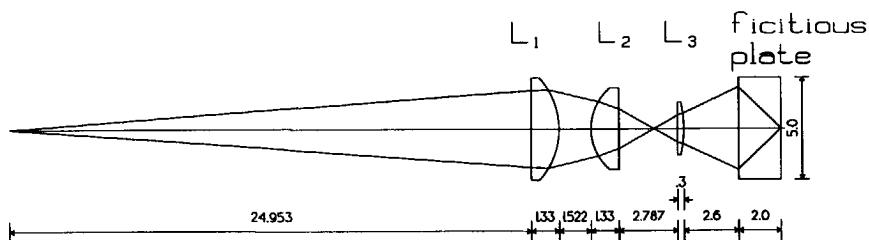


Figure 4.16: The modified Lawrence system, for recording and use at wavelengths of 480nm and 790nm , respectively, for making FGC's with a focal length of 2.0mm .

and its residual wavefront error is shown in Fig. 4.17. From that picture,

Table 4.6: The parameter values of OSII, for recording at a wavelength of $480nm$, optimized for an axial point object source at a distance $24.953mm$ in front of the system. Fabrication tolerances for this system are more critical than ours.

Lens no.	Thickness(mm)	Radius of curvature(mm)	Refractive index
L_1	1.330	$\infty/-3.834$	1.52283(BK7)
Air gap	1.522		1.00000
L_2	1.330	$2.704/\infty$	1.52283(BK7)
Air gap	9.330		1.00000
L_3	0.300	$\infty/-5.951$	1.52283(BK7)
Air gap	2.600		1.00000

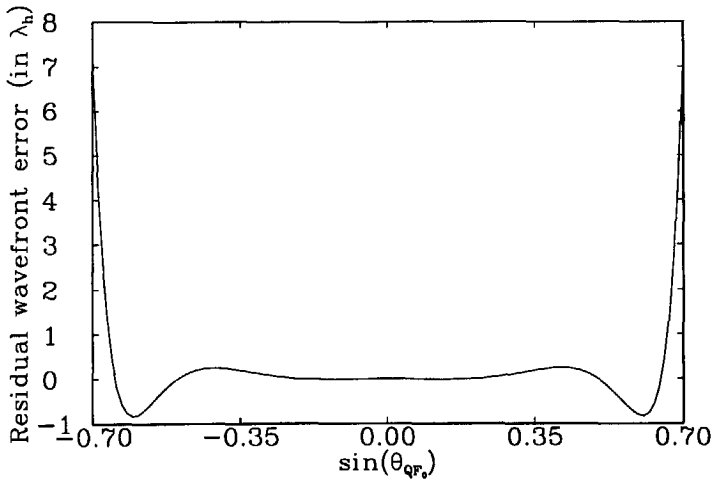


Figure 4.17: The residual wavefront error of the modified Lawrence system, calculated for recording at the wavelength of $480nm$ and used at $790nm$.

the region $-0.51 < \sin(\theta_{QF_0}) < 0.51$ shows an error is acceptable for practical use. In Fig. 4.15, the normalized flux density is also calculated for the modified Lawrence system, shown by a dotted line. During our system design, the system is optimized when the beam is converging onto a point at the back side of the fictitious plate. Considering the case that a spherical wave with uniform amplitude, originating from that focal point propagates back to the system, the normalized flux density at the front of the fictitious plate for this case is shown by the dashed line in Fig. 4.15. In fact, the flux density for this case is proportional to $\cos^3(\theta_{QF_0})$. For our system, the flux density can be approximated to be proportional to $\cos^4(\theta_{QF_0})$. Obviously, the spherical wave propagating to the focal point for our and the modified Lawrence systems is not uniform. The deviation of the dotted line from the dashed line indicates the influence of the actual inhomogeneous amplitude distribution. To obtain a uniform amplitude distribution in the recording plane (*i.e.* the front plane of the plate), neither the $\cos^3(\theta_{QF_0})$ nor the $\cos^4(\theta_{QF_0})$ suffice. No further optimization of the optical system towards this uniformity has been carried out. An absorption filter with a stronger absorption at the center but less at the edge might be introduced into the system to attain intensity uniformity. However, the distribution of the phase distortion introduced by such a filter must be determined exactly and has to be compensated for. Another disadvantage for the use of the filter is that a portion of the available power is absorbed by the filter itself. Recently, an investigation concerning conversion from a Gaussian to a uniform beam (from a collimated laser source) [35, 36, 37] has been published and might be used to solve the problem. Another solution is the use of a system in front of OS II that converts a collimated Gaussian beam into a prescribed intensity profile, such that a homogeneous amplitude is obtained at the recording plane without a spurious phase distortion. As mentioned in Ref. [35], a system with more than 95% conversion efficiency which is free from phase distortion may be achieved using two aspheric surfaces. The input aspheric surface attenuates the intense

central region of the Gaussian beam, while, at the same time, it redistributes the excess energy to the less intense peripheral region. The output aspheric surface reshapes the beam such that it becomes parallel to the input.

From calculation of the flux density behind our system OSII and referring to Eq.(4.1), the intensity distribution (proportional to the flux density) of the diverging spherical wave in the recording plane can be approximated by

$$|E_{\delta} e^{i n_a k_h (R_{\delta Q} - R_{\delta} + W_{\delta})}| = A_{\delta}^2 \frac{f^4}{(r_{\delta}^2 + f^2)^2}, \quad (4.28)$$

where A_{δ}^2 is the peak amplitude. Since the phase of the beam is already included in the exponential, we assume that E_{δ} is purely real. Then, the electric field distribution is obtained as

$$E_{\delta} e^{i n_a k_h (R_{\delta Q} - R_{\delta} + W_{\delta})} = A_{\delta} \frac{f^2}{r_{\delta}^2 + f^2} e^{i n_a k_h (R_{\delta Q} - R_{\delta} + W_{\delta})}. \quad (4.29)$$

Using the flux density equation, the beam collimated by OSI shows a Gaussian profile if a laser source with a Gaussian profile is used. For the collimated beam, the electric field distribution in the recording plane, which makes an angle θ_c with the beam, is approximated by

$$E_c e^{-i n_a k_h z \cos(\theta_c)} = A_c e^{-\frac{(y_Q^2 + [z_Q \sin(\theta_c)]^2)}{r_G^2}} e^{-i n_a k_h z \cos(\theta_c)}, \quad (4.30)$$

where A_c is the peak amplitude. r_G is the radius of the circle where the field amplitude is decreased by a factor of $\frac{1}{e}$ as compared to its value on the collimator axis. The total intensity distribution in the recording plane is written as

$$E_h E_h^* = |A_c e^{-\frac{(y_Q^2 + [z_Q \sin(\theta_c)]^2)}{r_G^2}} e^{-i n_a k_h z \cos(\theta_c)} + A_{\delta} \frac{f^2}{r_{\delta}^2 + f^2} e^{i n_a k_h (R_{\delta Q} - R_{\delta} + W_{\delta})}|^2. \quad (4.31)$$

Separately integrating the intensity over r_Q for each recording beam, using Eqs.(4.29) and (4.30), allows us to estimate the intensity ratio between these two beams such that their peak intensities are equal and a good fringe visibility around the center of the grating can be obtained. Assuming that a UV-detector with an illuminated circular detection area (4mm in diameter) is placed at the

position of the recording plane, the intensity ratio between the beams of OSI and OSII is calculated as 1.9 while taking $A_{\epsilon} = 1$, $A_{\delta} = 1$, $r_G = 5.0mm$ and $\theta_{\epsilon} = 25^{\circ}$. In practice, this intensity ratio approximates 1.4. The reason for such a deviation is that 30% of the power is blocked by the metal casing of the detector when the beam is incident upon the detector at a angle $\theta_{\epsilon} = 25^{\circ}$ (*i.e.* the actual illuminated area for the beam of OSI is smaller). Using a photodiode without a metal casing to measure the intensities, the intensity ratio approximates 1.8.

Chapter 5

EXPERIMENTAL RESULTS

5.1 The fabrication process

Waveguides with a structure shown in Fig.5.1 can be produced on glass plates. For integrated optics, glass plates are, however, seldom used because of insufficient hardness when the thickness is thin ($< 400\mu m$). Si wafers are chosen to serve as substrates in our experiments. Because of a high refractive index of Si, the waveguide structure cannot be used for visible light. In our experiments, multilayer waveguides produced on two-inch silicon substrates are used to make FGC's on the waveguides, as shown in Fig. 5.1. To form the waveguide, a thermally oxidized SiO_2 layer is first formed. The thickness of this layer is required to satisfy the condition that the field of the guided wave decays to a negligible level at the boundary between the substrate and the oxidized layer. In our experiments, the thickness of the oxidized layer is chosen as $1.7\mu m$. Due to interference between the wave diffracted by the grating into the cover and the wave reflected into the cover from the SiO_2/Si -interface, both the film thickness and the corrugation depth of the FGC have a large influence on the coupling efficiency and the attenuation coefficient. At the beginning, the film thickness was optimized for maximizing the coupling efficiency. Then, the coupling efficiency

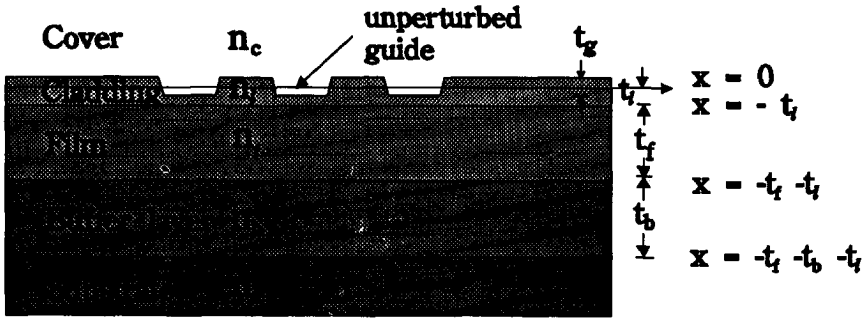


Figure 5.1: Geometry of the planar waveguide used in our experiments for making FGC's

can be optimized further by choosing the corrugation depth, until the average power of the guided wave decays to $\frac{1}{e^2}$ of input power after the wave has passed the FGC. The optimization is not effective when an FGC has a large numerical aperture, because then constructive interference may occur at the center of the FGC while destructive interference takes place at the edge, or the other way around. Thus, a small numerical aperture during optimization is recommended. If the corrugation depth t_g is equal to $40nm$ and $t_f = 20nm$ for a rectangular FGC with $N.A.=0.35$, the calculated dependencies of the effective refractive index, statistic attenuation coefficient (see page 28) and coupling efficiency upon the film thickness are shown in Fig. 5.2. There is a tendency of gradual decrease for the average of the statistic attenuation coefficient if the film thickness increases, apart from that the average is affected by the interference. The decrease in the peak values is due to the increase of mode confinement such that the field penetration into the media n_c and n_a decreases. Supposing that the waveguide of interest can support only the lowest TE_0 (TM_0) guided mode, a thickness above $350nm$ is excluded such that its optimized thickness is around $325nm$ where the coupling efficiency could be as high as 0.6, as seen from Fig. 5.2. The Al_2O_3 -layer is deposited on the oxidized Si wafer by sputtering. Due to

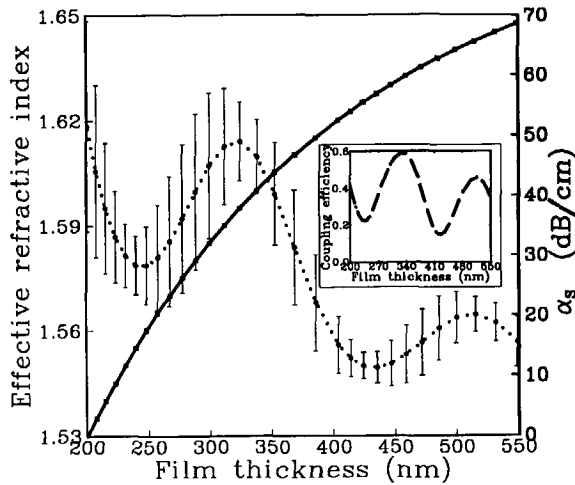


Figure 5.2: Effective refractive index (solid line), statistic attenuation coefficient (dotted line with error bars) and coupling efficiency (dashed line) for an FGC as a function of the film thickness. Refractive indexes n_c , n_l , n_f , n_b , n_s are equal to 1.0, 1.46, 1.7, 1.46, 3.83, at the wavelength of 632.8nm , respectively; $t_b = 1.7\mu\text{m}$, $t_l = 20\text{nm}$, $t_g = 40\text{nm}$.

fabrication errors and a few per cent of thickness variation over the two-inch wafer, the thickness is determined as 287nm by measurement of the effective refractive index, as will be explained in this section. Since Al_2O_3 is resistant to most chemical solutions except special treatments, 40nm SiO_2 is then produced on the top of the Al_2O_3 layer by e -beam evaporation for acting as a mask in the process of wet etching to form gratings. To measure the effective refractive index precisely by the method of prism coupling, a 510nm SiO_2 layer for controlling the incoupling efficiency is evaporated through a mask onto the top of 40nm SiO_2 layer. The parts of the two-inch wafer where gratings are produced

are protected by the mask to avoid evaporation. The wafer is then subjected to high temperature annealing at 800° for 55 minutes in a nitrogen atmosphere, to reduce the loss of the waveguide to below $1dB/cm$ [38]. Then, the wafer is ready for measurement. From the measurement of the effective refractive index [38], the thickness and refractive index of the film can be calculated approximately from the coupling angles of TE_0 and TM_0 modes through a prism with known apex and corner angles. The effective refractive index measured in this way is the value for the waveguide with a thickness of $550nm$ of the cover beneath the prism. The effective refractive index for the waveguide in which gratings are produced is evaluated from the calculated refractive index and thickness of the film. The error of this evaluation is $\pm 2\%$. The effective refractive index is calculated as 1.5778 corresponding to the tilt angle of the system OSI $24^\circ 53' 43''$. The system OSI is orientated to this tilt angle with a maximum error of $\pm 0.1^\circ$.

The positive photoresist (3.5% solids) obtained by diluting Microposit S1400-17 photoresist with Microposit thinner is dripped onto the wafer on a spin head through an injector with a $0.2\mu m$ filter inside. A thin and uniform photoresist layer is formed by spinning the wafer at $2500rpm$ for 10s and $5000rpm$ for 40s, without interruption. To minimize the standing wave effect in the photoresist, the wafer is prebaked at 60° for 10 minutes before recording. After recording, a softbaking at 90° for 25 minutes is used to remove the majority of the solvent from the photoresist. The photoresist is developed by dipping the wafer vertically into a Microposit developer 351, mixed with water at a ratio of 1 : 5 during 60 seconds. During this process, the wafer is gently shaken horizontally at a frequency of $1Hz$. After that, the wafer is immediately rinsed in water for 45 seconds with the same way of movement as at development. A postbake of 120° for 30 minutes is used to increase adhesion for a subsequent etching process. FGC's are formed by corrugating the top layer of the waveguide (SiO_2) using a chemical etchant whose recipe is $HF : NH_4F : H_2O = 1 : 5 : 80$, and which results in an approximate etching rate of $25nm/minute$ [39]. The photoresist

is removed with acetone after UV flood exposure. For an etching time of 45 seconds, a corrugation depth of about $19nm$ is reached. For a longer etching time, we found that gratings were gradually destroyed because a serious undercut occurred.

To obtain high-quality gratings, several conditions must be met. The optical path from the light source to the recording plane for the beam through OSI differs from that for OSII no more than the coherence length of the Ar^+ laser ($5cm$). This optical path difference in our setup has been adjusted to be smaller than $1cm$. The laser source must be stabilized, otherwise the fringe visibilities of gratings would be poor. Probably, gratings with weak fringe visibilities at the center and stronger ones at the periphery could be obtained. We found that it takes at least two hours to stabilize the laser at its operation power. The longer the laser operates, the better the quality of the laser light will be. In addition, the laser tube must have the correct pressure to obtain reliable results. Fringe shifts may occur due to air turbulence that makes the recording beams to vibrate, this is reduced by isolating the system with plates. Also, a short exposure time is recommended. The peak intensity ratio between two recording beams should be close to unity, is adjustable by tilting the $2\mu m$ pinhole forward or backward along the axis of OSII. The output power of the laser is set to $150mW$. To make the peak intensities about equal, the irradiances (total power arriving at unit area) of the beams of OSI and OSII in the recording plane, measured by an UV detector of the power meter (a product of OAI optical associates Inc., type 206), are adjusted to 5.0 and $3.6mW/cm^2$, respectively (corresponding to an intensity ration of 1.39, more explanations at page 70). Different exposure times have been tried out, grating sizes in the diameters of $1.0mm(0.42s)$, $1.3mm(0.44s)$, $1.5mm(0.46s)$, $1.7mm(0.48s)$, $1.8mm(0.5s)$ and $2.0mm(0.52s)$ have been obtained. As will be seen in Sec. 5.3, the optimized exposure time, determined from the quality of image is about 0.44 second. If those conditions are met, we found that the gratings are reproducible.

5.2 The measurement setup

Measuring the intensity distribution is the main objective to judge the performance of our FGC's and to compare the theoretical and experimental results. In our measurement setup, prism coupling is used to direct collimated light into a waveguide by adjusting the angle between the light and the prism. Besides, the holder in which the wafer is placed must be rotatable such that an optimized condition for the guided wave incident upon an FGC can be obtained. This can be determined by checking the image of the focal spot with a microscope. Therefore, the setup for measuring the intensity distribution must have at least two freedoms of rotation. Fig. 5.3 shows the measurement setup. The beam

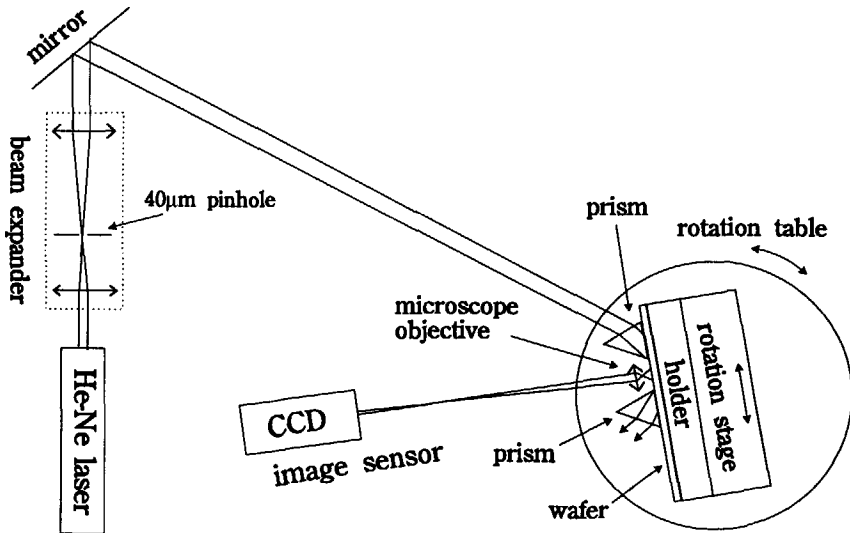


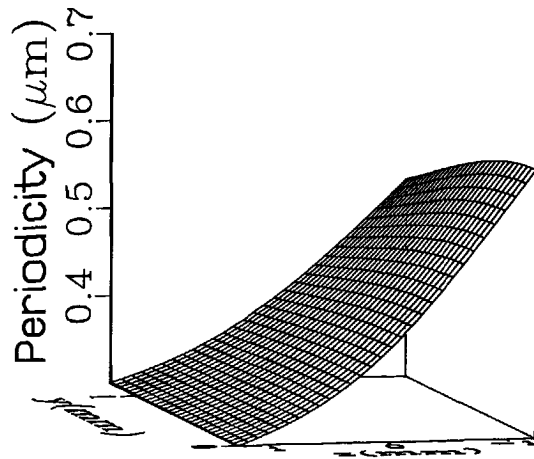
Figure 5.3: The setup for measuring the intensity distribution of an FGC.

size of a He-Ne laser has been enlarged to $6mm$ by a beam expander consisting of two lenses with focal lengths of $50mm$ and $150mm$. The parallelism measured from the interference of the reflected beams from both sides of a parallel plate is $0.1mrad$. The wafer is placed vertically. The apparatus comprising

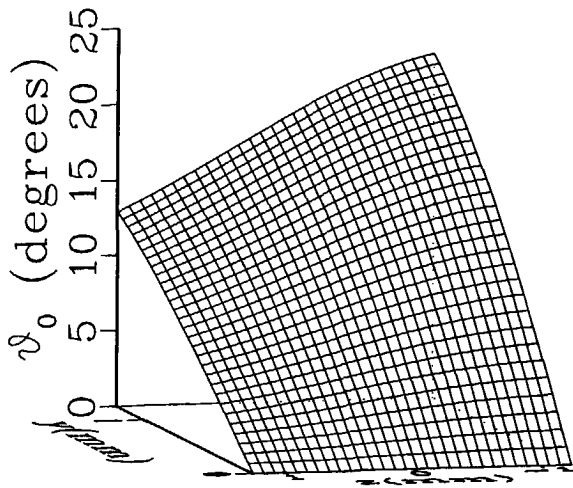
and a wafer holder for incoupling and outcoupling are mounted to a rotation table (horizontal rotation). The prism for outcoupling is removable to give enough space for microscopic inspection. The wafer holder is rotated vertically to obtain a good image of the focal spot by microscope observation. The eyepiece of the microscope is removed. A CCD image sensor (Philips NXA1011/01) is placed behind the microscope objective at a distance of 17cm , the focal spot is projected onto the CCD image sensor and observed through a computer monitor with an image capture board. The microscope objective is re-adjusted to obtain a good image displayed on the monitor.

5.3 Focusing characteristics

Some investigations on FGC characteristics concerning its grating pattern and field distribution around the focus have been carried out and their experimental results are included in this section. In our theoretical calculation, an FGC is divided into subgratings. Locally, each of them is replaced by a periodic and straight grating. ϑ_0 (being a parameter used in the analysis of the grating coupler, see Appendix A) is defined as the angle between the axis of the incident guided wave and the normal of the grating lines. Assuming that the incident wave propagates along the positive z -axis, ϑ_0 is exactly the angle between the normal of the grating lines and the z -axis. The periodicity and the angle ϑ_0 as a function of position across the FGC with a theoretical grating pattern whose parameters ($n_e = 1.5778$, $f_0 = 2\text{mm}$) are chosen the same as the produced FGC's described in Sec.5.1, are calculated from the calculated grating pattern equation (see page 10) and shown in Fig. 5.4. For a better visual effect, the z -axis has been reversed. At the z -axis, the periodicity varies from $0.6\mu\text{m}$ to $0.3\mu\text{m}$ along the propagation direction of the guided wave for a FGC with $N.A. = 0.53$. The coupling between TE- and TM-waves becomes more and more significant when the angle ϑ_0 increases.



(a)



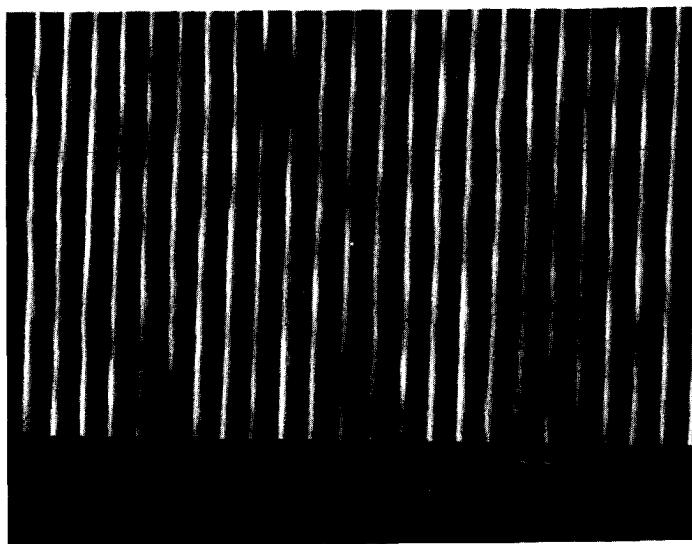
(b)

Figure 5.4: (a) The periodicity and (b) the angle ϑ_0 as a function of position across an FGC, calculated from the parameters $n_e = 1.5778$, $f_0 = 2mm$.

Our gratings in photoresist have been examined by a scanning electron microscope (SEM). Fig. 5.5 shows SEM photographs of the grating lines with a periodicity of $0.50\mu\text{m}$ and $0.31\mu\text{m}$ at two different regions near the z -axis. As can be seen from the pictures, the chirp rate and the curvature of the grating lines within a region of $8 \times 10\mu\text{m}^2$ are negligible such that locally replacing such a grating by a periodic and straight grating is an acceptable approximation.

Using the measurement setup as described in the previous section, the wafer was rotated to minimize the focal spot of the diffracted wave when a collimated guided TE-mode was incident upon an FGC. The focal spot was projected through a $70\times$ microscope objective (corrected without a 0.17mm thick cover glass) onto a CCD image sensor and was observed through a computer monitor with an image capture board. The microscope objective was adjusted to minimize the spot size. The two-dimensional and three-dimensional diffraction intensity patterns captured by the CCD image sensor for all FGC's mentioned in Sec. 5.1 are shown in Fig. 5.6 and Fig. 5.7, respectively. For an exposure time shorter than 0.44s , the diffracted wave shows a main peak with significant side lobes in the y -direction but negligible ones in the z -direction. The main peak shows a little astigmatism. The theory given in this dissertation, however, cannot explain why those side lobes with strong power occur. Probably, this results from misalignment of the recording setup such that some aberrations are recorded in the interference patterns. The image quality becomes worse if the exposure time increases longer than 0.44s . We observed that only a part of the diffracted wave can be focused into a spot, with considerably strong peaks beside. In addition, we also found that a few light rings diverge from the periphery of the FGC. This can be seen from the back side of a white paper placed above the FGC. In fact, these rings originate from recordings of the the light from system OSII that is reflected at the interfaces of the waveguide back into the photoresist. The reflected light of OSI back into the photoresist also destroys the interference pattern, because a very strong reflection occurs at each inter-

(a)



(b)

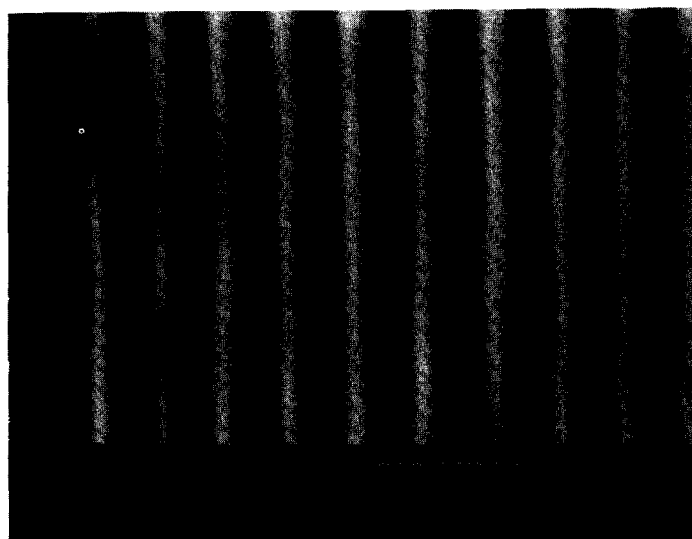


Figure 5.5: (a) FGC's with a periodicity of $0.50\mu m$, (b) a periodicity of $0.31\mu m$.

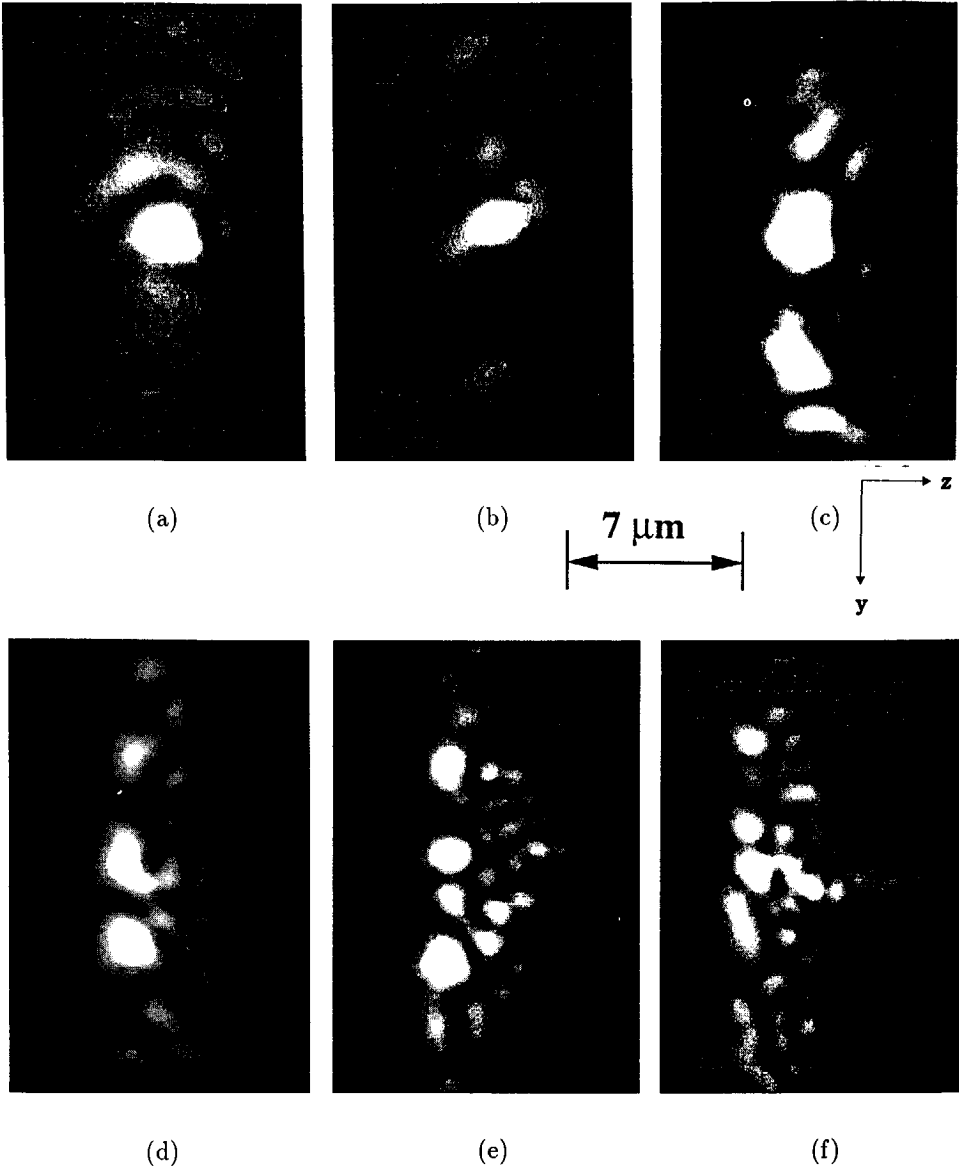
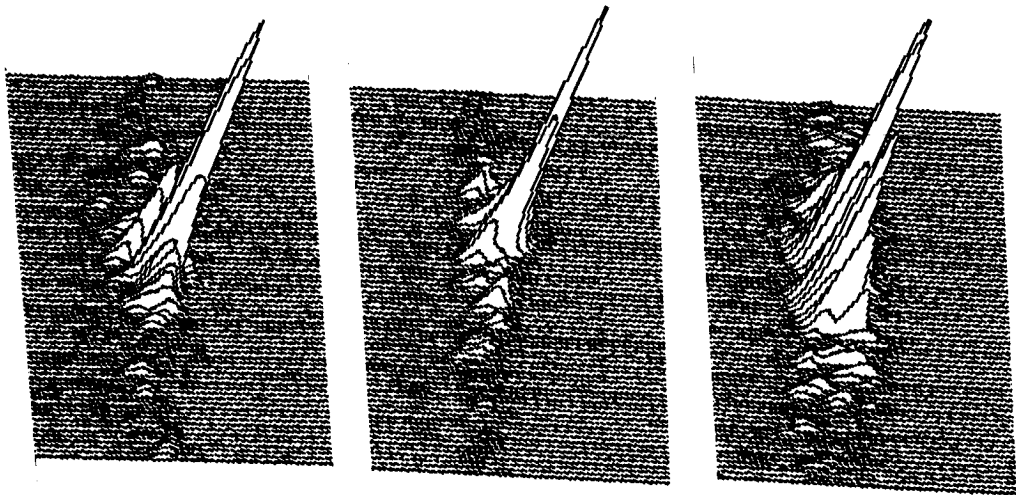


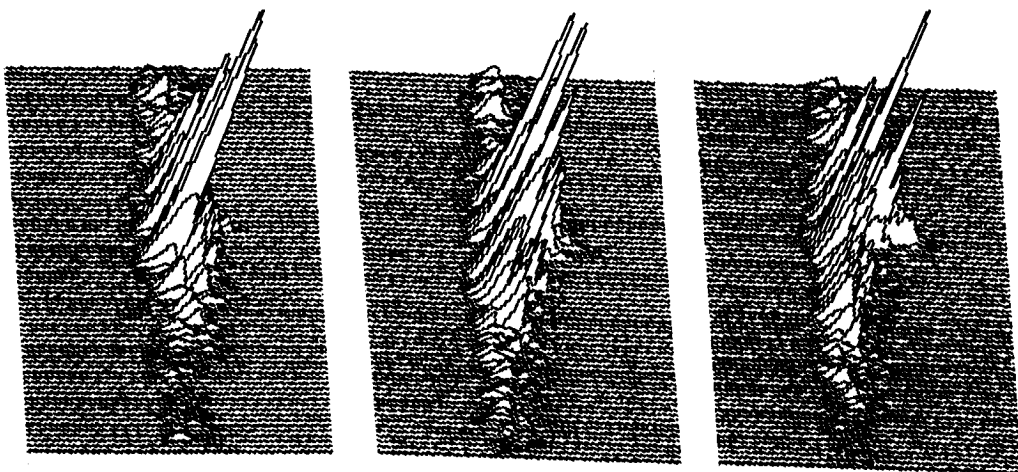
Figure 5.6: (a) Two-dimensional intensity patterns of focal spots for FGC's recorded during (a) $0.42s$, (b) $0.44s$, (c) $0.46s$, (d) $0.48s$, (e) $0.50s$, (f) $0.52s$.



(a)

(b)

(c)



(d)

(e)

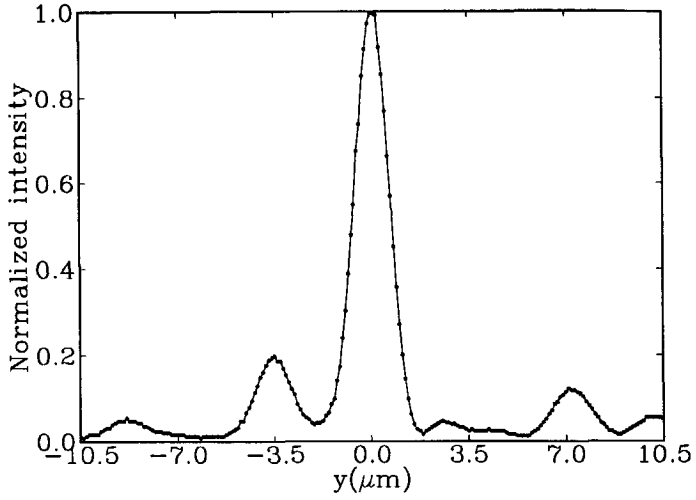
(f)

Figure 5.7: (a) Three-dimensional intensity patterns of focal spots for FGC's recorded during (a) 0.42s, (b) 0.44s, (c) 0.46s, (d) 0.48s, (e) 0.50s, (f) 0.52s.

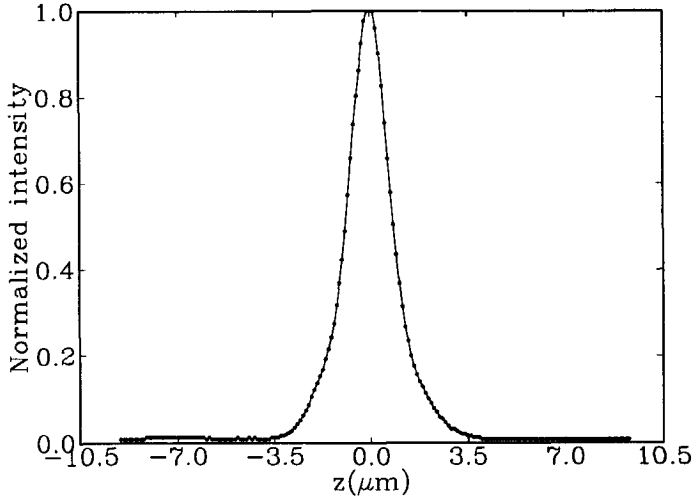
face when light from OSI is incident upon the wafer at an angle of incidence $\approx 65^\circ$. For a long exposure time, multiple reflections between the photoresist occur such that the recording process is no longer a two-beam interference. Such a recording process results in concentric ghost images between the closely spaced grating lines as described in Ref. [40]. In that paper, a trilayer resist system was used to obtain precise pattern dimension control by adjusting the refractive indices and attenuation coefficients of the resist layers. The linewidth variation caused by the interference effect was reduced to $0.04\mu\text{m}$ [40].

As seen from in Figs. 5.6 and 5.7, the optimized exposure time is about 0.44s . The intensity profiles, containing the peak intensity, in the y - and z -directions with an exposure time of 0.44s is shown in Fig. 5.8. The spot widths in the y - and z -directions, being the region in which the intensity drops to $\frac{1}{e^2}$ of the peak intensity, are measured as $2.3\mu\text{m}$ and $3.5\mu\text{m}$, respectively. The average focal spot diameter is $2.9\mu\text{m}$ (see page 21). 55.4% and 17.4% of the power carried by the diffracted wave, distributed over that spot and its side lobes. During the measurement of spot size, the eyepiece of the microscope has been replaced by one with a micrometer and a reticle inside. The magnification power of the microscope objective and the scale of the micrometer have been calibrated by a standard micrometer ruler. A measurement accuracy down to $0.1\mu\text{m}$ could be achieved.

The coupling efficiency (for its definition see page 21) for each FGC has been measured. However, due to instability of the out-coupling prism, the attenuation of the guided wave outside the grating and the loss occurring at the surface of prism where the outgoing light was measured by a photodetector, a $\pm 20\%$ error of this evaluation must be assumed. A slit placed in front of the measurement setup was adjusted such that the width of the collimated guided wave equaled that of the measured FGC. The powers of the diffracted wave and of the light coupled out by a prism were measured by a photodetector. Assuming that the sum of the measured powers equals the incident power, the coupling efficiency



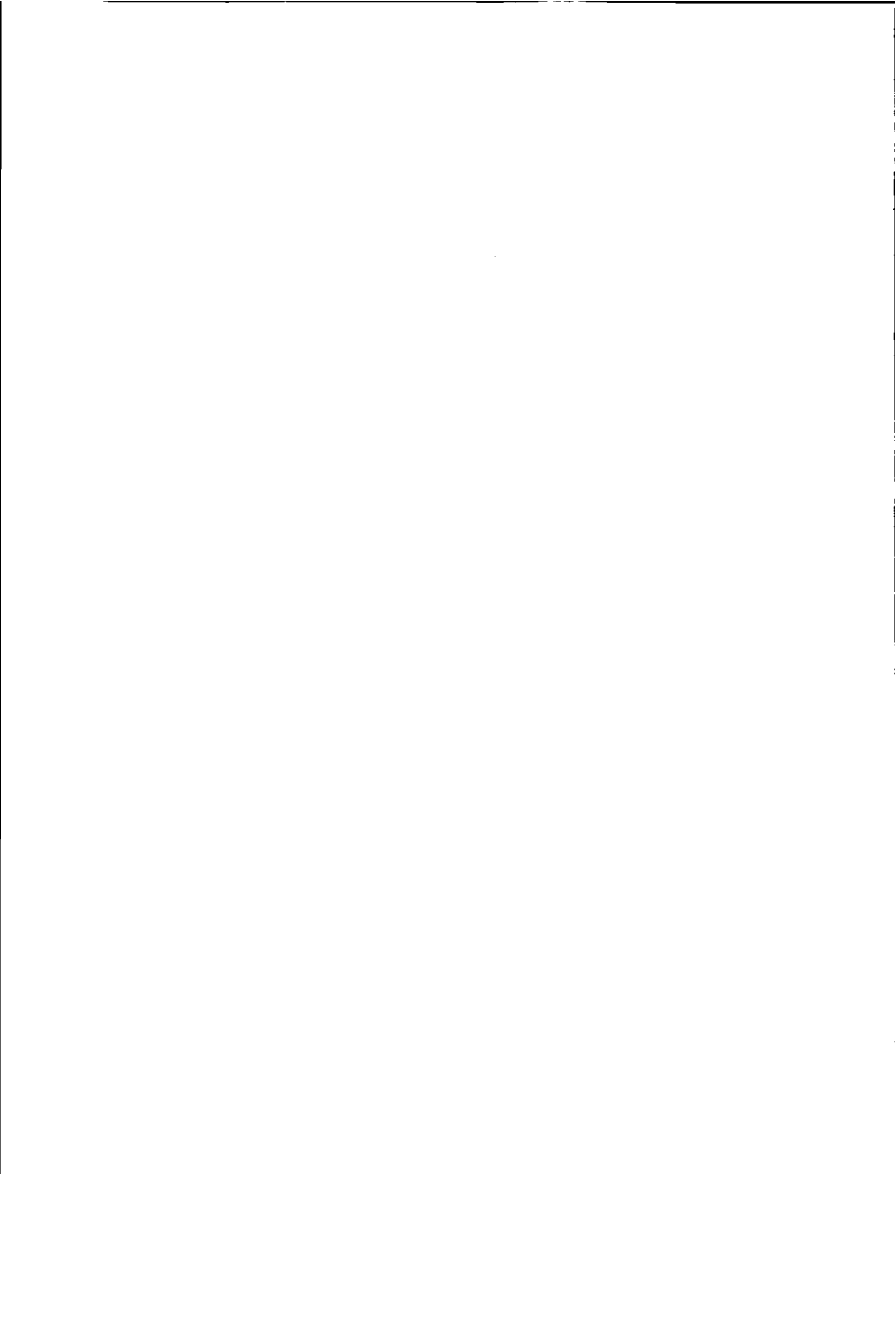
(a)



(b)

Figure 5.8: Intensity profile containing the peak intensity in (a) the y -direction, (b) the z -direction.

can be evaluated. The coupling efficiencies for the FGC's have been calculated as 0.13(0.42s), 0.15(0.44s), 0.32(0.46s), 0.35(0.48s), 0.40(0.5s) and 0.45(0.52s).



Chapter 6

DISCUSSION AND CONCLUSIONS

The field distributions of a focusing grating coupler in the exit plane and around the diffraction focus can be calculated for a diverging incident wave. The actual complex propagation constant of the incident guided wave is taken into consideration, leading to the optimization of the corrugation depth. In order to achieve a high coupling efficiency, at the same time preventing the focal spot from broadening, we suggest that the corrugation depth is determined such that the average power of the guided wave decays to $\frac{1}{e^2}$ of input power after the wave passing the FGC.

For FGC's, coma and astigmatism are essential and considerable. Using the criterion $\text{RMSD} \leq \frac{\lambda'}{14}$ to estimate the FGC's tolerances is inappropriate, because the criterion was obtained under the assumption that the field amplitudes are uniform across the exit plane. The Strehl intensity is chosen to judge the focal spot quality. An FGC system is considered to be well-corrected if $i(F') \geq 0.8$.

The coupling efficiencies for the FGC's discussed in Chapters 2 and 3 are low (about 0.35), and the energy reaching the focal spot is even lower (see

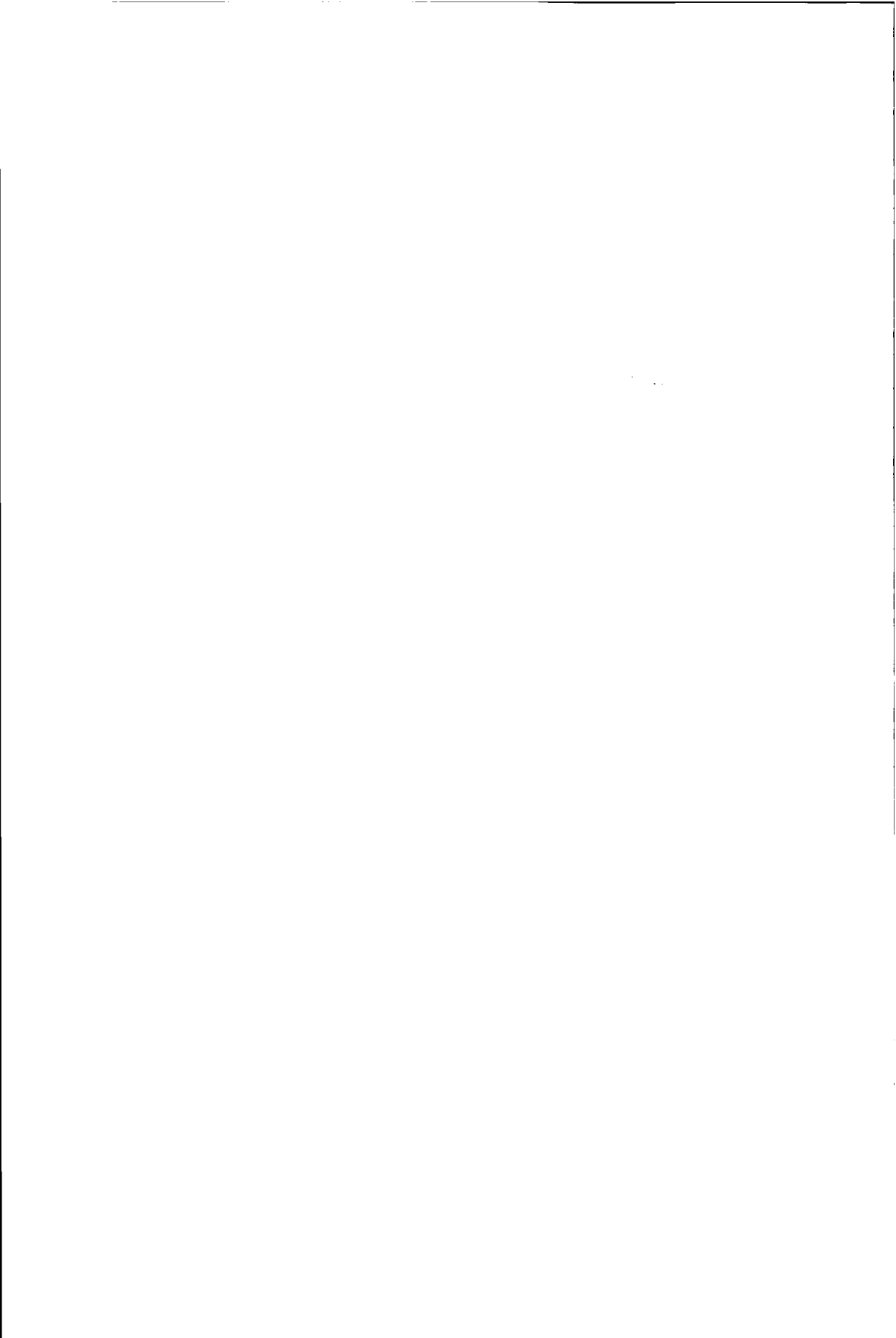
Sec. 3.4). For an FGC produced on a multilayer waveguide, the coupling efficiency can be increased by reflecting part of the light radiated into the substrate back toward the cover like Ura et al.[6] did in their demonstration device for an integrated-optical pickup head. We found, however, that the wavefront distribution becomes complicated due to reflections at interfaces between the various layers. This causes the focal spot to broaden. For an FGC produced on a multilayer waveguide, formulas for calculating the complex amplitude vectors of the Floquet waves and the change $\delta\beta$ in the propagation constant can be derived by applying at each interface the *equivalent boundary conditions* discussed in Ref. [10].

A method [34] which is capable of calculating the intensity distribution in the recording plane is used to evaluate the performance of our holographic setup. Because of the inhomogeneous intensity distribution in the recording plate and the residual wavefront error of the holographic setup, a diameter of $2mm$ is about the maximum grating size that can be produced in this recording setup.

In our experiments, multilayer waveguides produced on two-inch silicon substrates are used to make FGC's. For such a waveguide, the coupling efficiency can be increased by reflecting part of the light radiated into substrate back to cover in which the focus is formed. Theoretically, the coupling efficiency could be as high as 0.6 by optimizing the waveguide parameters and the corrugation depth. However, the required corrugation depth of $40nm$ for gratings with a periodicity around $0.3\mu m$ is too deep for wet chemical etching because of a serious undercut occurred. Dry etching techniques may be used to solve this problem.

The spot widths in the y - and z -directions for an FGC, at $\frac{1}{e^2}$ of the peak intensity, have been measured as $2.3\mu m$ and $3.5\mu m$, respectively. The average focal spot diameter is $2.9\mu m$. The FGC shows a little astigmatism causing such a difference in the spot widths. The coupling efficiency of this FGC is about 0.15. 55.4% and 17.4% of the power carried by the diffracted wave into that spot and its side lobes. For an FGC with a larger coupling efficiency, the image

quality is worse due to multiple reflections inside the photoresist. To reduce interference effects, a trilayer resist system [40] can be used for future work to obtain precise pattern dimension control by adjusting the refractive indices and attenuation coefficients of the resist layers.



Appendix A

FORMULAS FOR CALCULATING THE AMPLITUDE FACTORS OF THE FLOQUET WAVES AND THE QUANTITY $\delta\beta$

Consider an incident parallel beam propagating through a grating coupler (produced on a waveguide with the structure shown in Fig. 5.1) in the direction $(\vec{u}\sin(\vartheta_0) + \vec{v}\cos(\vartheta_0))$, which is inclined over an angle ϑ_0 to the grating vector $\vec{G} = \frac{2\pi}{\Lambda}\vec{v}$. Here, Λ is the periodicity of the grating, \vec{u} and \vec{v} are the unit vectors in the coordinate system (x, u, v) parallel to and perpendicular to the grating lines, positioned in the exit plane. The incident guided wave having its field characterized by the dependence of $e^{i\beta(u\sin(\vartheta_0)+v\cos(\vartheta_0))}$ can couple to Floquet waves characterized by the dependence $e^{i\beta(u\sin(\vartheta_0)+v\cos(\vartheta_0))+m\vec{G}\cdot\vec{v}}$ (where $m = 0, \pm 1, \pm 2, \dots$). The electric and magnetic fields vectors \vec{E} and \vec{H} are expressed in the coordinates (x, u, v) by

$$\begin{aligned}\vec{E}(x, u, v) &= \vec{E}_{un}(x, u, v) + \vec{E}_m(x, u, v) + \vec{E}_0(x, u, v), \\ \vec{H}(x, u, v) &= \vec{H}_{un}(x, u, v) + \vec{H}_m(x, u, v) + \vec{H}_0(x, u, v),\end{aligned}\tag{A.1}$$

where \vec{E}_{un} and \vec{H}_{un} are the fields in the unperturbed planar waveguide with its cover/cladding boundary at the plane $x = 0$. \vec{E}_m and \vec{H}_m are the sum fields for all $m \neq 0$ Floquet waves. \vec{E}_0 and \vec{H}_0 are the field for the $m = 0$ Floquet wave. \vec{E}_m and \vec{H}_m are proportional to the corrugation depth t_g , \vec{E}_0 and \vec{H}_0 are proportional to t_g^2 [10]. The perturbation fields (the sums of \vec{E}_m , \vec{H}_m and \vec{E}_0 , \vec{H}_0) are assumed to be small as compared to the unperturbed fields \vec{E}_{un}

and \vec{H}_{un} . From Maxwell's equations, the field components \vec{E}_{px} and \vec{H}_{px} (where $p=un, m, 0$) satisfy independently the wave equation

$$\left(\frac{\partial^2}{\partial x^2} + \frac{\partial^2}{\partial u^2} + \frac{\partial^2}{\partial v^2} + n(x)^2 k_0^2 \right) \begin{Bmatrix} E_{px} \\ H_{px} \end{Bmatrix} = 0 \quad (p = un, m, 0). \quad (\text{A.2})$$

The refractive index profile can be written as an equation similar to Eq.(2.1) for the unperturbed planar guide shown in Fig.5.1. Eq.(A.2) indicates that there are two independent groups of modes, viz., TE-modes (for which $E_{px}=0$) and TM-modes (for which $H_{px}=0$). The two other field components can be calculated by substituting the x -components into the formulas given in Ref. [10]. Let us assume that a guided TE-wave is obliquely incident upon the grating coupler. The incident guided wave can couple to Floquet waves of the TE-polarization as well as with Floquet TM-waves. Since Floquet waves are characterized by the dependence $e^{i\beta(u \sin(\vartheta_0) + v \cos(\vartheta_0)) + m\vec{G}\cdot\vec{v}}$, Eq.(A.2) becomes

$$\begin{Bmatrix} \frac{\partial^2}{\partial x^2} + [n(x)^2 k_0^2 - \beta_m^2] \\ H_{px}(\beta_m) \end{Bmatrix} \begin{Bmatrix} E_{px}(\beta_m) \\ H_{px}(\beta_m) \end{Bmatrix} = 0 \quad \begin{array}{l} (p = un, m, 0), \\ (m = 0, \pm 1, \pm 2, \dots), \end{array} \quad (\text{A.3})$$

in which

$$\beta_m = \sqrt{[\beta_0 \sin(\vartheta_0)]^2 + [\beta_0 \cos(\vartheta_0) + m\vec{G}\cdot\vec{v}]^2}, \quad (\text{A.4})$$

is the propagation constant of the m -th Floquet wave. The direction of $\vec{\beta}_m$ is given by its angle ϑ_m with respect to the local grating vector \vec{G} , satisfying

$$\begin{aligned} \beta_m \sin(\vartheta_m) &= \beta_0 \sin(\vartheta_0), \\ \beta_m \cos(\vartheta_m) &= \beta_0 \cos(\vartheta_0) + m\vec{G}\cdot\vec{v} \quad (m = 0, \pm 1, \pm 2, \dots). \end{aligned} \quad (\text{A.5})$$

Eq.(A.3) has the solutions $E_{px}(\beta_m)$ and $H_{px}(\beta_m)$ of the character of plane waves:

$$\begin{aligned} E_{px}(\beta_m) &\propto e^{ik_j m x} e^{i\beta_m [u \sin(\vartheta_m) + v \cos(\vartheta_m)]}, \\ H_{px}(\beta_m) &\propto e^{ik_j m x} e^{i\beta_m [u \sin(\vartheta_m) + v \cos(\vartheta_m)]}, \end{aligned} \quad (\text{A.6})$$

where

$$k_{\tilde{j}m} = \sqrt{n_{\tilde{j}}^2 k_0^2 - \beta_m^2} \quad (\tilde{j} = c, l, f, b, s), \quad (m = 0, \pm 1, \pm 2, \dots), \quad (\text{A.7})$$

where the subscript $\tilde{j} = c, l, f, b, s$ denotes the field in the regions of cover, cladding, film, buffer layer, substrate (see Fig. 5.1). To satisfy the boundary conditions for the unperturbed guide, the field component H_{px} of the incident guided TE-wave can be written in the form

$$\begin{aligned} H_{unx}(x, u, v) &= A_{c0}^{h+} e^{ik_{c0}x} e^{i\beta_0[u \sin(\vartheta_0) + v \cos(\vartheta_0)]} \quad (x > 0), \\ &= [A_{l0}^{h-} e^{-ik_{l0}(x+t_l)} + A_{l0}^{h+} e^{ik_{l0}(x+t_l)}] e^{i\beta_0[u \sin(\vartheta_0) + v \cos(\vartheta_0)]} \quad (-t_l < x < 0), \\ &= [A_{f0}^{h-} e^{-ik_{f0}(x+t_l+t_f)} + A_{f0}^{h+} e^{ik_{f0}(x+t_l+t_f)}] e^{i\beta_0[u \sin(\vartheta_0) + v \cos(\vartheta_0)]} \quad (-t_l - t_f < x < -t_l), \\ &= [A_{b0}^{h-} e^{-ik_{b0}(x+t_l+t_f+t_b)} + A_{b0}^{h+} e^{ik_{b0}(x+t_l+t_f+t_b)}] e^{i\beta_0[u \sin(\vartheta_0) + v \cos(\vartheta_0)]} \\ &\quad (-t_l - t_f - t_b < x < -t_l - t_f), \\ &= A_{s0}^{h-} e^{-ik_{s0}(x+t_l+t_f+t_b)} e^{i\beta_0[u \sin(\vartheta_0) + v \cos(\vartheta_0)]} \quad (x < -t_l - t_f - t_b). \end{aligned} \quad (\text{A.8})$$

Here, waves with a phase factor $e^{ik_{j0}x}$ or $e^{-ik_{j0}x}$ travel in the positive (also indicated by '+' in the superscript of the field amplitudes) or negative x -direction ('-'), respectively. A_{c0}^{h+} is the magnetic field amplitude of the incident TE wave at a point Q in the plane $x = 0$. The superscript h in A_{c0}^{h+} indicates that the incident wave is a TE-mode.

The dispersion equation is obtained by imposing the boundary conditions at each interface to the field H_{px} . We obtain [10]

$$\frac{1 - R_{0h}^{fl} R_{0h}^{fb} e^{2ik_{f0}t_f}}{R_{0h}^{fb} e^{2ik_{f0}t_f} - R_{0h}^{fl}} = R_{0h}^{lc} e^{2ik_{l0}t_l}, \quad (\text{A.9})$$

where

$$R_{0h}^{fb} = \frac{k_{f0} - k_{b0}}{k_{f0} + k_{b0}}, \quad R_{0h}^{fl} = \frac{k_{f0} - k_{l0}}{k_{f0} + k_{l0}}, \quad R_{0h}^{lc} = \frac{k_{l0} - k_{c0}}{k_{l0} + k_{c0}}. \quad (\text{A.10})$$

In the derivation of Eq.(A.10), satisfying the requirement $|k_{b0}| t_b \gg 1$ (k_{b0} is purely imaginary) has been assumed, such that the factor $e^{2ik_{b0}t_b}$ is approximated by zero. This requirement implies that the field of the guided wave must decay

to a negligible level at the boundary between the substrate and the buffer layer. In Ref. [10], two groups of equivalent boundary conditions are provided. One of them is used to calculate the field amplitudes of the $m \neq 0$ Floquet waves E_m and H_m . The other is used to calculate field amplitudes of the $m = 0$ Floquet waves E_0 and H_0 as well as the quantity $\delta\beta$ (its definition see page 11). After using the equivalent boundary conditions, the field amplitudes of the diffracted Floquet waves ($m \neq 0$) can be written in terms of A_{c0}^{h+} . For diffracted waves with a TE-polarization, the field amplitudes of Floquet waves ($m \neq 0$) equal, at the cover/cladding interface:

$$A_{cm}^{h+} = i\tilde{\eta}_m \frac{Z_0}{n_c} \frac{\beta_m}{\beta_0} (k_{lm} - k_{cm}) \cos(\vartheta_0 - \vartheta_m) \frac{1 - R_{mh}^{fl} \rho_h - (R_{mh}^{fl} - \rho_h) e^{2ik_{lm}t_i}}{1 - R_{mh}^{fl} \rho_h + R_{mh}^{lc} (R_{mh}^{fl} - \rho_h) e^{2ik_{lm}t_i}} A_{c0}^{h+}; \quad (\text{A.11})$$

at the interface between the buffer layer and the substrate:

$$A_{sm}^{h-} = \frac{(1 + R_{mh}^{bs})(1 + R_{mh}^{fb})(1 - R_{mh}^{fl}) e^{i(k_{bm}t_b + k_{jm}t_j + k_{lm}t_i)}}{(1 + R_{mh}^{fb} R_{mh}^{bs} e^{2ik_{bm}t_b})(1 - R_{mh}^{fl} \rho_h - (R_{mh}^{fl} - \rho_h) e^{2ik_{lm}t_i})} A_{cm}^{h+}, \quad (\text{A.12})$$

where Z_0 is the wave impedance of vacuum. Waves with a TE-polarization are indicated by h in the superscript of the amplitude coefficients, and e for waves with a TM polarization. ρ_h appearing in Eqs.(A.11) and (A.12) equals

$$\rho_h = \frac{R_{mh}^{fb} + R_{mh}^{bs} e^{2ik_{bm}t_b}}{1 + R_{mh}^{fb} R_{mh}^{bs} e^{2ik_{bm}t_b}} e^{2ik_{jm}t_j}. \quad (\text{A.13})$$

where

$$R_{mh}^{fb} = \frac{k_{jm} - k_{bm}}{k_{jm} + k_{bm}}, \quad R_{mh}^{bs} = \frac{k_{bm} - k_{sm}}{k_{bm} + k_{sm}}, \quad R_{mh}^{fl} = \frac{k_{jm} - k_{lm}}{k_{jm} + k_{lm}}, \quad R_{mh}^{lc} = \frac{k_{lm} - k_{cm}}{k_{lm} + k_{cm}}. \quad (\text{A.14})$$

In Eq.(A.11), $\tilde{\eta}_m$ is the m -th Fourier coefficient of the groove profile multiplied by the half-depth of the corrugation ($\frac{t_g}{2}$), and is calculated from the groove profile described by

$$\begin{aligned} x &= \frac{t_g}{2} \chi(v) \quad [\chi(z) \leq 1], \\ &= \sum_{m=1}^{\infty} \left(\tilde{\eta}_m e^{-i\frac{2\pi}{\lambda} z} + \tilde{\eta}_m^* e^{i\frac{2\pi}{\lambda} z} \right), \end{aligned} \quad (\text{A.15})$$

where $\chi(v)$ gives the dependence of the surface corrugation as a function of the v -coordinate.

Similarly, the field amplitudes of Floquet waves ($m \neq 0$) with a TM-polarization equal, at the cover/cladding interface:

$$A_{cm}^{e+} = -i\tilde{\eta}_m \frac{\beta_m}{\beta_0} \frac{k_{lm}(p_c - 1)}{k_{lm} + p_c k_{cm}} \sin(\vartheta_0 - \vartheta_m) \frac{1 - R_{me}^{fl} \rho_e + (R_{me}^{fl} - \rho_e) e^{2ik_{lm}t_l}}{1 - R_{me}^{fl} \rho_e + R_{me}^{lc} (R_{me}^{fl} - \rho_e) e^{2ik_{lm}t_l}} A_{c0}^{h+}; \quad (\text{A.16})$$

at the interface between the buffer layer and the substrate:

$$A_{sm}^{e-} = -\frac{n_f^2 k_{cm}}{n_s^2 k_{lm}} \frac{(1 + R_{me}^{bs})(1 + R_{me}^{fb})(1 - R_{me}^{fl}) e^{i(k_{bm}t_b + k_{fm}t_f + k_{lm}t_l)}}{(1 + R_{me}^{fb} R_{me}^{bs} e^{2ik_{bm}t_b})(1 - R_{me}^{fl} \rho_e + (R_{me}^{fl} - \rho_e) e^{2ik_{lm}t_l})} A_{cm}^{e+}. \quad (\text{A.17})$$

Here,

$$\rho_e = \frac{R_{me}^{fb} + R_{me}^{bs} e^{2ik_{bm}t_b}}{1 + R_{me}^{fb} R_{me}^{bs} e^{2ik_{bm}t_b}} e^{2ik_{fm}t_f}, \quad (\text{A.18})$$

$$R_{me}^{fb} = \frac{k_{fm} - p_b k_{bm}}{k_{fm} + p_b k_{bm}}, R_{me}^{bs} = \frac{k_{bm} - p_s k_{sm}}{k_{bm} + p_s k_{sm}}, R_{me}^{fl} = \frac{k_{fm} - p_l k_{lm}}{k_{fm} + p_l k_{lm}}, R_{me}^{lc} = \frac{k_{lm} - p_c k_{cm}}{k_{lm} + p_c k_{cm}}, \quad (\text{A.19})$$

$$p_b = \left(\frac{n_f}{n_b}\right)^2, p_s = \left(\frac{n_b}{n_s}\right)^2, p_l = \left(\frac{n_f}{n_l}\right)^2, p_c = \left(\frac{n_l}{n_c}\right)^2. \quad (\text{A.20})$$

The electromagnetic field of each Floquet wave as a function of x is either oscillatory or it decays exponentially in the various media, depending whether k_{zm} is real or imaginary. If the condition $0 < |\beta_m| < n_c k_0$ is satisfied, the wave is radiated into cover and substrate. If $n_c k_0 < |\beta_m| < n_s k_0$, the wave radiates into the substrate, but decays exponentially in the cover (we suppose $n_s > n_c$). If $n_s k_0 < |\beta_m| < n_f k_0$, the waves are guided. If $|\beta_m| > n_f k_0$, it can be proven that $\delta\beta$ is purely real such that those waves do not influence the damping of the guided wave [10, 18]. By choosing proper periodicities, $\beta_{-1} = \sqrt{[\beta_0 \sin(\vartheta_0)]^2 + [\beta_0 \cos(\vartheta_0) - \frac{2\pi}{\Lambda}]^2}$ can be smaller than $n_c k_0$ such that the wave is radiated into the cover.

After the equivalent boundary conditions [10] are applied to the perturbed fields E_0 and H_0 at each interface, We obtain an equation which is different from

the dispersion equation of the unperturbed guide (see Eq.(A.9)) by a modified term

$$\frac{1 - R_{0h}^{fl} R_{0h}^{fb} e^{2ik_{f0}t_f}}{R_{0h}^{fb} e^{2ik_{f0}t_f} - R_{0h}^{fl}} - R_{0h}^{lc} e^{2ik_{l0}t_l} = -(k_l - k_c)(1 + R_{0h}^{lc}) e^{2ik_{l0}t_l} \\ \times \sum_{|m|=1}^{\infty} \tilde{\eta}_m^* \left\{ 2k_{c0} + i \frac{\beta_0}{\beta_m} \left[k_{cm} A_{cm}^{e+} \sin(\vartheta_0 - \vartheta_m) - \frac{A_{cm}^{h+}}{Z_0} \cos(\vartheta_0 - \vartheta_m) \right] \right\}. \quad (A.21)$$

We assume that the actual propagation constant for calculating the right-hand side of Eq.(A.21) is approximated to β_0 . At the left-hand side, the actual propagation constant $\beta_0 + \delta\beta$ is substituted. Using the first two terms of a Taylor expansion of the left-hand side, and putting the first term equal to zero on account of Eq.(A.21) , an expression for $\delta\beta$ can be obtained.

From now on, the formulas become different for the cases $n_l < n_e$ and $n_l \geq n_e$. If $n_l < n_e$, $\delta\beta$ equals

$$\delta\beta = \frac{i}{2} k_{f0} (k_{l0} - k_{c0}) \frac{[1 - (R_{0h}^{fl})^2](1 + R_{0h}^{lc}) e^{2ik_{l0}t_l}}{R_{0h}^{fl} t_{eff} n_e \Upsilon} \\ \times \sum_{|m|=1}^{\infty} \tilde{\eta}_m^* \left\{ 2k_{c0} + i \frac{\beta_0}{\beta_m} \left[k_{cm} A_{cm}^{e+} \sin(\vartheta_0 - \vartheta_m) - \frac{A_{cm}^{h+}}{Z_0} \cos(\vartheta_0 - \vartheta_m) \right] \right\}, \quad (A.22)$$

in which the effective waveguide thickness t_{eff} is

$$t_{eff} = t_f + \frac{i}{k_{b0}} + i \frac{1 - (R_{0h}^{lc} e^{2ik_{l0}t_l})^2}{k_{l0} \Upsilon} \\ - 2i \frac{\Im \{ R_{0h}^{fl} \} R_{0h}^{lc} e^{2ik_{l0}t_l}}{\Upsilon} \left(\frac{k_{f0}}{k_{l0}} t_l + i \frac{k_{f0}}{k_{l0} k_{c0}} \right), \quad (A.23)$$

where \Im is an operator performing on a complex value to obtain its imaginary part. In fact, each term at the right-hand side of Eq.(A.23) is purely real. Υ , appearing in Eqs.(A.22) and (A.23) equals

$$\Upsilon = 1 + 2R_{0h}^{lc} e^{2ik_{l0}t_l} \Re \{ R_{0h}^{fl} \} + (R_{0h}^{lc} e^{2ik_{l0}t_l})^2. \quad (A.24)$$

\Re is an operator performing on a complex value to obtain its real part. The amplitude A_{c0}^{h+} and the power P_g of the guided wave are related by

$$P_g = M_h |A_{c0}^{h+}|^2, \quad (A.25)$$

and

$$M_h = \frac{1}{4} \frac{n_f^2 - n_l^2}{n_f^2 - n_e^2} \frac{c_0}{n_e} \frac{\Upsilon t_{eff}}{(1 + R_{0h}^{lc})^2} e^{-2ik_{l0}t_l}, \quad (\text{A.26})$$

where c_0 is the light speed in vacuum.

If $n_l > n_e$, $\delta\beta$ is

$$\delta\beta = \frac{i}{2} k_{f0} (k_{l0} - k_{c0}) \frac{[1 - (R_{0h}^{fl})^2] (1 + R_{0h}^{lc})}{R_{0h}^{lc} t_{eff} n_e \Upsilon} \times \sum_{|m|=1}^{\infty} \tilde{\eta}_m^* \left\{ 2k_{c0} + i \frac{\beta_0}{\beta_m} \left[k_{cm} A_{cm}^{e+} \sin(\vartheta_0 - \vartheta_m) - \frac{A_{cm}^{h+}}{Z_0} \cos(\vartheta_0 - \vartheta_m) \right] \right\}, \quad (\text{A.27})$$

where

$$t_{eff} = t_f + \frac{i}{k_{b0}} + 2 \frac{\Im\{R_{0h}^{lc} e^{2ik_{l0}t_l}\} R_{0h}^{fl}}{\Upsilon k_{l0}} + \frac{1 - (R_{0h}^{fl})^2}{\Upsilon} \left(\frac{k_{f0}}{k_{l0}} t_l + i \frac{k_{f0}}{k_{l0} k_{c0}} \right), \quad (\text{A.28})$$

and

$$\Upsilon = |R_{0h}^{fl} + R_{0h}^{lc} e^{2ik_{l0}t_l}|^2, \quad (\text{A.29})$$

$$P_g = M_h |A_{c0}^{h+}|^2, \quad (\text{A.30})$$

$$M_H = \frac{1}{4} \frac{n_l^2 - n_e^2}{n_l^2 - n_e^2} \frac{c_0}{n_e} \frac{\Upsilon t_{eff}}{(1 + R_{0h}^{fl})^2}. \quad (\text{A.31})$$

At the right-hand side of Eq.(A.28), each term is purely real. The formulas given in this appendix can be applied for several other waveguide structures by putting some parameters to be equal. For example, let $n_l = n_f$, $n_b = n_s$, $t_l = 0$ and $t_b = 0$, then the formulas appearing in the case $n_l \geq n_e$ become the same as those derived in Ref. [10] (see Fig. 2.1).

REFERENCES

- [1] Proceedings S&A Symposium of the University of Twente, Enschede, The Netherlands, November 15-16, (1990).
- [2] M.L. Dakss, L. Kuhn, P.F. Heidrich, and B.A. Scott, "Grating coupler for efficient excitation of optical guided waves in thin films," *Appl. phys. Lett.*, Vol.16, pp.523-525, (1970).
- [3] A. Katzir, A.C. Livanos, J.B. Shellan, and A. Yariv, "Chirped gratings in integrated optics," *IEEE Journal of Quantum Electronics*, Vol. **QE-13**, NO.4, pp.296-304, (1977).
- [4] W.W. Ng, C.S. Hong and A. Yariv, A: "Holographic interference lithography for integrated optics," *IEEE Trans.*, **ED-25**, p.1193-1200, (1978).
- [5] M. Miler and M. Skalsky, "Stigmatically focusing coupler," *Electron. Lett.*, Vol.15, pp.275-276, (1979).
- [6] S. Ura, T. Suhara, H. Nishihara and J. Koyama, "An Integrated-Optic Disk Pickup Device," *IEEE, Journal L.T.*, Vol.LT-4, No.7, pp.913-918 (1986).
- [7] Shogo Ura, Toshiaki Suhara, and Hiroshi Nishihara, "Aberration characterizations of focusing grating coupler in an integrated-optic disk pickup device," *Applied Optics*, Vol.26, No.22, pp.4777-4782 (1987).

- [8] Detlef Heitmann and Carmen Ortiz, "Calculation and experimental verification of two-dimensional focusing grating couplers," *IEEE Journal of Quantum Electronics*, Vol.**QE-17**, No.7, pp.1257-1263 (1981).
- [9] Joel Seligson, "Modeling of a focusing coupler using vector scattering theory," *Appl. Opt.*, Vol.**27**, No4, pp.684-691 (1988).
- [10] Marek T. Włodarczyk and S. R. Seshadri, "Analysis of grating couplers in planar waveguides for waves at oblique incidence," *J. Opt. Soc. Am. A.*, Vol.**2**, No.2, pp.171-185 (1985).
- [11] Gen-ichi Hatakoshi and Shun-ichi Tanaka, "Coupled-mode theory for a plane and a cylindrical wave in optical waveguide Bragg grating lenses," *Journal of Opt. Soc. Am.*, Vol.**71**, No.1, pp.40-48 (1981).
- [12] E. Popov and L. Mashev, "Analysis of mode coupling in planar optical waveguides," *Optica Acta*, Vol.**32**, No. 3, pp.265-280 (1985).
- [13] K.O. Peng, "Imaging by curved holographic optical elements," Ph.D. thesis, Delft University of Technology, The Netherlands, (1983).
- [14] Daniel Malacara, J. Martin Carpio Valadéz and J. Javier Sánchez Mondragón, "Wavefront fitting with discrete orthogonal polynomials in a unit radius circle," *Optical Engineering*, Vol.**29**, No.6, pp.672-675 (1990).
- [15] Max Born and Emil Wolf, "Principles of Optics," sixth edition, Pergamon press, Oxford, (1980).
- [16] William Streifer, Don R. Scifres, Robert D. Burnham, "Analysis of grating-coupled radiation in GaAs:GaAlAs lasers and waveguides," *IEEE Journal of Quantum Electronics*, Vol.**QE-12**, pp.422-428 (1976).

- [17] E. Wolf, "Electromagnetic diffraction in optical systems, I. An integral representation of the image field," Proc. Roy. Soc. London Ser. **A253**, pp.349-357 (1959).
- [18] V.A. Sychugov and A.V. Tishchenko, "Light emission from a corrugated dielectric waveguide," Sov. Journal of Quantum Electronics, Vol.**10**, No.2, pp.186-189 (1980).
- [19] M. Mansuripur, "Certain computational aspects of vector diffraction problems," J. Opt. Soc. Am. A, Vol.**6**, No.5, pp.787-805 (1989).
- [20] Geoge N. Lawrence, Kenneth E. Moore, and Patrick J. Cronkite, "Rotationally symmetric construction optics for a waveguide focusing grating," Appl. Opt., Vol.**29**, No.15, pp.2315-2319, (1990).
- [21] G. N. Buinov and K. S. Mustafin, "Compensation of spherical aberration of hologram lenses when there is a short-wave shift of the reconstructing radiation," Opt. Spectrosc., Vol.**41**, No.1, pp.90-91, (1976).
- [22] T. Kuwayama, Y. Nakamura, N. Taniguchi and S. Suda, "Aberration corrected off-axis holographic lens," Conference Digest, ICO-13 Sapporo, C6-6, pp.520-521, (1984).
- [23] G. N. Buinov, I. E. Kit, K. S. Mustafin, and M.I. Savrasova, "Compensation of spherical aberration of hologram lenses by a plane-parallel plate," Opt. Spectrosc., Vol.**38**, No.1, pp.88-89, (1975).
- [24] Yaakov Amitai, Ireena A. Erteza, and Joseph W. Goodman, "Recursive design of a holographic focusing grating coupler," Appl. Opt., Vol.**30**, No.27, pp.3886-3890, (1991).
- [25] P.K. Tien, "Method of forming novel curved-line gratings and their use as reflectors and resonators in integrated optics," Optics Letters, Vol.**1**, No.2, pp.84-85, (1977).

- [26] M. Miler, M. Skalsky, "Stigmatically focusing grating coupler," *Electronics Letters*, Vol.15, No.10, PP.275-276, (1979).
- [27] Z.Q. Lin, S.T. Zhou, William S.C. Chang, S. Forouhar, and J.M. Delavaux, "A generalized two-dimensional coupled-mode analysis of curved and chirped periodic structures in open dielectric waveguides," *IEEE Trans. on Microwave Theory and Techniques*, Vol.MTT-29, No.9, pp.881-891, (1981).
- [28] C.W. Pitt, S. Reid, S. Reynolds and J. Skinner, "Waveguiding Fresnel lenses: Modelling and fabrication," *J. Modern Optics*, Vol.35, No.6, pp.1079-1111, (1988).
- [29] D.Y. Zang, C.S. Tsai, "Titanium-indiffused proton-exchanged waveguide lenses in LiNbO3 for optical information processing," *Appl. Opt.*, Vol.25, No.14, pp.2264-2271, (1986).
- [30] P.J.R. Laybourn, "Homogeneous refracting lenses for integrated optical circuits," *J. Modern Optics*, Vol.35, No.6, pp.1029-1048, (1988).
- [31] J. Braat and J. Waelpoel, "Guide to the optical design programme OPT-SYS," Philips Research Laboratories, The Netherlands, 94 pages, (1988).
- [32] Rudolf Kingslake, "Lens design fundamentals," first edition, Academic press, New York, (1978).
- [33] Warren J. Smith, "Modern optical engineering," first edition, McGraw-Hill, Inc., (1966).
- [34] Donald G. Burkhard and David L. Shealy, "Simplified formula for the illuminance in an optical system," *Appl. Opt.*, Vol.20, No.5, pp897-907, (1981). Donald G. Burkhard and David L. Shealy, "A different approach to lighting and imaging: formulas for flux density, exact lens and mirror

- equations and caustic surfaces in terms of the differential geometry of surfaces," Proceedings of SPIE, Vol.692, pp.248-273, (1986).
- [35] S.R. Jahan, M.A. Karim, "Refracting system for Gaussian-to-uniform beam transformation," Optics & Laser Technology, Vol.21, No.1, pp.27-30, (1989).
- [36] Carl C. Aleksoff, Kenneth K. Ellis, Bradley D. Neagle, "Holographic conversion of a Gaussian beam to a near-field uniform beam," Optical Engineering, Vol.30, No.5, pp.537-543, (1991).
- [37] Uri Levy, "Special CLEO issue: diffractive optics spawns, new products and a multimillion-dollar market," Photonics Spectra, pp.135-136, May (1992).
- [38] Th.J.M. Jongeling, "Technologische aspecten van planaire optische golfgeleiders," Afstudeerverslag, TH Delft, Faculteit der Technische Natuurkunde, (1988).
- [39] L.K. Cheng, "De invloed op de golfvoortplanting van een tralie in een planaire golfgeleiders," Afstudeerverslag, TH Delft, Faculteit der Technische Natuurkunde, (1989).
- [40] Toshihiko Tanaka, Norio Hasegawa, Shinji Okazaki and Yoshie Azuma, "Precise pattern delineation by refractive index matching in a trilayer resist system," J. Vac. Sci. Technol. B Vol.10, No.2, pp.723-728, (1992).

ACKNOWLEDGEMENTS

I am indebted to many colleagues in the Research Group of Optics, Department of Applied Physics, Delft University of Technology, the Netherlands, who have helped me during this research work.

I would like to express my deepest appreciation to Prof. dr. ir. H.J. Frankena for his guidance and helpful advice. The strictly deductive logic in which I have been trained by him during the last four years is my greatest acquisition and will certainly be useful for my future research work. He has spent much of his spare time to improve my dissertation and to translate the summary into Dutch. During the extension of last six months, he helped me to find additional financial support. I engrave his kindness on my memory.

I am grateful to Prof. dr. ir. J.J.M. Braat for numerous enthusiastic discussions and for his help in the system design for the holographic recording setup. I was astonished watching him deriving formulas for a difficult problem and hearing his answers which were so perfect each time.

I am pleased to acknowledge my gratitude to ir. F. H. Groen and ir. J. de Jong for useful discussions. Special thanks go to ir. C.J. van der Laan for his coating designs. I would like to thank A.J. van der Lingen, A. Kuntze, A. Looijen and R.C. Horsten for their technical support. I wish to express my gratitude to all colleagues in the optical polishing workshop: J.H. den Dulk, R.J. Kuiper, R. Partosobroto and Mrs. I. Nieuwlaat for their delicate skill during the production of all the lenses in the setup, and to R. Pols for his aid in designing and producing the mechanical parts.

Thanks to my colleagues Shaodong Wu and Daoping Li for their help in many ways. We became good friends, although they come from the mainland of China. I enjoyed conversations on politics, economy, culture and life with them during lunch time.

With all my heart, I am indebted to Dr. Otto C.C. Lin (the president of ITRI) and Dr. Ping Tien Wu (the former general director of MRL in ITRI) for their recommendations and encouragement. I would like to express my thanks to Dr. Ada Wen-Shung Ma Lin who encouraged me during a visit to the Netherlands. It was also a great pleasure to host Dr. Yin-Shun Gou (my advisor of M.Sc.) whose encouragement helped me a lot.

I owe my parents so much. They always bestow their children with endless love, especially me, the oldest son. I am looking forward to reuniting my family.

Summary

Focusing grating couplers (FGC's) are designed to outcouple a guided wave from an integrated optical circuit and to focus it onto a point above the waveguide. A model including the vectorial treatment of the electromagnetic field is introduced to calculate the field distributions at an FGC and around the focal point for estimating of the image quality. An FGC which covers a rectangular area on the waveguide is formed by corrugating part of the top surface of the waveguide. The corrugation depth is assumed to be small as compared to the wavelength of the incident wave and to the film thickness. We aim at a design that generates a spherical wave converging to a given point above the waveguide, the required grating pattern is determined from the phase difference between the incident guided wave and the required spherical wave. In reality, an FGC always causes some aberration in the spherical wave due to fabrication errors and deviations in the configuration outside the grating. Aberrations in the spherical wave are described by the deviation of the actual wavefront from a reference sphere with its center at the *point of reference* [13] (which is determined by minimizing the wavefront aberration). To investigate the field distributions at the FGC and around the focus, the FGC is divided into subgratings, each of which is approximated by a periodic and straight grating, such that the grating is regarded as an array of subgratings with different periods and orientations. A previously published method of calculating the field distribution of a grating coupler [10] is used to design the subgratings. Once the field at the center of each subgrating is known, the field distribution around the focus is calculated utilizing the modified Huygens-Fresnel principle [17], which operates with secondary plane waves rather than with secondary spherical waves.

For the analysis of grating couplers for waves at oblique incidence (see Appendix A of this dissertation), the coupling between an incident TE- (or TM-polarized) guided wave and diffracted waves with TE- as well as those with

TM-polarization with respect to the local grating vector is taken into account. In addition, the complex propagation constant of the incident guided wave is considered, leading to the optimization of the corrugation depth.

A comparison between our model and the more restricted earlier theories has been carried out, their agreement is shown. For an FGC produced on a waveguide consisting of a guiding film sandwiched between two semi-infinite other media, three components of the field distribution at the FGC have been calculated. For this FGC, the wavefront aberration of the focused wave resulting after phase correction in the presence of the grating describes a uniform tilt only, which causes the diffraction focus to be displaced over a small distance (in the order of $0.1\mu m$) in the direction opposite to the propagation direction of the guided wave. Theoretically, a coupling efficiency of 0.3 and a focal spot diameter of $0.76\mu m$ (at $\frac{1}{e^2}$ of the peak intensity) can be achieved for such an FGC with $N.A. = 0.6$.

The field amplitudes of the diffracted focused wave is proportional to the corrugation depth and the attenuation coefficient of the guided wave is proportional to the square of that corrugation depth. To obtain a high coupling efficiency, the corrugation depth should be chosen as large as possible. If the corrugation is chosen too large, however, the main peak of the diffraction field is broadened in the propagation direction of the guided wave. In order to prevent the focal spot from broadening and to realize a high coupling efficiency, we determine the corrugation depth such that the average power of the guided wave decays to $\frac{1}{e^2}$ of the input power after the wave has passed the FGC.

Our model has the advantage that it can include field deviation calculations caused by fabrication errors, by a light source displacement and by a wavelength shift. The quality of FGC's image is very sensitive to a light source displacement. For FGC's, coma and astigmatism are essential and considerable aberrations. A tolerance analysis using the Strehl intensity at the diffraction focus is used to calculate the tolerances for the grating alignment and for its shape parameters.

Because of stability problems and the low throughput of *e*-beam writing, holographic techniques are chosen to produce FGC's. Recording an FGC at one wavelength and reconstruction at another results in aberrations in the reconstructed beam. A holographic setup has to be designed to compensate for the aberration caused by this wavelength shift. Two different combinations of a holographic setup can, in principle, generate the same FGC pattern, but with aberrations of opposite signs, as discussed in Sec.4.2. The method of Ref. [20], to design a holographic recording setup for a collimated guided wave, is extended here for a diverging one. The related fabrication process is described. One branch of the holographic setup contains a collimating optical system, while the other system is designed to compensate the aberration caused by the wavelength shift such that the interference pattern at the recording plate has exactly the shape of the required FGC-lines. The period and curvature of those lines can be adjusted by the angle between these two branches. This holographic setup allows recording of FGC's with a maximum numerical aperture of 0.55 and a focal length of 2mm. In our experiments, the FGC's are recorded holographically at the wavelength of 363.8nm, and used at the wavelength of 632.8nm for coupling a focused wave out of the waveguide from an incident collimated wave.

A method [34] which is capable of calculating the intensity distribution in the recording plane is used to evaluate the performance of our holographic setup. This evaluation shows an inhomogeneous intensity distribution in the recording plane which can be approximated mathematically, allowing us to estimate the intensity ratio between two recording beams by integration of the intensity of each beam over the grating.

In our experiments, multilayer planar waveguides produced on two-inch silicon substrates are used to accommodate the FGC's. For such a multilayer waveguide, the coupling efficiency can be increased by reflecting part of the light radiated into substrate back to the cover where the beam is focused. Theoretically, the coupling efficiency could be as high as 0.6 by optimizing the

waveguide parameters and the corrugation depth. We found, however, that the wavefront distribution becomes very complicated due to reflections at the interfaces between the layers. This causes the focal spot to broaden slightly. In our experiments, a focal spot size of $2.9\mu m$ for an FGC with a focal length of $2.0mm$ and a grating diameter of $1.3mm$ have been obtained. The coupling efficiency of this FGC is about 0.15.

SAMENVATTING

Het doel van focuserende traliekoppelaars (FGC) is, om licht vanuit een golfgeleider in een geïntegreerd-optisch circuit om te zetten in een convergerende golf in het medium daarboven, of omgekeerd. Een dergelijke FGC wordt gevormd door een (doorgaans rechthoekig) deel het bovenoppervlak van de golfgeleider van een reliëf te voorzien. De diepte van dat reliëf wordt verondersteld klein te zijn ten opzichte van de golflengte van het invallende licht en van de dikte van de filmlaag. Gestreefd wordt naar een ontwerp waarin een bolvormige golf ontstaat rond een punt boven de golfgeleider, het daartoe benodigde traliëpatroon wordt bepaald uit het faseverschil tussen de invallende geleide golf en de genoemde bolvormige golf. In de praktijk veroorzaakt een FGC altijd enige aberratie in de bolvormige golf, ten gevolge van fabricagefouten en afwijkingen in de structuren buiten het tralië. Zulke aberraties worden beschreven met behulp van de afwijking tussen het echte golffront en een bol rond het *referentiepunt* [13] (dat bepaald wordt door de aberraties te minimaliseren). In dit proefschrift worden de veldverdelingen op de FGC, zowel als rond het brandpunt van de uittrekkende golf, bestudeerd. Hiertoe wordt de FGC onderverdeeld in subtraliës, die elk als benadering geacht worden periodiek en van rechte traliëlijnen voorzien te zijn. Een eerder gepubliceerde methode voor veldberekening [10] kan hierop direct worden toegepast. Indien het veld in het midden van elk subtralië bekend is, kan het veld rond het brandpunt berekend worden met behulp van het Huygens-Fresnel principe [17], dat op vlakke, in plaats van bolvormige, secundaire golven gebaseerd is.

De analyse van traliekoppelaars voor scheef invallende geleide golven gaat uit van een invallende TE- (of TM-) modus die energie uitwisselt met zowel TE- als TM-golven ten opzichte van de traliëvector. Voorts wordt daarbij de werkelijk optredende complexe voortplantingsconstante in rekening gebracht, waaruit een optimalisatievoorwaarde voor de traliëdiepte naar voren komt. Vergelijken

van onze methode met eerdere theorieën leidt tot een hoge mate van overeenstemming. Voor een FGC die gevormd is op een golfgeleidende filmlaag tussen twee halfoneindige media zijn de drie componenten van het veld in het tralie berekend. In dat geval bestaat de aberratie in de gefocusseerde golf ten gevolge van de fasecorrectie door de aanwezigheid van het tralie slechts uit een vaste scheefstelling van het golffront, waardoor het brandpunt verplaatst wordt over een kleine afstand (in de orde van $0.1\mu m$) tegen de voortplantingsrichting van de geleide golf in. Theoretisch kan een koppelrendement van 0.3 en een brandpuntsdiameter van $0.76\mu m$ (tussen de punten met $\frac{1}{e^2}$ van de piekintensiteit) bereikt worden voor zo'n FGC, bij een numerieke apertuur van 0.6.

De amplitude van de afgebogen gefocusseerde golf is recht evenredig met de traliediepte en de dempingscoëfficiënt voor de geleide golf is evenredig met het kwadraat ervan. Voor een groot koppelrendement moet deze diepte zo groot mogelijk gekozen worden. Als deze echter té groot gekozen wordt, zal het centrale maximum van het afgebogen veld rond het brandpunt verbreed worden in de voortplantingsrichting van de geleide golf. Om zowel een smal brandpunt als een hoog koppelrendement te bereiken, wordt hier voorgesteld om de traliediepte zodanig te bepalen dat het gemiddelde vermogen in de geleide golf na het doorlopen van het tralie tot $\frac{1}{e^2}$ van de invallende waarde is afgenomen.

Ons model heeft het voordeel dat ook de veldafwijkingen ten gevolge van fabricagefouten, van verplaatsingen van de lichtbron van golflengte-verschuivingen bepaald kunnen worden. De beeldkwaliteit in het brandpunt blijkt zeer gevoelig te zijn voor de vorm van de invallende golf (verplaatsingen van de bron). Belangrijke aberraties voor FGC's zijn coma en astigmatisme. Een analyse, gebruik makend van de Strehl-verhouding in het brandpunt, is uitgevoerd voor het berekenen van de toleranties voor de tralie-positionering en voor zijn vormparameters.

In verband met stabiliteitsproblemen en met de lage opbrengst van het schrijven met elektronenstralen, is er gekozen voor een holografische productietechniek.

niek. Opname van een FGC met een andere golflengte dan bij weergave leidt tot aberraties in de gefocusseerde bundel. De holografische opstelling moet zodanig opgezet worden dat deze aberraties gecompenseerd worden. In principe kunnen twee verschillende holografische configuraties hetzelfde FGC-patroon vastleggen doch, zie Sec. 4.2, met tegengestelde tekens voor de aberraties. De methode van Ref. [20] om een holografische opstelling te ontwerpen voor opname van een FGC met een gecollimeerde invallende geleide golf is uitgebreid naar de mogelijkheid van divergerende invallende golven. Op basis hiervan is een opstelling, bestaande uit conventionele lenzenstelsel, ontworpen en vervaardigd. Een tak van de interferentie-opstelling bevat een collimerend stelsel, de andere is ontworpen om de aberraties ten gevolge van de golflengte-verschuiving te compenseren. De periode en kromming van de aldus geproduceerde interferentielijnen kunnen geregeld worden door de hoek tussen de beide takken te veranderen. De opstelling is geschikt voor het vastleggen van FGC's met een maximale numerieke apertuur van 0.55 en een brandpuntsafstand van 2mm . De holografische opname geschiedt bij een golflengte van 363.8nm , de koppelaar wordt gebruikt bij 632.8nm voor koppeling uit een gecollimeerde geleide golf.

Een methode voor het berekenen van het intensiteitsverloop in het hologramvlak [34] is gebruikt om de opstelling te evalueren. Dit bracht een inhomogene verdeling aan het licht die, wiskundig benaderd, tot een schatting heeft geleid voor de intensiteitsverhouding tussen de beide opnamebundels.

In de experimenten zijn meerlaags golfgeleiders, gedeponerd op silicium-substraten met een diameter van 2 inch, gebruikt als ondergrond voor de FGC's. Voor zulke meerlaags geleiders kan het koppelrendement verbeterd worden door een deel van het licht dat het substraat wordt ingestraald, terug te kaatsen naar de deklaag waarin het brandpunt wordt gevormd. Door optimaliseren van de golfgeleider parameters en de traliediepte kan aldus een theoretisch rendement van 0.6 bereikt worden. Er is echter gevonden dat de veldverdeling door reflecties aan de grensvlakken tussen de lagen zeer ingewikkeld wordt, waardoor

het brandpunt enigszins verbreed wordt. Experimenteel is een brandpunt met een diameter van $2.9\mu m$ voor een FGC met een brandpuntsafstand van $2.0mm$ en een traliediameter van $1.3mm$ bereikt. Het koppelrendement daarvoor is ongeveer 0.15.

CURRICULUM VITAE

Chieh-wen Wang

born on the ninth of October, 1961 in Taiwan, the Republic of China.

EDUCATION:

1988-1992: Ph.D. student under the guidance of Prof. H.J. Frankena at the Department of Applied Physics, Delft University of Technology.

1983-1985: Master degree at the Institute of Electro-Optical Engineering, National Chiao Tung University, Hsinchu, Taiwan, July, 1985. Master thesis: "Indium-tin-oxide Film: Preparation and Characterization".

1979-1983: Bachelor degree at the Department of Physics, Chung Yuan University, Chungli, Taiwan, June, 1983.

WORK EXPERIENCE:

1985-1988: research worker for Materials Research Laboratories (MRL), Industrial Technology Research Institute (ITRI), in Taiwan. Worked on projects: Liquid phase epitaxy processes for GaP red/green light emitting diodes and Bulk-type InSb magnetoresistance sensors.